TURUN
YLIOPISTO
UNIVERSITY
OF TURKU

INVESTIGATING MULTI-WAVELENGTH PHOTOPLETHYSMOGRAPHY FOR HEMODYNAMIC MONITORING

Jukka-Pekka Sirkiä

TURUN YLIOPISTON JULKAISUJA ANNALES UNIVERSITATIS TURKUENSIS
SARJA SER. F OSA TOM. 61 | TECHNICA INFORMATICA | TURKU 2025

TURUN
YLIOPISTO
UNIVERSITY
OF TURKU

INVESTIGATING MULTI-WAVELENGTH PHOTOPLETHYSMOGRAPHY FOR HEMODYNAMIC MONITORING

Jukka-Pekka Sirkiä

TURUN YLIOPISTON JULKAISUJA ANNALES UNIVERSITATIS TURKUENSIS
SARJA SER. F OSA TOM. 61 | TECHNICA INFORMATICA | TURKU 2025

University of Turku

Faculty of Technology
Department of Computing
Information and Communication Technology
Doctoral Programme in Technology

Supervised by

Assistant Professor, Matti Kaisti
Department of Computing
University of Turku
Turku, Finland

Professor, Pasi Liljeberg
Department of Computing
University of Turku
Turku, Finland

Reviewed by

Professor, Antti Vehkaoja
Biomedical Technology
Tampere University
Tampere, Finland

Associate Professor, Yannis Papadopoulos
School of Applied Mathematical and
Physical Sciences
National Technical University of Athens
Athens, Greece

Opponent

Professor, John Allen
Centre for Intelligent Healthcare
Coventry University
Coventry, United Kingdom

ISBN 978-952-02-0236-1 (PRINT)
ISBN 978-952-02-0237-8 (PDF)
ISSN 2736-9390 (Painettu/Print)
ISSN 2736-9684 (Sähköinen/Online)
Painosalama, Turku, Finland, 2025

UNIVERSITY OF TURKU
Faculty of Technology
Department of Computing
Information and Communication Technology
SIRKIÄ, JUKKA-PEKKA: Investigating Multi-Wavelength Photoplethysmography for Hemodynamic Monitoring
Doctoral dissertation, 142 pp.
Doctoral Programme in Technology
May 2025

ABSTRACT

Photoplethysmography (PPG) is the predominant technique used by modern wearable devices to measure cardiovascular parameters, from simple heart rate and its variability to respiratory rate, and cardiovascular age. In clinical practice, PPG is the technique behind the pulse oximeter that provides vital information about peripheral oxygen saturation – a parameter that modern wearables also measure. The configuration of the sensor in the common reflectance mode is relatively straightforward with a light source illuminating the skin and an adjacent photodetector detecting the backscattered light. The detected intensity is modulated by the light-absorbing cutaneous blood volume which has a periodic component that varies with the beating of the heart. An important factor in obtaining the signal is the wavelength of the light source. Due to the optical properties of the skin chromophores, the penetration depth of light varies so that in general in the visible light and in the very near-infrared (NIR) part of the spectrum, longer wavelengths penetrate deeper than shorter wavelengths. Multi-wavelength PPG (MWPPG) utilizes this by using several wavelengths of light simultaneously with the aim of providing information from the large arteries buried deep in the tissue to the more superficial arterioles and capillaries.

This thesis contributes to MWPPG research by developing a fingertip-based method that enables the recording of MWPPG signals under controlled and measurable sensor contact pressure. The method is initially demonstrated with a device consisting of five light-emitting diodes (LEDs) with central wavelengths ranging from 465 to 880 nm. The method is then developed further by inverting the typical MWPPG sensor setup of (relatively) narrow-band LEDs and a wideband photodiode to a configuration consisting of a wideband light source and a spectrometer capable of extracting 99 different channels with a range of approximately 434–731 nm. Using the oscillometric blood pressure (BP) measurement technique, the method is demonstrated to extract BP simultaneously from large arteries using wavelengths over 630 nm and from more superficial vessels using wavelengths under 590 nm. The part in the middle, 590–630 nm, forms a transition band where a jump from probing superficial, low-pressure, blood vessels to deeper, high-pressure, vessels occurs. The experimental results are corroborated with a Monte Carlo (MC) photon propagation model.

MWPPG signals are then further studied under different levels of sensor contact pressure. Static pressure held at relatively high pressure levels is shown to cause different responses between the wavelength channels, and, based on the MC results, is hypothesized to reveal information about the blood vessels primarily responsible for vasodilation in response to pressure stimulation. Additionally, a separate study is performed to study the effects of sensor contact pressure on measured peripheral oxygen saturation (SpO_2), pulse arrival time (PAT) and pulse waveform features. The results show that especially sensitive are the parameters that are based on amplitudes or DC level.

Finally, in the age of rapidly advancing artificial intelligence, a mathematical model is developed to generate synthetic PPG signals. The model can help tackle problems related to, for example, dataset sizes, bias, and data privacy. The synthetic model is demonstrated with a wearable device that uses convolutional neural networks (CNNs) trained with only synthetic data to estimate heart rate (HR) from measured signals. The performance of the CNNs often exceeds the more traditional methods used to calculate HR, providing a path to apply the synthetic model to more complex problems. This is briefly demonstrated by combining the synthetic model with another mathematical physiological model to generate synthetic oscillograms similar to those obtained with the presented MWPPG instruments.

KEYWORDS: photoplethysmography, multi-wavelength photoplethysmography, microvasculature, microcirculation, blood pressure, synthetic biosignal

TURUN YLIOPISTO
Teknillinen tiedekunta
Tietotekniikan laitos
Tietotekniikka
SIRKIÄ, JUKKA-PEKKA: Investigating Multi-Wavelength Photoplethysmography for Hemodynamic Monitoring
Väitöskirja, 142 s.
Teknologian tohtoriohjelma
Toukokuu 2025

TIIVISTELMÄ

Fotopletysmografia (PPG) on nykyaikaisissa puettavissa laitteissa käytetty vallitseva tekniikka kardiovaskulaaristen parametrien, kuten sykkeen, sykevälivaihtelun, hengitystiheyden ja kardiovaskulaarisen iän, mittaamiseen. PPG-tekniikkaan pohjautuu myös kliinisessä käytössä yleinen pulssioksimetri, jolla voidaan mitata veren happisaturaatio – parametri, jota myös nykyaikaiset puettavat laitteet mittaavat. PPG-sensorin toimintatapa on yksinkertainen yleisesti käytössä olevassa heijastukseen perustuvassa tekniikassa: ledi valaisee ihoa ja fotodiodi havaitsee takaisinpäin siroavan valon. Ihon veritilavuus, joka vaihtelee muun muassa sydämen lyöntien mukaan, absorboi valoa ja moduloi näin fotodiodin rekisteröimää valon intensiteettiä. Keskeinen signaalin informaatiosisältöön vaikuttava tekijä on ledin aallonpituus. Ihon optisten ominaisuuksien vuoksi valon tunkeutumissyvyys vaihtelee, ja yleisesti ottaen näkyvän valon ja lähi-infrapuna-alueen alkupään alueella pidemmät aallonpituudet tunkeutuvat syvemmälle kuin lyhyemmät aallonpituudet. Moniaallonpituus-PPG (MWPPG) hyödyntää tätä käyttämällä samanaikaisesti useita eri valon aallonpituuksia, mikä mahdollistaa hemodynaamisen informaation saamisen syvällä ihossa sijaitsevista suurista valtimoista että pinnallisimmista pikkuvaltimoista ja kapillaareista.

Tämä väitöstyö edistää MWPPG-tutkimusta kehittämällä mittausmenetelmän, joka mahdollistaa MWPPG-signaalien mittaamisen sormenpäästä hallitussa ja mitattavassa sensorikontaktipaineessa. Menetelmää kehitetään aluksi laitteella, joka hyödyntää viittä eri valon aallonpituutta välillä 465–880 nm. Menetelmää kehitetään väitöstyössä edelleen kääntämällä tyypillinen MWPPG-sensorikonfiguraatio kapean aallonpituusalueen ledeistä ja laajan spektrivasteen fotodiodista konfiguraatioksi, joka käsittää laajan aallonpituusalueen valonlähteen ja spektrometrin. Tällaisella konfiguraatiolla voidaan mitata 99 eri kaistaa 434–731 nm:n alueella. Kontrolloimalla sensorikontaktipainetta oskillometrisestä verenpainemittaustekniikasta tutulla tavalla, menetelmällä voidaan mitata verenpaine samanaikaisesti sekä suurista valtimoista käyttäen yli 630 nm:n aallonpituuksia että pinnallisimmista verisuonista käyttäen alle 590 nm:n aallonpituuksia. Näiden väliin jäävä alue, 590–630 nm, muodostaa ns. siirtymäalueen, jossa tapahtuu siirtymä pinnallisista, matalan verenpaineen verisuonista syvempiin, korkean verenpaineen suoniin. Mitattuja tuloksia verrataan Monte Carlo (MC) -simulaatiomallin tuloksiin.

MWPPG-signaaleja tutkitaan sitten tarkemmin eri sensorikontaktipaineissa. Mittauksissa, joissa kontaktipaine pidetään verrattain korkeana, havaitaan selkeästi erilaisia vasteita eri aallonpituuskanavien välillä. MC-tulosten pohjalta voidaan todeta, että mittauksista saadaan tietoa pikkuvaltimoista, jotka ovat vastuussa verisuonten laajenemisesta vastineena paineen aiheuttamaan stimulaatioon. Tämän lisäksi suoritetaan tutkimus sensorikontaktipaineen vaikutuksista mitattuun veren happisaturaatioon (SpO_2), pulssin saapumisaikaan (PAT) ja pulssiaaltomuodosta laskettaviin suureisiin. Tulokset osoittavat, että erityisen herkkiä ovat parametrit, jotka perustuvat aaltomuodon amplitudiin tai DC-tasoon.

Väitöstyön lopuksi esitetään matemaattinen malli, jolla voidaan luoda synteettisiä PPG-signaaleja. Nopeasti kehittyvällä tekoälyn aikakaudella malli voi auttaa esimerkiksi datasettien kokoon, vinoumaan ja tietosuojaan liittyvissä ongelmissa. Synteettistä mallia demonstroidaan puettavalla laitteella, jossa suoritetaan synteettisellä datalla koulutettuja konvoluutioneuroverkkoja (CNN) sykkeen arvioimiseksi mitatuista signaaleista. Luodut neuroverkkopohjaiset mallit suoriutuvat usein paremmin kuin perinteisemmät sykkeen laskemiseen käytetyt menetelmät, mikä luo pohjan synteettisen mallin soveltamiseen monimutkaisempiin ongelmiin. Tätä esitellään lyhyesti yhdistämällä synteettinen malli oskillometrista verenpainemittausta mallintavan matemaattisen mallin kanssa. Mallilla voidaan tuottaa synteettisiä oskillogrammeja, jotka muistuttavat väitöstyössä esiteltävillä MWPPG-instrumenteilla mitattuja.

ASIASANAT: fotopletysmografia, moniaallonpituusfotopletysmografia, mikroverisuonisto, mikroverenkierto, verenpaine, synteettinen biosignaali

Acknowledgements

First and foremost, I would like to thank my supervisors, Professor Pasi Liljeberg and Assistant Professor Matti Kaisti, for all their help and guidance during these years. I am extremely grateful to my primary supervisor Matti for bringing me on board his team and providing me with the opportunity to engage in thoroughly captivating research. Without him, this thesis would not have been possible. His vast knowledge of the field is deeply impressive, and his guidance has been invaluable. It has been admirable and inspiring to witness his energetic drive and passion for research.

It has been a privilege to work with many excellent researchers within the Digital Health Technology Lab at the University of Turku during my research career, and I would like to express my gratitude to all of you. In particular, I am grateful to Tero Koivisto and Dr. Mikko Pänkäälä for the opportunities to participate in many interesting research projects. I would like to give special thanks to Dr. Tuukka Panula for all his help and fruitful discussions during our time as doctoral researchers. You and Matti have been my closest colleagues, and it has truly been an honor to work with such brilliant scientists.

I would also like to thank professor Ilkka Kantola and research nurse Essi Roine for making it possible to perform clinical measurements at the Turku university hospital.

My sincere thanks go to the reviewers, Professor Antti Vehkaoja and Associate Professor Yannis Papadopoulos, for taking the time and effort to assess my thesis and provide valuable comments. I am most grateful to Professor John Allen for willing to make the journey from the UK to Finland, and I am honored to have him as my opponent.

My heartfelt appreciation goes to my family for their unwavering support and warmth during this journey. Especially, my parents, Seija and Jarkko, have always been there for me, encouraging me in my endeavors.

Finally, I want to acknowledge my furry little research assistant Hillevi for his emotional support by having always been purring next to my keyboard, and to thank my wife Emma for being the bedrock of my life. You have patiently listened to me talk about my research, helped me when I needed another pair of hands while working with the devices, and even participated as an alpha tester. Without you, this thesis would not have happened, simply because you were the one who gave me the

inspiration to embark on a new career back in the days, but moreover because of your love.

Espoo, May 2025
Jukka-Pekka Sirkiä

Table of Contents

Acknowledgements . . . . **vii**

Table of Contents . . . . **ix**

Abbreviations . . . . **xii**

List of Original Publications . . . . **xiv**

1 Introduction **1**

2 Literature Review **7**
- 2.1 Human Skin and Cutaneous Vasculature 7
  - 2.1.1 Skin Structure 7
  - 2.1.2 Cutaneous Vasculature 8
  - 2.1.3 Cutaneous Microcirculation in Disease 9
- 2.2 Tissue Optics 10
  - 2.2.1 Optical Properties of the Skin 10
  - 2.2.2 Beer-Lambert Law 12
  - 2.2.3 Monte Carlo Photon Propagation Modeling 13
- 2.3 Photoplethysmography 15
  - 2.3.1 Multi-Wavelength Photoplethysmography 18
  - 2.3.2 Remote Photoplethysmography 19
  - 2.3.3 Synthetic Photoplethysmography Signals 20
- 2.4 Other Optical Sensing Techniques of the Cutaneous Vasculature 21
  - 2.4.1 Near-Infrared Spectroscopy 21
  - 2.4.2 Diffuse Correlation Spectroscopy 22
  - 2.4.3 Hyperspectral Imaging 23
  - 2.4.4 Laser Doppler Flowmetry 24
  - 2.4.5 Laser Speckle Contrast Imaging 24
  - 2.4.6 Photoacoustic Imaging 26
  - 2.4.7 Optical Coherence Tomography 27
  - 2.4.8 Videocapillaroscopy 27

2.4.9 Orthogonal Polarization Spectral Imaging 28
2.4.10 Sidestream Dark Field Imaging 29
2.4.11 Incident Dark-Field Illumination 30
2.5 Summary of Optical Sensing Techniques 30
2.6 Techniques to Obtain Hemodynamic Responses from the Cutaneous Vasculature 34

3 Aims of the Study 37

4 Materials and Methods 39
4.1 Instrument Design 39
4.2 Software 39
4.3 Signal Processing 40
4.4 Human Studies 40
4.4.1 Studies Ia and Ib 41
4.4.2 Study II 41
4.4.3 Study III 42
4.4.4 Study IV 42

5 Summary of Results and Discussion 43
5.1 Developed Instruments 43
5.1.1 Instrument I 43
5.1.2 Instrument II 47
5.1.3 Instrument III 48
5.1.4 Instrument IV 49
5.2 Depth-Resolved Blood Pressure 52
5.2.1 Working Principle 52
5.2.2 Experimental Results 53
5.2.3 Simulation Results 56
5.3 Effects of Contact Pressure on Multi-Wavelength Photoplethysmograms 58
5.3.1 Pressure Ramp 58
5.3.2 Pressure Steps 60
5.3.3 Static Pressure Hold 64
5.4 Synthetic Photoplethysmograms 67
5.4.1 Mathematical Model 67
5.4.2 Convolutional Neural Network Based Heart Rate Calculation 72

6 Conclusion 74

List of References 77

Original Publications **93**

Abbreviations

ADC	analog-to-digital converter
AI	artificial intelligence
AMPD	automatic multi-scale peak detection
AUC	area under curve
BLL	Beer-Lambert law
BP	blood pressure
CAD	coronary artery disease
CIV	current-induced vasodilation
CNN	convolutional neural network
CV	coefficient of variation
CVD	cardiovascular disease
DAC	digital-to-analog converter
DBP	diastolic blood pressure
DCS	diffuse correlation spectroscopy
ECG	electrocardiography
GUI	graphical user interface
HR	heart rate
HRV	heart rate variability
HSI	hyperspectral imaging
IDF	incident dark field illumination
IR	infrared
LDF	laser Doppler flowmetry
LED	light-emitting diode
LSCI	laser speckle contrast imaging
MAP	mean arterial pressure
MC	Monte Carlo
ML	machine learning
MOP	maximum oscillometric pressure
MWPPG	multi-wavelength photoplethysmography
NIR	near-infrared
NIRS	near infrared spectroscopy
OCT	optical coherence tomography

OPS	orthogonal polarization spectral imaging
PAI	photoacoustic imaging
PAT	pulse arrival time
P_c	contact pressure
PCB	printed circuit board
PI	perfusion index
PIV	pressure-induced vasodilation
PPG	photoplethysmography
PSD	power spectral density
P_t	transmural pressure
PTT	pulse transit time
PWA	pulse wave analysis
RAM	random access memory
RBC	red blood cell
RH	reactive hyperemia
ROI	region of interest
rPPG	remote photoplethysmography
SBP	systolic blood pressure
SD	standard deviation
SDF	sidestream dark field imaging
SDK	software development kit
SE	standard error
SNR	signal-to-noise ratio
SoC	system on a chip
SPG	speckle plethysmography
SpO_2	peripheral oxygen saturation
VSMC	vascular smooth muscle cell

List of Original Publications

This dissertation is based on the following original publications, which are referred to in the text by their Roman numerals:

I Sirkiä, J.-P., Panula, T., and Kaisti, M. Tonometric Multi-Wavelength Photoplethysmography for Studying the Cutaneous Microvasculature of the Fingertip. IEEE Transactions on Instrumentation and Measurement, 2023; 72: 4009113.

II Sirkiä, J.-P., Panula, T., and Kaisti, M. Wearable Edge Machine Learning with Synthetic Photoplethysmograms. Expert Systems with Applications, 2024; 238: 121523.

III Sirkiä, J.-P., Panula, T., and Kaisti, M. Investigating the Impact of Contact Pressure on Photoplethysmograms. Biomedical Engineering Advances, 2024; 7: 100123.

IV Sirkiä, J.-P., Panula, T., and Kaisti, M. Non-Invasive Hemodynamic Monitoring System Integrating Spectrometry, Photoplethysmography and Arterial Pressure Measurement Capabilities. Advanced Science, 2024; 11: 2310022.

The original publications have been reproduced with the permission of the copyright holders.

1 Introduction

Photoplethysmography (PPG) is the underlying technique in the clinically important pulse oximeter and is arguably the most common sensor modality used in modern wearable devices to monitor hemodynamic and, more broadly, cardiovascular parameters, such as heart rate. A telltale sign of the presence of a PPG sensor in a wearable device is a light source illuminating the skin. The popularity of this optical technique is essentially due to its simplicity for the user: the skin is illuminated with a light source, and the changes in the light intensity caused by blood volume variations are detected, provided that the location of the body contains sufficient vasculature. Thus, many easily accessible locations can be used, such as the wrist, finger, ear, or temple with convenient form factors allowing sensor embedding, such as watches, rings, earphones, and glasses. The simplicity of the technique is not limited to the user side of the device, but also extends to the manufacturing side. In its simplest form, only a handful of inexpensive semiconductor components, mainly a light-emitting diode (LED) and a photodiode together with the accompanying electronics, are required to construct a PPG sensor. On top of these benefits, PPG signals have also shown to contain a wealth of information from which various cardiovascular parameters, in addition to the rather trivial heart rate, can be extracted. PPG is therefore an attractive technique regardless of the end product, whether it is a consumer-grade or a clinical-grade device.

PPG is a relatively old technique with its origins dating back to the last half of the 1930s. Alrick Hertzman and his colleagues are regarded as pioneers in the establishment of the technique. [1] In 1937 they presented observations on the variation of light transmission through a finger [2] with subsequent papers describing the measurement of PPG signals from the nasal septum [3] and fingers and toes using a system consisting of a car headlight [4]. In 1938 a system enabling to measure PPG in both relfectance and transmissive mode was presented and demonstrated by measuring signals from different parts of the body [5]. Within a few more years they had investigated the pulsatile AC and non-pulsatile DC components of the PPG signal [6], applications of PPG in peripheral vascular disease [7], and the effects of the vasomotor response on PPG [8].

Technological advancements, especially in semiconductors (e.g. the invention of the LED in the 1960s), have since allowed researchers to improve the technique in terms of capability, sensitivity, and reliability. A major breakthrough was the intro-

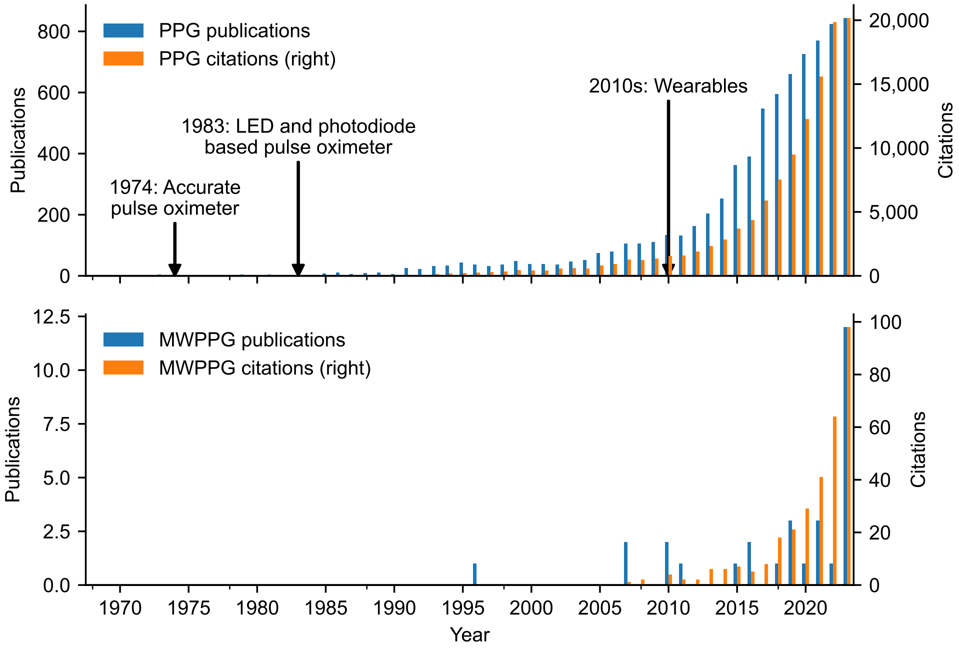

Figure 1. Web of Science citation report for the search strings *photoplethysmography OR photoplethysmogram* (upper panel) and *"multi-wavelength photoplethysmography" OR "multiwavelength photoplethysmography"* (lower panel). The period is from 1968 to 2023.

duction of an accurate pulse oximeter in 1974 by Takuo Aoyagi [9], which allowed non-invasive measurement of blood oxygen saturation and paved the way for the clinical use of PPG. In 1983, a pulse oximeter based on LEDs and a photodiode, i.e., the components used by modern PPG sensors, was developed [9]. Further advances in microelectronics in the 1990s and in the first decade of the millennium enabled the rise of wearables in the early 2010s. Wearables sparked great enthusiasm among researchers and launched PPG research onto a new trajectory, which is clearly visible in the upper panel of Figure 1 showing the number of PPG related publications and citations in the Web of Science database from 1968 to 2023.

Figure 2 views the same data, but at the level of publication category and for each decade, to reveal the prevailing research trends in each decade since the 1980s. In the 1980s and 1990s, research focused heavily on the medical and physiological aspects of PPG. In the 2000s the focus started to shift towards engineering disciplines, and by the 2010s engineering topics clearly dominated. The dominance of engineering continues in the 2020s but with new flavors including the rapidly evolving artificial intelligence research and analytical chemistry, the latter including topics such as the estimation of blood hemoglobin content (e.g. glycated hemoglobin in diabetes monitoring) and optimal light wavelength selection.

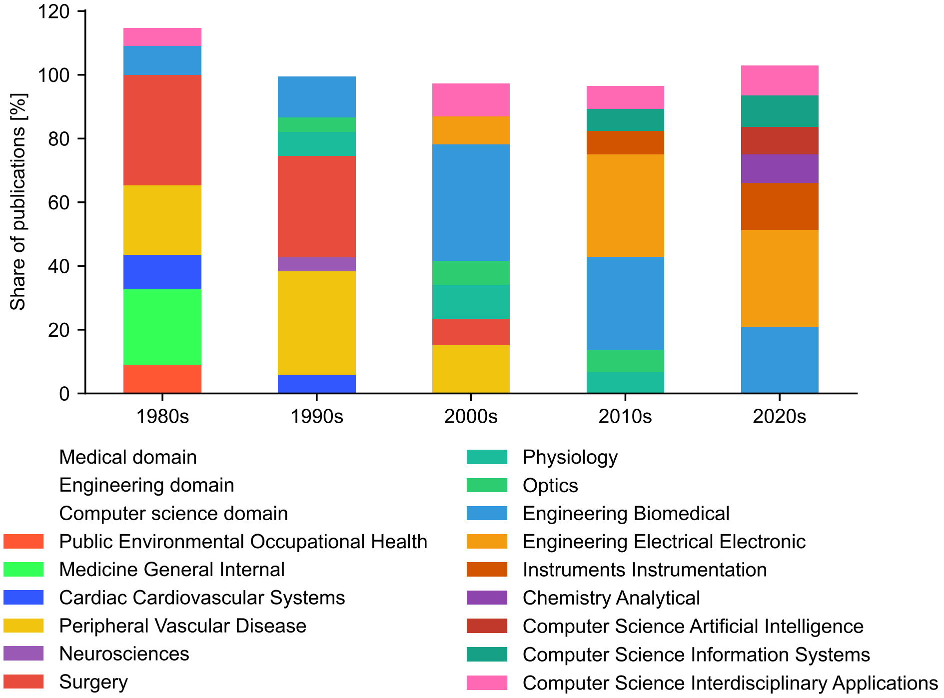

Figure 2. The top seven Web of Science citation report categories for the search string *photoplethysmography OR photoplethysmogram* for each decade since the 1980s. Note that the bars sum over 100% because an article can be categorized under more than one category.

PPG is commonly used to monitor heart rate, heart rate variability (HRV), respiratory rate and the clinically important peripheral oxygen saturation (SpO_2). Moreover, given the vast research interest, the technique has also been studied in various fields, such as blood pressure [10], sleep analysis [11], vascular age assessment [12], atrial fibrillation detection [13], pregnancy monitoring [14], and postoperative pain assessment [15]. However, in recent years a new area of research has emerged alongside single, dual (in the case of a pulse oximeter), and triple wavelength (combining a pulse oximeter and typically a green LED for motion robust sensing) PPG sensors, coined as multi-wavelength photoplethysmography (MWPPG) in an effort to extend the capabilities of PPG.

MWPPG extends the application of the PPG technique to several wavelengths of visible light or near-infrared (NIR) (typically at least blue and/or green, yellow, red and infrared (IR)), all measured simultaneously. The potential of MWPPG lies in the fact that different skin chromophores have different optical properties depending on the wavelength of electromagnetic radiation. This effectively means that different wavelengths of light penetrate into different depths of the skin, with, generally, in the visible and at the short-wavelength end of the NIR region of the electromagnetic spectrum, shorter-wavelength light penetrating less deeply than longer-wavelength light [16]. Combined with cutaneous vascular anatomy, where large blood-conducting arteries are buried deep in the skin with branches of smaller regulating arterioles arising toward the surface of the skin before branching themselves into capillaries [17], the promise of MWPPG technology is to add depth resolution to PPG.

MWPPG is a relatively new technique, with the first Web of Science result dating back to 1995 when a group of Finnish researchers used three wavelengths (560 to 850 nm) of light to measure PPG signals from dental pulp to assess its vitality [18]. However, after that article it took twelve years (2007) before the research picked new momentum with an article about a laser-based system that used five wavelengths (405 to 1,064 nm) and simple weight-based loading on top of the probe [19]. The different waveform shapes and responses of the different channels for breath holding indicated that the signals originated from different depths of the skin [19]. In 2016, the small time delay, coined as MWPPG pulse transit time (PTT), between the waveforms measured at shorter-wavelengths and those measured at longer-wavelengths (470 to 940 nm) was used to track blood pressure (BP) [20], and was later in 2019 extended to demonstrate systemic vascular resistance tracking [21]. In addition, experimental MWPPG sensors were also presented in 2019 in [22] (460 to 940 nm) and [23], the latter being a chip scale spectrometer based on plasmonic filters (515 to 940 nm). In 2020 and 2021, initial results of the MWPPG sensor (465 to 880 nm) [24] and the subsequent external pressure control and measurement coupled version [25] discussed in this thesis were published, respectively. Model development around MWPPG PTT extraction continued in 2021 [26]. Simultaneously with the MWPPG sensor technology development, Monte Carlo (MC) model simulations investigated the origins and penetration depth of different wavelengths of visible light and NIR [27; 16].

MWPPG research has the potential to provide a broad hemodynamic profile, from large blood-conducting arteries to the vessels of the microcirculation. In recent years, microcirculation has gained more attention in cardiovascular disease (CVD) research, with studies discussing the possible cross-link between micro and macrocirculation in hypertension [28] and increasing evidence of impaired cutaneous microcirculation in many CVDs [29]. This thesis contributes to MWPPG research in the following ways:

- Develops a tonometric fingertip-based method for measuring MWPPG signals under controllable and measurable external pressure. The method was initially implemented as a five-channel system (Publication I) using five LEDs with distinct central wavelengths and a broadband photodiode. It was then expanded to 99 channels by reversing the conventional PPG sensor design, employing a broadband light source paired with a spectrometer (Publication IV).

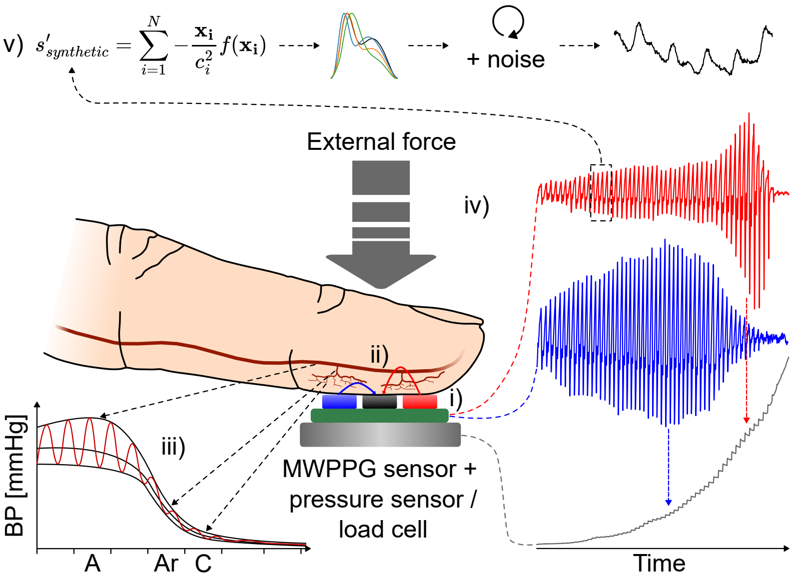

Figure 3. Graphical abstract of the thesis illustrating the key concepts. i) MWPPG sensor technology utilizing the different tissue penetration depth ability of different wavelengths of visible light and NIR. ii) The anatomy of the cutaneous vasculature changes from large arteries buried deep in the tissue into superficial small capillaries. iii) BP decreases in the systemic circulation as the blood vessels get smaller (A = large arteries, Ar = arterioles, and C = capillaries). iv) External pressure exerted on blood vessel walls changes local hemodynamics. As a result, a measurement where the sensor contact pressure is gradually increased (a so-called oscillometric measurement), leads to unique MWPPG signal responses where shorter-wavelength channels (blue light channel in the figure) show maximal pulsation at lower levels of external pressure than longer-wavelength channels (red light channel in the figure). Note that for illustration purposes the presented PPG signals are in fact the AC components extracted with a bandpass filter (to remove the large DC component) and are presented as recorded by the photodiode, i.e. *raw*, with the systolic peaks pointing down. v) Purely synthetic, yet realistic, PPG signals can be generated with a mathematical model.

- Demonstrates the method in experimental measurements to extract depth-resolved BP with effectively the shorter-wavelength channels probing the more superficial lower-pressure blood vessels and the longer-wavelength channels deeper large high-pressure arteries (Publications I and IV). In addition, a MC model is used to gain insights into the results (Publication I).

- Investigates the effects of sensor contact pressure on MWPPG signals, which are typically ignored in most real-world PPG applications (Publication III but also I and IV). Best practices / standards regarding PPG sensor contact pressure are yet to be established [30; 31].

- Develops a parametric model to generate purely synthetic PPG signals with automatic labeling of waveform onsets. The applicability of the model is demonstrated by training convolutional neural network (CNN) models with the generated synthetic signals and then testing the trained CNN models on real-world signals recorded with a developed wearable device (Publication II). Furthermore, the flexibility of the synthetic model is briefly demonstrated by coupling it with another mathematical model modeling oscillometric BP measurements, resulting in a model that essentially generates synthetic oscillograms similar to those recorded in Publications I and IV. At a time of rapid developments in artificial intelligence (AI), realistic synthetic data can help address problems related to biased training data, privacy requirements, and dataset sizes [32; 33].

A graphical abstract presenting the key concepts of this thesis is illustrated in Figure 3.

2 Literature Review

This chapter introduces the relevant literature and theoretical background needed to understand the results presented in Chapter 5. Considering that finger-based PPG measurements are the central unifying element in each publication forming this thesis, the review starts by exploring the structure and optics of the human skin before introducing the concept of PPG. Subsequently, an examination of other optical sensing techniques for the cutaneous vasculature is provided to contextualize PPG. Finally, a brief overview of the techniques available to obtain hemodynamic responses from the cutaneous vasculature is provided, noting that three of the four underlying thesis publications used controlled external pressure as a stimulus.

2.1 Human Skin and Cutaneous Vasculature

2.1.1 Skin Structure

The skin is the largest organ in the human body and acts as a barrier against the surrounding environment. The outermost layer of the skin is the epidermis, which protects against physical, microbial, and chemical attacks. The layer also acts as a regulating layer for water release, preventing dessication. [34] Keratinocytes and melanocytes, the latter responsible for manufacturing and distributing melanin, form approximately up to 90% and 10%, respectively, of epidermal cells [35]. In particular, the epidermis does not contain any blood vessels. The thickness of the epidermal layer varies greatly depending on the body location from as thin as 0.02 mm in the face to 0.8–1.44 mm in friction ridge skin found, for example, on the fingertips [35; 36].

The layer beneath the epidermis is the dermis, which is made up primarily of collagen. The dermis contains a rich set of systems and structures, including lymph channels, nerve fibers, hair folies, sebaceous glands, sweat glands, and blood vessels. [35] The dermis plays an important role in regulating body temperature through sweat glands and superficial blood vessels that act as a thermal radiator [37; 17]. Most importantly, the dermis is home to the cutaneous microcirculation responsible for providing nutrients and oxygen to surrounding tissue and removing metabolic waste products [17]. The thickness of the dermis is between 2–5 mm [38].

The deepest layer of the skin, below the dermis, known as the hypodermis or subcutis, is composed of connective tissue and fat cells [35]. In addition to acting

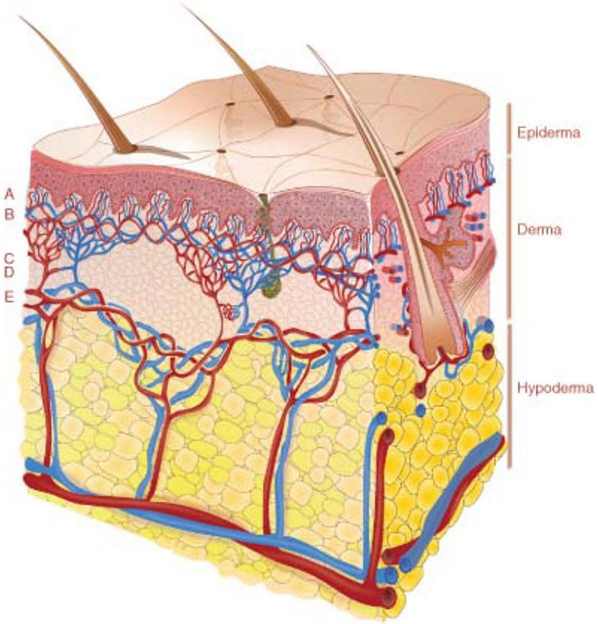

Figure 4. Anatomy of the skin: capillary loops (A), superficial plexus (B), ascending arterioles (C), arteriovenous anastomoses (D), and deep horizontal plexus (E). Reprinted with permission from [38]. Copyright 2020 American Physiological Society.

as an energy storage, fat cells are grouped together by collagen fibers, forming a cushion that absorbs external impacts and thus protects deep tissue [35; 37]. An illustration of the skin structure is presented in Figure 4.

2.1.2 Cutaneous Vasculature

The most intricate structure and functions of the cutaneous vasculature are contained within the dermis. The blood vessels branched from the large vesssels in the deep tissue penetrate the hypodermis and connect to a plexus of horizontal arterioles and venules at the interface of the hypordermis and dermis, as also illustrated in Figure 4. From this plexus emerge ascending arterioles and venules that connect to an upper plexus of horizontal blood vessels in the papillary dermis. Capillary loops arise from this plexus toward the boundary of the epidermis before turning down and changing to post-capillary venules in the same upper plexus. [17] In glabrous skin, found, for example, in the palms and palmar side of the fingers, there are also numerous arteriovenous anastomoses that directly connect arterioles and venules to help regulate body temperature [38; 39]. This terminal vascular network contained within the dermis forms the cutaneous microcirculation, and the microvessels within it are responsible for oxygen transfer to the tissue (more specifically the capillaries), transportation of hormones and nutrients to tissue cells, and removal of metabolic byproducts. Microcirculation also plays a role in mediating the immune system and maintaining the proper function of parenchymal cells. Due to these vital functions, microcirculation is argued to be the most important compartment of the cardiovascular system. [40]

The blood vessels in the microcirculation are the smallest in the human body, consisting of the smallest resistance arteries (diameter < 150 µm), arterioles, capillaries and venules [38]. The capillaries have an inner diameter below 10 µm, whereas the diameter of arterioles varies from approximately 15 µm just before the capillaries up to approximately 100 µm at the border of the dermis and hypodermis [17; 41]. The venous counterparts, venules, are somewhat larger [41].

The structure of the blood vessel varies between the different types. Capillaries and postcapillary venules are essentially tubes consisting of a single layer of endothelial cells that are in direct contact with the blood, surrounded by the basement membrane [41]. The basement membrane of capillaries has cells called pericytes that allow the regulation of vessel diameter and, therefore, vascular tone [38; 41]. Arterioles and arteries instead have a more complex structure, although the inner layer similarly consists of a single layer of endothelial cells. The surrounding layer consists of predominantly vascular smooth muscle cells (VSMCs) which can modulate the diameter of the vessels, and thus vascular tone. The volume fraction of VSMCs increases as the vessel diameter decreases, increasing the ability to modulate vessel diameter. [38] Importantly, VSMCs are in close proximity to the endothelium, making frequent tight junctional contacts, which is crucial in the regulation of vascular tone [38; 17]. The outermost layer consists of, for example, elastin and collagen, which provide structural support. In the cutaneous microcirculation, this layer also has a high density of sensory, sympathetic, and parasympathetic nerve fibers that pass close to VSMCs, and thus together play a significant role in the regulation of vascular tone. [38]

The blood vessels of the microcirculation are indeed crucial in the regulation of blood flow. Approximately 80% of the total pressure drop from the aorta to the vena cava occurs within these vessels, with the steepest pressure gradient found in the arterioles [41], as illustrated in Figure 5. In the arteriolar segment of the capillary loop, the blood pressure is approximately 40 mmHg [42], while in the capillary it ranges from approximately 10 to 20 mmHg [42; 43; 44; 45].

2.1.3 Cutaneous Microcirculation in Disease

Many diseases are associated with impaired microvascular function, such as coronary artery disease (CAD), diabetes mellitus, obstructive sleep apnea, heart failure, obesity, and hypertension [47], and several studies have investigated the link between CVDs and cutaneous microcirculation [48; 49; 50; 51]. For example, CAD patients have shown impaired microvascular function in reactivity tests performed with laser

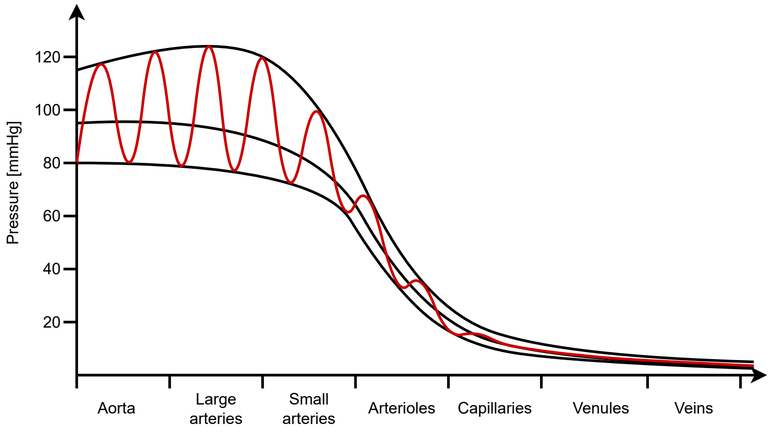

Figure 5. BP in the different blood vessels of the systemic circulation, based on [46]. The largest pressure drop occurs in the arterioles that regulate the blood flow to be suitable for the capillary functions.

Doppler flowmetry (LDF) and laser speckle contrast imaging (LSCI) [52; 51] while hypertensive patients have shown reduced skin blood flow [53] and vasoreactivity [54], and impaired recruitment of perfused capillaries [55]. However, it is still unclear whether microvascular dysfunction is responsible for the development of cardiometabolic diseases or is a result of it [38]. In hypertension, for example, microcirculation and macrocirculation are tightly interconnected, forming a vicious circle where increased total peripheral resistance due to microvascular alterations increases the mean BP. Then again, this has damaging effects on the microvasculature over time, leading to an even greater increase in total peripheral resistance and mean BP [28].

Taking into account the increasing evidence for impaired skin microcirculation in many CVDs, the possibility of it as a model of generalized microvascular function has been presented [56]. However, studies, although numerous, are still not able to provide sufficient evidence to draw such conclusions considering their heterogeneity in methods, differences in patient populations, and even weaknesses in study designs [38]. Thus, more studies are needed to further investigate the link between skin microcirculation and diseases. The non-invasive access of skin microcirculation ensures its attractiveness for technological and clinical research.

2.2 Tissue Optics

2.2.1 Optical Properties of the Skin

The propagation of light within a turbid medium such as the skin is defined by reflection, refraction, scattering, and absorption. In the spectrum of visible light, ap-

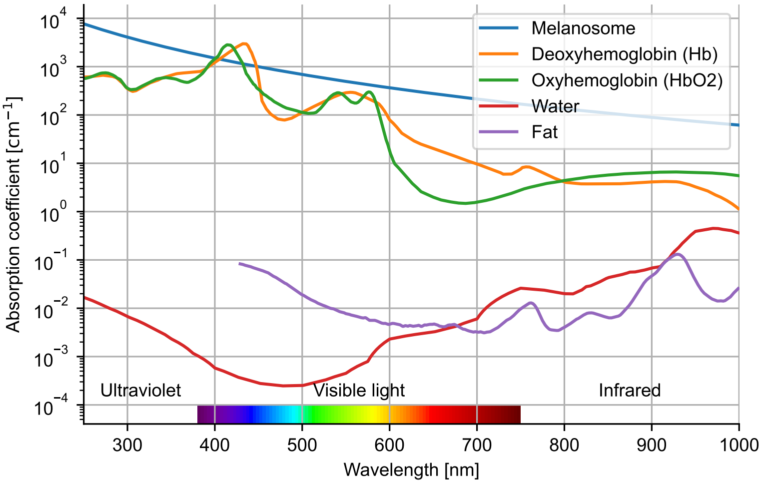

Figure 6. Absorption coefficients of some of the main skin chromophores as a function of wavelength. The figure is based on the data collected by Steven Jacques and Scott Prahl and published on their website [60; 61; 62; 63].

proximately 4–7% is reflected by the surface of the skin, while the remaining portion is refracted [57; 58]. Therefore, at the boundaries of different media, the refractive indices determine how light propagates from one layer to another [35]. While light propagates in the skin, it experiences scattering events that alter the direction as a result of interaction with small regions with optical properties that differ from the surroundings [58]. Only a very small fraction of the light is inelastically scattered (i.e., with a change in wavelength), while the vast majority (more than 99%) is elastically scattered [35]. The propagation can result in either photons escaping the skin into the outside medium (e.g., air) or absorption by the medium where the photon energy is thermally dissipated [35].

The interaction of light with the skin is, therefore, determined by the optical properties of the skin. In the epidermis and dermis, absorption in the spectral range of visible light, see Figure 6, is mainly determined by melanin and blood (in practice hemoglobin and its derivatives), respectively, [35; 59] while water dominates in the NIR range [35]. In the hypodermis, lipids are the strongest chromophores in the visible and NIR range [59]. Scattering is higher in the epidermis than in the other two skin layers due to the epidermal melanin content. In the dermis, scattering is dominated by collagen fibers, with collagen also playing a role in the scattering properties of the hypodermis along with elastin. In general, scattering dominates absorption by at least one order of magnitude in the visible and NIR part of the spectrum [35].

2.2.2 Beer-Lambert Law

Beer-Lambert law (BLL) is commonly used to analyze light attenuation through a sample, defining absorbance or optical density (OD) as [64; 65]:

$$\mathrm{OD} = \log\left(\frac{I_0}{I}\right) = \epsilon \cdot c \cdot d = \mu_a \cdot d, \tag{1}$$

where I is the transmitted intensity, I_0 is the incident light intensity, ϵ is the molar extinction coefficient, c is the molar concentration, d is the sample thickness, and μ_a is the sample absorption coefficient. However, the law assumes that attenuation is dominated by absorption, and if instead scattering is significant, the trajectories of the photons passing through the sample are much greater than the straight line distance d between the light source and the detector, as illustrated in Figure 7a. [64] Note that the figure essentially describes the configuration of a transmissive PPG sensor (discussed later in Chapter 2.3).

A modified version of the Beer-Lambert law was introduced in [66] to take into account the fact that scattering is indeed significant in human skin tissue, given as:

$$\mathrm{OD} = \log\left(\frac{I_0}{I}\right) = B \cdot d_p \cdot \mu_a + G, \tag{2}$$

where B is a pathlength factor dependent upon the absorption and scattering coefficients μ_a and μ_s, and the scattering phase function (in practice an experimentally determined correction factor for d_p), d_p is the distance between the light source and the detector, and G is an unknown geometry dependent factor. However, because a simple parameter B does not consider the empirically observed non-linear relationship between OD and μ_a, and G is typically unknown, Equation 2 is commonly not used as such [66]. Instead, the differential version of the modified BLL is used to relate an infinitesimal change in OD to a change in absorption, given as [67]:

$$\delta\mathrm{OD} = \langle L\rangle \delta\mu_a, \tag{3}$$

where $\langle L\rangle$ is the differential pathlength [68; 64], which is the mean pathlength of detected photons [67; 64; 65], and depends on μ_a, μ_s, source-detector configuration, scattering phase function and the geometry of the medium [67]. The only assumption in the equation is that changes in μ_a are spatially uniform [67]. The dimensionless ratio of $\langle L\rangle / d_p$ is known as differential pathlength factor, DPF [69; 67]. Thus, an infinitesimal change in OD is given as:

$$\delta\mathrm{OD} = \mathrm{DPF} \cdot d_p \cdot \delta\mu_a. \tag{4}$$

For a finite change:

$$\Delta\mathrm{OD} = \mathrm{DPF} \cdot d_p \cdot \Delta\mu_a, \tag{5}$$

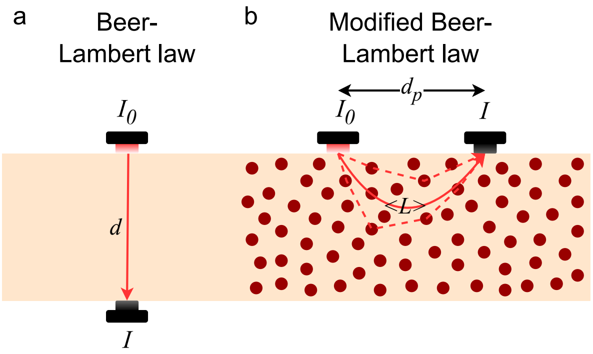

Figure 7. Beer-Lambert law (BLL). a. BLL assuming a non-scattering tissue and transmissive measurement where the light source and the detector are placed on the opposite side of the sample. b. Modified BLL assuming a scattering tissue and reflectance measurement where the light source and the detector are placed on the same side of the sample. Reflectance mode measurement relies on backscattering where light is scattered back from the tissue into the detector.

where:

$$\Delta \mathrm{OD} = \log\left(\frac{I_0}{I_2}\right) - \log\left(\frac{I_0}{I_1}\right) = \log\left(\frac{I_1}{I_2}\right), \tag{6}$$

and thus Equation 5 becomes:

$$\log\left(\frac{I_1}{I_2}\right) = \mathrm{DPF} \cdot d_p \cdot \Delta\mu_a, \tag{7}$$

where I_1 and I_2 are the detected light intensities at two different states of tissue [65]. Values of DPF have been defined experimentally under different conditions, and varies typically between 3 and 6 for tissue [69]. The modified BLL is illustrated in Figure 7b, and in essence describes the configuration of a reflectance PPG sensor (discussed later in Chapter 2.3).

In conclusion, according to the modified BLL, changes in detected light intensity are primarily related to changes in the absorption properties of the medium. The modified BLL has been used, for example, to extract blood flow information from diffuse correlation spectroscopy measurements [64] and to extract arteriolar pulse from reflectance MWPPG signals using a layered tissue model with a layer-wise absorption weighting system [20].

2.2.3 Monte Carlo Photon Propagation Modeling

Light transportation in tissue can be modeled using an MC based computational method where packets of photons are recorded as they scatter and absorb in tissue, governed by statistical sampling of probability density functions. The photon packets

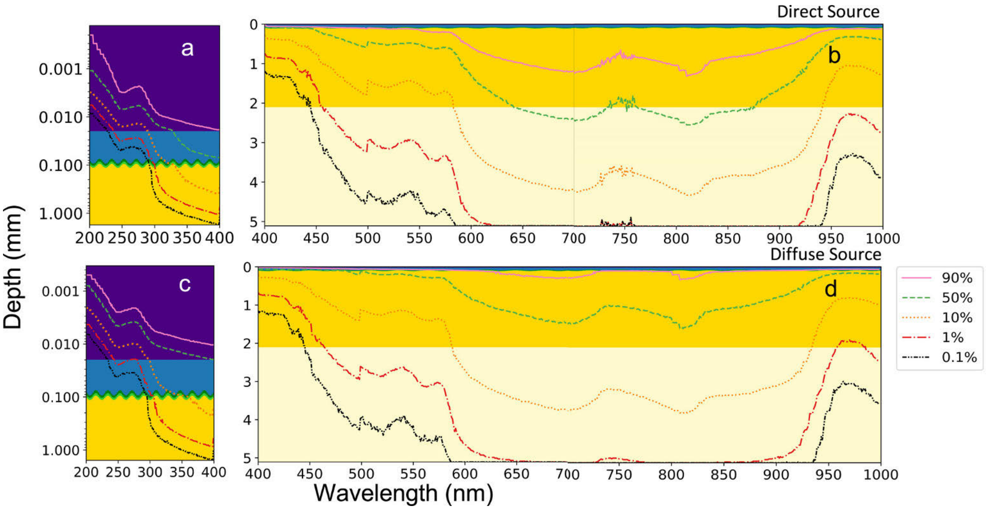

Figure 8. Simulated fluence rates for a 6-layer skin model with the dark yellow representing the dermis and the light yellow subcutaneous fat. The figure shows values for both direct and diffuse light sources with different fluence rates as a percentage of the incident light value. The figure is from [16], used under CC BY.

are launched one-by-one into a tissue being modeled, and each packet is propagated in a series of small steps during which they can scatter, absorb, reflect internally or transmit out of the tissue. The propagation of a photon packet continues until it is either absorbed by the tissue or transmitted out of the tissue. [70] The details of MC light propagation are extensively discussed in [70; 71; 72; 73].

The input to an MC model is a tissue volume that specifies the 3D shape of the sample and the different types of tissue within it. The tissue volume can have several layers of different types of tissue [71] and even arbitrary shapes with heterogeneous tissue properties can be modeled by constructing the tissue model from volumetric pixels known as voxels [72]. Different light sources (e.g., Gaussian beam, laser beam, and isotropic source) can also be easily included in the simulation model. The assumed light source dictates the initial trajectory for a photon packet. For example, in the case of a laser beam, the initial trajectory is typically assumed to be downward perpendicular to the tissue model.

When the optical properties of the skin (see Figure 6 for absorption coefficients of some of the main skin chromophores) are mapped with tissue volume and the characteristics of a light source, it is possible to estimate the penetration depth of light into the skin by launching a large number of photon packets into the tissue volume. In general, the penetration depth of light into the skin increases with increasing wavelength in the visible-light range [16]. This is due to the monotonically decreasing melanin absorption and simultaneously decreasing hemoglobin absorption [35]. At approximately 600 nm there is a steep decrease in hemoglobin absorption, resulting in a steep increase in penetration depth [16]. The penetration ability begins to decrease after approximately 900 nm [16], at which point the absorption due to water and lipids begins to gradually increase [35]. The wavelength range of 600–1,300 nm is commonly known as an optical window because of the increased penetration depth of light into the skin [35; 74]. Figure 8 presents the simulated fluence rates for a six-layer tissue model and for different thresholds of the incident light value according to [16]. Assuming that the optical penetration depth is the point at which the incident light has attenuated to approximately $1/e$ ($\approx$ 0.37) [75], penetration depth of light ranges from the upper part of the dermis for wavelengths below 450 nm to perhaps slightly into the subcutaneous fat for wavelengths between 800–850 nm, assuming a diffuse light source. For a direct light source the penetration depths are greater. Note that besides the type of the light source, the estimated penetration depths are greatly affected by the assumed tissue volume (e.g. thicknesses of different layers) and optical properties (e.g. concentration of blood).

2.3 Photoplethysmography

PPG is an optical technique in which the skin is illuminated with a light source and variations in light intensity caused by changes in blood volume are recorded with a photodetector [1]. As a non-invasive and easy-to-use technique (the only minimum requirement is sufficient skin contact), PPG sensors are widely used to monitor human cardiovascular activity, especially in wearables, such as smart watches and smart rings. The sensor can be constructed to work in transmissive or reflectance mode, as shown in Figure 10, where the former refers to sensors where the probed tissue is placed between the light source and the photodetector, and the latter refers to sensors where the light source and the photodetector are located next to each other, with both components facing the tissue [76]. Reflectance mode sensors are more typical in practical applications, as the sensor construction allows free placement on the body with sufficient vasculature, for example wrist, temple, ear canal, chest, and fingers. Clinical applications typically use finger or toe clip form factor with the transmissive mode sensor configuration to ensure that the signal is influenced by the large arteries [77], considering that the detected light passes completely through the finger/toe.

PPG signal consists of a large non-pulsatile quasi-DC component and a superimposed pulsatile AC component [1; 76], as illustrated in Figure 9. The terms DC and AC are borrowed from electromagnetism, where they are used to describe constant or slowly varying and periodically varying current/voltage, respectively. The ratio of the AC amplitude to the baseline DC level ranges from less than 1% to greater than 10% [78]. In fact, this AC/DC ratio is also known as the perfusion index and, as suggested by the name, is used as an estimate of perfusion. The DC component is related to the tissue composition and the average blood volume [1; 76] and to external and device-specific factors [76], such as ambient light and the brightness of the light

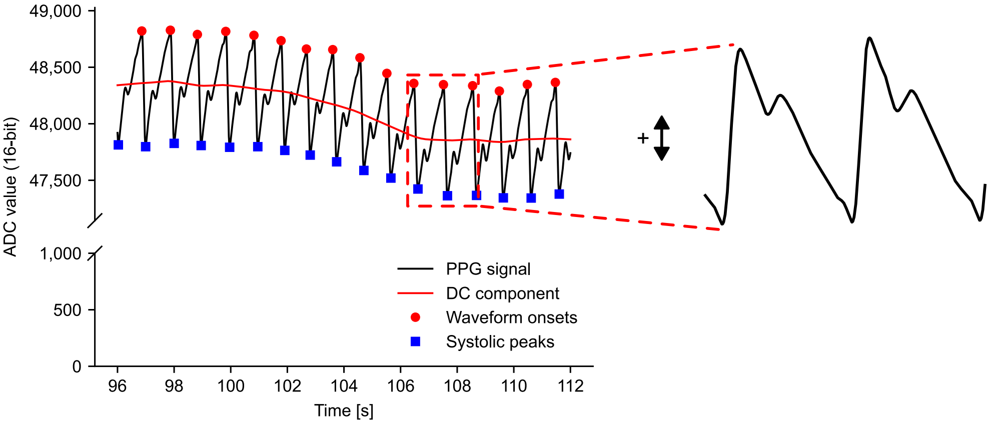

Figure 9. An example of a typical PPG signal together with its DC component and markers for the waveform onsets and systolic peaks. The zoomed-in section shows two waveforms inverted so that the systolic peaks point up – a style often used in PPG waveform illustrations. The PPG signal has been filtered with a lowpass filter with a cutoff frequency set at 8 Hz to remove high frequency noise. The DC component has been extracted with a lowpass filter with a cutoff frequency set at 0.5 Hz.

source (i.e., LED driving current). The DC component is influenced by vasomotor activity, breathing, and Traube-Hering-Mayer waves [1; 76].

The AC component varies with the beating of the heart, decreasing during systole as blood is pushed through the aorta to the periphery and increasing during diastole. However, because of similarity with the arterial pressure waveform, PPG AC waveforms are often inverted so that the systolic peak points up, as illustrated in Figure 9. Unsurprisingly, heart rate (HR) and HRV are typical parameters along with the respiratory rate to extract from the AC component. However, the waveform contains a significant amount of additional information, and the branch of research studying the waveform morphology is known as pulse wave analysis (PWA). PWA is based on extracting numerous features from the waveform using the characteristic points (e.g., systolic peak, dicrotic notch, and diastolic peak) of the waveform, revealing information on the cardiovascular state [77]. PPG features have been shown to provide information on arterial stiffness / aging, stroke volume, systemic vascular resistance, and BP [79; 77]. PPG has also been used to extract jugular venous pulse from the neck [80].

An important application of PPG is the pulse oximeter which is widely used in clinical settings to monitor SpO_2. The technique uses two wavelengths from red and NIR part of the electromagnetic spectrum, and utilizes the difference in oxyhemoglobin and deoxyhemoglobin absorption by selecting the two wavelengths from both sides of the isosbestic point at approximately 800 nm (see Figure 6), i.e., de-

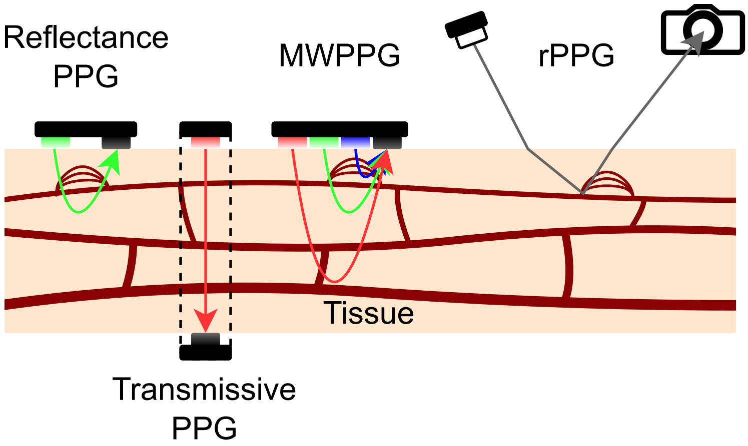

Figure 10. Photoplethysmography (PPG)-based sensing techniques. i) In a reflectance PPG sensor, the LEDs and the photodiode(s) are next to each other on the skin. ii) In transmissive mode, the LEDs and the photodiode(s) are on the opposite side of the measurement site. In practice, this limits the configuration to thin extremities of the human body, i.e. fingers, toes and ear lobes. iii) Multi-wavelength photoplethysmography (MWPPG) sensors have several LEDs with each emitting light at different wavelength. The sensor configuration is in practice limited to reflectance mode if shorter wavelengths of light (approximately wavelengths below red light) are used. iv) Remote photoplethysmography (rPPG) technique uses an external light source or even ambient light to illuminate the skin and a camera to record the faint pulsations of the cutaneous blood vessels.

oxyhemoglobin absorbs more red light than IR and oxyhemoglobin absorbs more IR than red light. The ratio

$$R = \frac{AC_{red}/DC_{red}}{AC_{IR}/DC_{IR}} \tag{8}$$

can be accurately related to SpO_2 by performing a clinical calibration over a wide range of SpO_2 values.

Finally, the working principle of PPG can be explained with the modified BLL. In the context of PPG, I denotes the unprocessed PPG signal recorded by the photodetector, as shown in the Figure 7b for a reflectance PPG sensor. Assuming a steady-state measurement condition where $\langle L \rangle$ remains constant (essentially neglecting changes in the scattering coefficient, e.g. due to moving red blood cells (RBCs)), variations in the PPG signal are primarily attributed to changes in tissue absorption (Equation 5), predominantly from blood absorption. This is because within the visible and NIR spectrum, hemoglobin is a major absorber (see Figure 6), and, moreover, the volume of blood at any given time is modulated by the pumping activity of the heart. Thus, the signal I reflects blood volume changes over time.

2.3.1 Multi-Wavelength Photoplethysmography

MWPPG is the simultaneous application of the PPG technique to multiple wavelengths of light, as shown in Figure 10. A typical MWPPG sensor consists of a wideband photodiode and several LEDs with different wavelengths driven one after another using time-multiplexing. Currently, there is no single definition for the number of different wavelengths a sensor should have to be labeled as MWPPG. For example, in multispectral and hyperspectral imaging, the former refers to devices recording fewer than 20 non-continuous wavelengths, while the latter refers to devices recording a large number, over 20, equally distributed wavelengths [38]. Although such definitions do not help to draw a line on how many channels MWPPG sensors should have at minimum, they do imply that all LED and photodiode based sensors, regardless of the number of channels, would in practice be MWPPG sensors because it is unlikely that the different LED spectra would be evenly spaced from each other. Then again, under such a definition, spectrometer-based MWPPG sensor configurations, as discussed in this thesis, would deserve a new term, *hyperspectral PPG* given (very close to) equal wavelength spacing and number of wavelengths close to a hundred or possibly even more. In the opinion of the author of this thesis, an *MWPPG sensor* should include at least three wavelengths to distinguish it from dual-channel pulse oximeters. Based on the results presented later in this thesis, an even more restrictive definition could be justified to require that sufficient parts of the spectrum containing different physiological information are included, meaning that MWPPG sensors should have wavelengths at least in the blue, green, yellow, and red light and NIR part of the spectrum.

The dependency between the wavelength of light and the penetration depth ability into the skin, as detailed in Section 2.2.3, and the structure of the cutaneous vasculature, as detailed in Section 2.1.2, are the reasons for developing MWPPG sensors. Longer wavelengths, such as red light and NIR, are able to penetrate down to the large blood-conducting arteries buried deep in the tissue, while shorter wavelengths, such as blue and green light, can only probe the smaller, more superficial blood vessels, namely capillaries and arterioles. A practical demonstration of this are the experimental results showing that PPG waveforms measured with blue light are delayed compared to the waveforms measured with NIR [81; 24; 25]. Thus, PPG signal information content depends on wavelength, and since MWPPG sensors typically contain LEDs with peak wavelengths at the shorter and longer ends of the visible light spectrum (or even NIR), information from different depths and thus different parts of the vasculature can be obtained simultaneously. The use of shorter wavelengths of light (in practice wavelengths shorter than the red light), actually means that MWPPG sensors typically work in reflectance mode because shorter wavelengths of light are not able to penetrate through fingers and toes, where transmissive PPG sensors are typically attached.

Early MWPPG research with five wavelengths from 405 to 1,064 nm showed that the channels show different waveform shapes and respond differently to breath holding and increasing probe contact pressure [19]. Another early research study showed that skin and muscle perfusion can be separately measured using green light with short LED-photodetector distance and IR with long LED-photodetector distance, respectively [82]. Indeed, in addition to wavelength, the distance between the light source and the photodector is a factor that affects PPG penetration depth, with greater distances leading to higher penetration depths [27].

MWPPG has in recent years seen steady increase in research activity. The aforementioned delays between the MWPPG waveforms have been used to extract arteriolar PTT with the aim of it being a single-point alternative to the more common PPG and electrocardiography (ECG) based pulse arrival time (PAT) [20]. Later the same research group demonstrated the delays in continuous MWPPG-based BP measurement [21]. The feasibility of MWPPG based blood glucose monitoring by estimating glycated hemoglobin levels has also been studied [83] as well as automatic illumination adapting to the skin type (from light to dark) [84]. Recently, perhaps on the more technical side, the coupling of MWPPG sensors with systems enabling the variation of the sensor contact pressure to extract oscillometric measurements has been demonstrated in [85] and in the publications leading to this thesis [25; 86; 87]. Recent technical advances also include spectrometric approaches in which the sensor configuration is effectively reversed: the photodiode is replaced with a spectrometer and the several LEDs are replaced with a wideband light source. Both plasmonic filter-based on-chip spectrometers [23; 88] and laboratory grade spectrometers [87] have been demonstrated.

2.3.2 Remote Photoplethysmography

Remote photoplethysmography (rPPG), as illustrated in Figure 10, is a technique that applies the principles of PPG to a remote monitoring system using a video camera instead of a sensor in direct contact with the skin [89; 90]. This allows contactless monitoring in situations where a subject, such as a person driving a car [91] or a neonate in an incubator [92], cannot be assumed to conveniently maintain contact with a PPG sensor. The illumination can vary from ambient illumination to an artificial light source or some sort of combination [93]. The video camera can range from high-speed cameras to low-cost webcameras, with a typical sampling rate of 30 fps or less [93]. The vast majority of studies use cameras with typical red, green and blue channels, although, e.g., five-band cameras [94] and cameras working in the NIR region [95] have also been demonstrated.

The general pipeline for processing video frames into a plethysmogram includes signal extraction and signal estimation phases [96]. In the signal extraction phase a region of interest (ROI) is detected from the frames, the face being the typical target as it is usually not covered and is well perfused [93]. The face is commonly detected using machine learning (ML) methods, after which the final ROI is defined as the whole face or some subset of pixels or even multiple subsets of pixels in the case of a dynamic ROI [96]. The ROI is then tracked through every frame as the subject moves, and from each frame a raw signal is extracted using spatial averaging for each color channel [90; 96]. In the signal estimation phase, individual signals are filtered to remove unwanted noise before using one of the color channels, typically the green channel, or a combination of the channels (dimensional reduction) [90; 96; 93]. Typical methods to combine channels include blind source separation methods (e.g., principal component analysis and independent component analysis) and model-based methods (e.g., skin illumination models) [96; 93]. Heart rate is the most commonly calculated parameter, but rPPG signals have also been used to extract HRV, respiratory rate, and SpO_2, to detect atrial fibrillation [97] and to extract the jugular venous pulse [98].

The rPPG signal quality and the accuracy of the parameters are generally not as good as with contact PPG due to the inherently greater number of error sources, especially movement-related errors [95]. Furthermore, the probing depth of rPPG is less than in contact PPG [99], which likely contributes to errors with respect to contact PPG. Moreover, especially in SpO_2 estimation the typical 3-channel RGB camera is challenging because it forces to use the blue or green channel in combination with the red channel, and, as described earlier, such a pair probes different parts of the vasculature, with the blue/green channel mostly modulated by the arterioles, while the red channel is modulated by the large arteries [99].

2.3.3 Synthetic Photoplethysmography Signals

Synthetic data is data that does not originate directly from the observable real world, that is, does not result from a real-world process. Instead, synthetic data is generated using models that try to replicate some real-world process. Synthetic data has become a prominent alternative to gathering large dataset required by AI models, providing unbeatable cost effectiveness given that data can be generated instantly as required. Synthetic data can also help address the problem of bias in medical data, which can arise due to homogeneous study participants (e.g., socioeconomic factors, gender, and age), and imbalanced classes. Even the use of a single type of device, such as PPG sensor, can lead to a situation where the data does not generalize well. [32] Finally, data privacy aspects are ever more important as regulators tighten the rules related to data, such as the General Data Protection Regulation (GDPR) 2016/679 of the European Union (EU).

There are several techniques to generate synthetic data, including ML-based generative models (e.g. generative adversarial networks (GANs)), parametric models, and physical simulations [32; 100]. Parametric models and physical simulation models generate inherently privacy-secure data assuming that the models are purely mathematical. With regards to PPG signals, synthetic signals have been created using parametric models that combine Gaussian functions [101; 102; 103] or Gaussian functions with log-normal functions [104]. These models reconstruct the PPG pulse waveform by adjusting the parameters of the Gaussian function so that the collective bumps form the intended waveform. In addition, more intricate physiological PPG models have been devised, which simulate cardiac function, including the heart chambers, valves, and systemic circulation [105]. GAN models producing synthetic PPG signals have also been demonstrated [106].

2.4 Other Optical Sensing Techniques of the Cutaneous Vasculature

2.4.1 Near-Infrared Spectroscopy

Near infrared spectroscopy (NIRS), visualized in Figure 11, also sometimes referred to as diffuse optical spectroscopy (DOS), leverages the property that biological tissues scatter and absorb less electromagnetic radiation in the NIR spectrum compared to the visible light range [107], enabling a relatively deep penetration depth of a few centimeters [108], even up to 8 cm [109]. There are three types of NIRS, namely continuous wave, frequency domain, and time domain. Continuous wave NIRS illuminates the sample with constant intensity and measures changes in the intensity of the detected light. The frequency-domain technique modulates the emitted light intensity and measures both the intensity and phase shift of the detected light, with the phase shift corresponding to the time of flight of the photons, which is the time it takes from the photons to propagate through the sample. The time-domain technique measures this time directly by emitting very short pulses of light into the tissue and recording the arrival time of the photons. [108; 109; 110]. The time of flight information provides rich information about the tissue properties and can be used to extract absolute values for oxy- and deoxyhemoglobin concentrations. In contrast, the continuous wave technique can only measure changes in concentrations, but has a significantly simpler design, a lower cost, and is easy to use [108; 110]. The following text focuses on the continuous wave technique which is the most prevalent of the three.

In its simplest form, the construction of a NIRS system reminds that of a PPG system, requiring only an LED and a photodiode. Similarly to a pulse oximeter, by having at least two wavelengths around the isosbestic point of oxyhemoglobin and deoxyhemoglobin at around 800 nm, tissue oxygenation can be computed [108]. The optimal wavelengths tend to be within the optical window ($\approx$ 650–950 nm) where NIR absorption by tissue components is low (see Section 2.2.1). The exact optimal two wavelengths are debatable, for example, $<$ 780 nm and 830 nm or 704 nm and

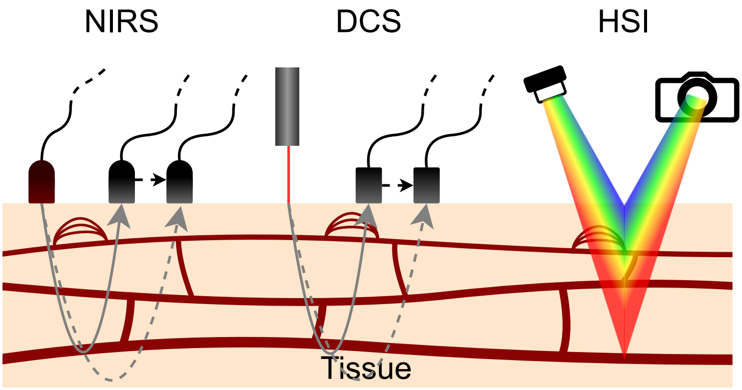

Figure 11. Spectroscopy-based techniques, from left to right. i) Near infrared spectroscopy (NIRS) uses an NIR emitter and a photodetector to probe deeper tissue. Besides the selection of wavelengths, also the distance between the emitter and detector is a defining factor. ii) Diffuse correlation spectroscopy (DCS) uses a long-coherence laser and a photon counting device. iii) Hyperspectral imaging (HSI) uses a wideband light source and a hyperspectral camera.

887 nm [108]. By employing three or more wavelengths, it becomes possible to separate more chromophores, such as oxyhemoglobin, deoxyhemoglobin, and water.

As with PPG, the distance between the light source and the detector is also an important factor to consider, as it affects the probing depth, with longer source-detector distances being more sensitive to deeper tissue [108]. Several different source-detector distances can be used simultaneously, enabling image reconstruction. Although NIRS terminology can be loose, systems with more than four channels and capable of producing 2D images are called infrared topography, while systems capable of producing 3D images are called infrared tomography. The latter is also known as diffuse optical tomography or diffuse optical imaging. [108]

NIRS is extensively used in brain function monitoring, where the technique is known as functional NIRS (fNIRS). The technique is able to detect relative changes in oxyhemoglobin and deoxyhemoglobin concentrations in response to increased cerebral blood flow. The increase in blood flow is caused by activation of a certain brain area in response to the execution of a task to meet the increased metabolic demand for oxygen and glucose [110]. Other uses of NIRS include assessing tissue oxygenation [111] and muscle oxygenation [112], the latter made possible by the deep penetration ability of NIRS.

2.4.2 Diffuse Correlation Spectroscopy

Similarly to NIRS, DCS, visualized in Figure 11, uses NIR radiation for deeper penetration ability, but unlike in NIRS, the source is a laser. An important property of the laser is the coherence length (typically $\sim$10 m), which should be longer than the spread of the path length distribution of the photon trajectories defined by the optical properties of the tissue and the source-detector distance, which can even be a few centimeters. [113] The coherent light endures multiple scattering in tissue resulting in an interference pattern known as the speckle pattern (see Section 2.4.5 for more details). The moving RBCs in the blood vessels buried in the tissue alter the pattern causing it to fluctuate rapidly [114]. These fluctuations can be detected with a photomultiplier, but more often a single-photon counting avalanche photodiode is used [113]. By collecting photons from a single speckle / few speckles, intensity variation over time can be recorded and used to calculate a temporal autocorrelation function [113; 114; 115], which is related to the motion of scatterers, i.e., RBCs [114; 116; 115].

Given that the technique measures RBC movement, it provides a measure of blood flow [116], and is commonly used to measure cerebral blood flow but also other tissue blood flow [116], for example, in tissue flaps [117]. DCS can be extended to tomography, known as diffuse correlation tomography (DCT), using arrays of sources and detectors [117; 115].

2.4.3 Hyperspectral Imaging

HSI, visualized in Figure 11, is an imaging technique that provides 2D images with spectral information in each pixel. In essence, the output is a 3D dataset, also known as a hypercube with 2D spatial information and 1D spectral information in each spatial point. [118; 119] The spatially-resolved spectral content enables the discrimination or classification of samples, which is not possible with conventional color imaging techniques. [118] A closely-related technique to HSI is multispectral imaging, which differs with respect to the channel capabilities. HSI typically refers to devices recording a large number, over 20, equally distributed channels (wavelength bands), while multispectral imaging systems have fewer than 20 noncontinuous channels [38].

There are three main types of HSI techniques: spectral scanning method, spatial scanning, and snapshot imaging [118]. In spectral scanning, 2D images are obtained one-by-one for different wavelength ranges by adjusting the wavelength of light either at the detector (camera) or illumination side with spectral filters. In spatial scanning, a spectrometer is used to obtain spectral data from a single point, and then spatially scanned across the desired target region. Finally, in snapshot imaging, multiple narrow-band filter arrays are placed on top of a camera sensor to obtain both spatial and spectral information without any scanning. Compared to the scanning methods, it is fast but compromises spatial and spectral resolution. [118]

The spectral ability of HSI provides information about the different tissue chromophores, which can be used in disease screening, detection, and diagnosis [120; 121]. The spectral data can be used to assess tissue perfusion and blood oxygenation [120], for example to quantify tumor angiogenesis and tumor metabolism [121]. Besides cancers, HSI has also been used to detect diabetic foot ulcers and peripheral vascular disease [120].

2.4.4 Laser Doppler Flowmetry

LDF technique, as illustrated in Figure 12, is based on illuminating the tissue with a monochromatic laser light and detecting the Doppler frequency shift caused by moving RBCs scattering the light. The concentration of the RBCs affects the fraction of Doppler-shifted light, whereas the average velocity of the RBCs affects the magnitude of frequency broadening. Commercial LDF systems, however, report only a single value that, under ideal conditions, reflects the product of these two properties of RBCs. [122; 123] The recorded values, or flux, are reported in arbitrary units, i.e., the technique cannot provide values in absolute, physiologically meaningful, units [123]. Monte Carlo modeling has shown that the penetration depth of LDF is less than 1 millimeter [122].

LDF is an established method for measuring microcirculatory blood flow, not only from the skin but also from, e.g. muscle, brain and liver tissues [122], and is accurate in measuring fast changes in skin blood flow, but suffers from a small probing volume of just 1 mm^3. Together with the heterogeneity of skin perfusion, LDF shows great spatial variability and relatively poor reproducibility. An extension of the technique, laser Doppler imaging (LDI), tackles this by scanning the area of interest with the laser beam, producing 2D images. However, the technique is slow and, thus, fast changes in skin blood flow are difficult to measure. [124]

2.4.5 Laser Speckle Contrast Imaging

LSCI, visualized in Figure 12, uses a laser light source to illuminate a diffuse object and registers backscattered light with a camera with a limiting aperture in front of it. The aperture causes diffraction of the coherent light that is observed by the camera as speckle patterns. If the object contains mobile scatterers, such as red blood cells in biological tissue, the speckle patterns fluctuate in intensity because of (constructive and destructive) interference of light waves as they recombine, assuming an exposure time longer than the speckle fluctuation time. This causes the speckle patterns to blur and thus a reduction in the speckle contrast, i.e., a pattern of bright and dark areas, is observed. [125; 126; 127] Given the random nature of the speckle phenomenon, it can only be described statistically [126]. An important measure in LSCI is speckle contrast, which is defined as:

$$K(x, y) = \frac{\sigma_N}{\mu_N}, \tag{9}$$

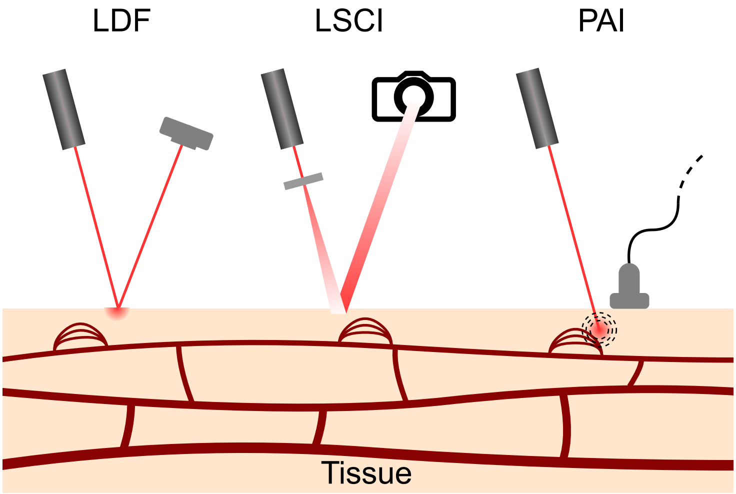

Figure 12. Laser-based techniques. i) Laser Doppler flowmetry (LDF) uses a laser coupled with a photodetector. ii) Laser speckle contrast imaging (LSCI) uses a laser and a camera. iii) Photoacoustic imaging (PAI) uses a laser and an ultrasound transducer to detect the pressure waves due to thermoelastic expansion.

where σ_N and μ_N are the standard deviation and mean of the pixel intensities around the pixel $P(x, y)$ given a neighborhood of N pixels [125; 126]. Typically N of 5 or 7 is used as a compromise between statistics and spatial resolution [126]. Importantly, this measure, K, is inversely related to scatter flow velocity, and as a result the blood vessels carrying the flow of red blood cells appear darker against a lighter background [125]. In addition to blood flow dynamics, LSCI can also be used to study the vascular structure due to its highly detailed images of the vasculature.

Although LSCI has attracted a lot of attention in recent years, the underlying technique dates back to the 1960s. In the early 1980s, the technique attracted renewed attention in terms of the underlying mathematical theory, and by the 1990s digital technology had sufficiently advanced, allowing digital imaging methods. [126] Nowadays LSCI is mainly used in the medical field in cerebral blood flow monitoring, dentistry, wound and burn assessment, and microcirculation research. In microcirculation research, LSCI can visualize superficial microvascular flow with a spatial resolution of tens of micrometers. The camera-based approach also allows for a wide field of view, and assuming a fast camera, the technique essentially combines the advantages of LDF and LDI, namely good temporal and spatial resolutions, respectively [124]. Furthermore, compared to LDI and its scanning technique, LSCI is simple and inexpensive because it requires only a laser diode and a digital camera [128]. The drawback of LSCI is its sensitivity to movement artifacts that decrease the speckle contrast [124; 129].

Speckle plethysmography (SPG) is a subset of LSCI in the sense that it is based on the analysis of video frames produced by an LSCI system, with the end result being a single value for each video frame [130]. The resulting timeseries, i.e. SPG signal, reminds a lot of PPG signal, as visualized in [130], but they indeed have a fundamental difference in that PPG signal is primarily modulated by blood absorption whereas SPG signal is modulated effectively by RBC scattering. SPG has been shown to produce higher signal-to-noise ratios in low perfusion conditions [130] but the advantage of PPG is its significantly simpler design.

2.4.6 Photoacoustic Imaging

PAI, illustrated in Figure 12, is an optoacoustic imaging technique that uses a very short (nanosecond scale) pulsed laser to illuminate the skin. The molecules in the skin absorb the photons and the optical energy is converted into heat. The resulting temperature rise leads to thermoelastic expansion that generates pressure (ultrasound) waves. These waves are detected with an ultrasonic transducer or an array of ultrasonic transducers. [131; 132; 133; 37] The technique utilizes the low scattering of acoustic waves in tissue – 1,000 times less than for light – to obtain high spatial resolution at depths of up to centimeters [37; 131].

There are two main implementations of PAI, categorized according to the image formation method: photoacoustic (PA) tomography and PA microscopy (PAM). PA tomography uses an array of ultrasound transducers arranged in 2D (linear or curved) or 3D spatially to reconstruct the image, providing cross-sectional or volumetric images [134; 131]. In addition, more sophisticated computational methods can also be used in the image reconstruction phase, known as PA computation tomography (PACT) [37]. PA tomography has an imaging depth of several centimeters, but does not have sufficient resolution to image superficial vasculature [131]. PAM uses a focused ultrasound transducer for image reconstruction and can be configured in two settings depending on the targeted imaging depth and spatial resolution [37]. Acoustic resolution PAM (AR-PAM) uses weak optical and tight acoustic focusing [131] with a lateral resolution of tens of micrometers and an imaging depth of 1–10 mm [37]. Optical resolution PAM (OR-PAM) then again uses tight optical focusing [131], which enhances the lateral resolution to even sub-micrometer but with a cost of decreased imaging depth of less than 1 mm [37]. Thus, the choice of PAI implementation is depended on the targeted vascular compartment, with OP-PAM being the most suitable for superficial vascular imaging.

PAI has been extensively used in human skin imaging, especially in skin cancer and skin disease, such as psoriasis, research [133; 135]. In addition to visualizing the cutaneous vasculature, PAI is able to provide functional and molecular biomarkers by quantifying vascular density and blood flow velocity. In addition, spectroscopic PAI can extract melanin concentration and oxygen saturation of hemoglobin. The total hemoglobin concentration can also be calculated using a wavelength corresponding to an isosbestic point in the oxy- and deoxyhemoglobin spectra. [37]

2.4.7 Optical Coherence Tomography

Optical coherence tomography (OCT) is an imaging technique that uses interferometry, detailed in Figure 13, to obtain high-resolution cross-sectional images of the internal microstructure of samples. An interferometer measures the cross-correlation between reflected light from a sample and a reference. In a typical Michaelson interferometer-based setup low-coherence light is directed onto a beam-splitter with one beam directed onto a sample and another onto a reference. [136; 137; 138]. The back-scattered light from the sample is interfered with the reference light and is detected by a photodetector at the output of the intereferometer [136; 137]. In a time-domain system, the reference mirror is moved with respect to the beam splitter to measure optical delay, effectively measuring backscattered light from one depth in the sample at a time. Higher scan rates (hundreds of images per second vs. a few images per second) can be obtained with frequency-domain and spectral-domain techniques, where Fourier transformation is used to compute the sample reflectance profile. In these techniques, depth information is effectively collected from all depths in parallel. [138]

OCT is commonly compared to ultrasound due to its somewhat similar spatial resolution [138]. OCT axial resolution is in the micrometer range, whereas a high-frequency ultrasound (50 MHz transducer) has a resolution smaller than 100 µm. In terms of probing depth comparison, OCT achieves a probing depth of 1–3 mm when the light source is in the range 1,300 nm, while ultrasound achieves approximately 1.4 mm. [139; 136]. Lower-frequency ultrasound can achieve penetration depths on the order of centimeters, though with a significant decrease in resolution [136]. In skin morphology analysis, OCT is able to reveal finer details and provide higher precision to determine geometric dimensions [139]. Besides skin, OCT is especially widely used for retinal imaging and to guide coronary stenting and in research on coronary artery disease and acute myocardial infarction [138].

2.4.8 Videocapillaroscopy

Videocapillaroscopy, illustrated in Figure 14, is a reflected light microscopy technique in which the capillaries of the skin are directly observed with a handheld device consisting of a magnifying lens system (typically in the order of 200) and a video camera. The technique allows to observe only capillaries with circulating RBCs as the vessels walls are invisible. [140; 141]

Typically, the technique is used to study the nailfold capillaries which are easily observable considering that they are parallel to the surface of the skin. This allows

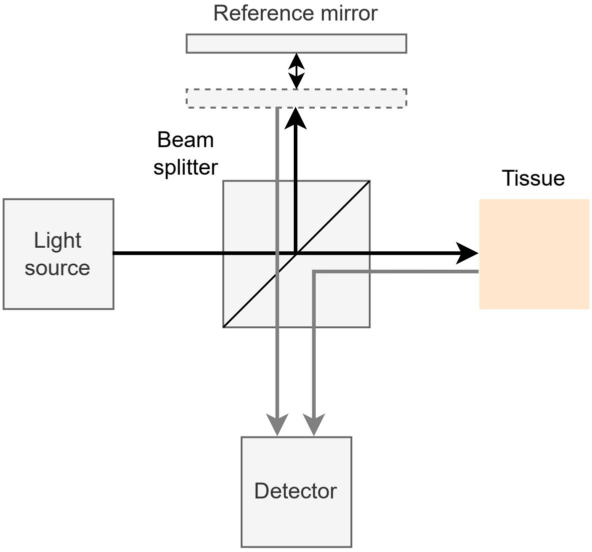

Figure 13. Schematic of interferometry, which is the underlying technique used in optical coherence tomography (OCT) [137].

morphological study of capillaries, for example, enlarged capillary loops, giant capillaries, and in general capillary dimensions. [140; 141] In other parts of the skin, the technique can only provide the density of functioning capillaries as the capillaries are perpendicular to the skin and show up as red spots [140]. Videocapillaroscopy is the gold standard for screening for systemic sclerosis and Raynaud's phenomenon [141].

2.4.9 Orthogonal Polarization Spectral Imaging

OPS technique, visualized in Figure 14, uses linearly polarized light and a polarizing beam splitter together with a lens to illuminate a circular area of skin of approximately 1 mm in diameter. The reflected and backscattered light from the tissue travels through the beam splitter and an orthogonal polarizer behind it into a video camera. The polarizer ensures that most of the reflected (polarized) light cannot pass through, whereas light that has gone through multiple scattering events within the tissue can pass because it is depolarized. Absorbing material, such as blood vessels with light absorbing RBCs, in the foreground is effectively back-illuminated by the observed light. [143; 145]

Videos recorded with OPS can be analyzed for functional capillary density, RBC velocity and small blood vessel diameter [143; 146]. At the time of its invention, OPS offered a significant improvement over nailfold videocapillaroscopy because it enabled the evaluation of any microcirculatory bed [147]. It has also been regarded

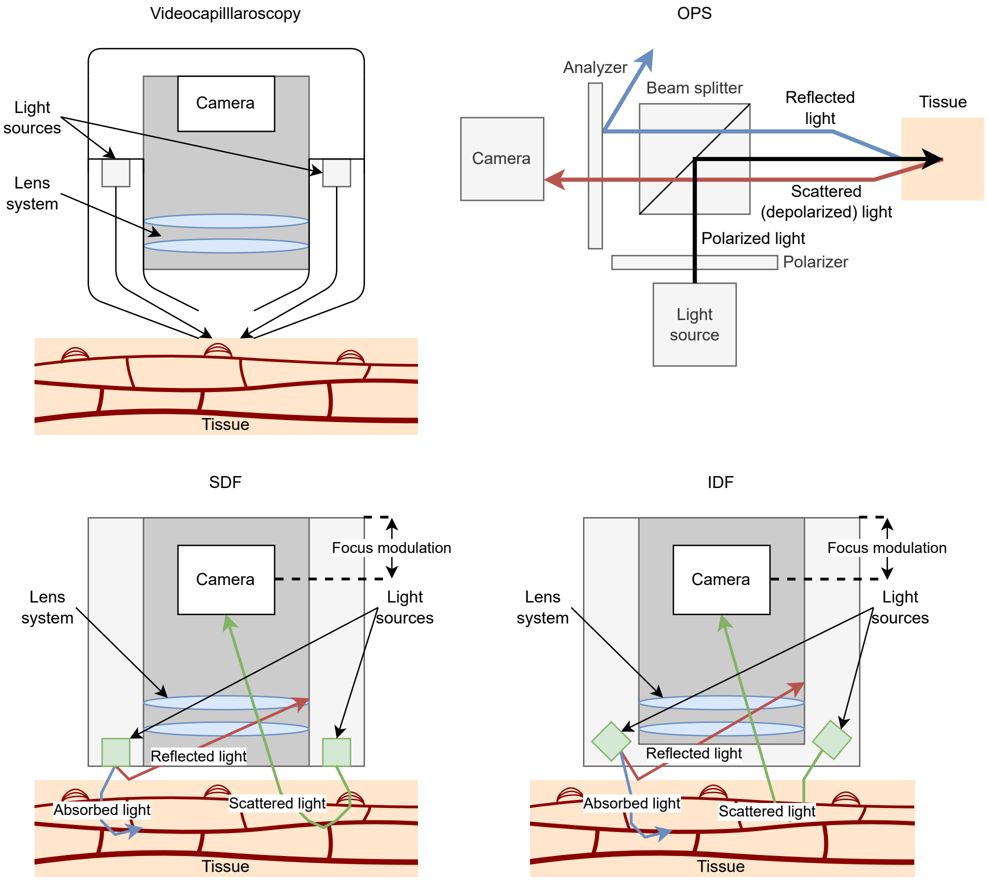

Figure 14. Microscopic techniques, from top left to bottom right. i) Videocapillaroscopy [142]. ii) Orthogonal polarization spectral imaging (OPS) [143]. iii) Sidestream dark field imaging (SDF) [144]. iv) Incident dark field illumination (IDF) [144].

as a bedside imaging technique that has resulted in general recognition of the importance of monitoring microcirculation in critically ill patients [148].

2.4.10 Sidestream Dark Field Imaging

In SDF, illustrated in Figure 14, tissue is illuminated by a ring of LEDs placed concentrically and outside a light guide leading to a video camera. The light guide blocks the direct reflectance of light from the tissue surface into the lens system inside the light guide. Thus, the light guide is optically insulated from the illuminating LEDs. The photons entering the light guide are the result of light scattering within the illuminated tissue, and as in OPS, absorbing material, such as RBCs, appears dark against a white/grayish background. Furthermore, the illuminating LEDs are pulsed in synchrony with the camera frame rate to improve the image quality of the moving

RBCs. The central wavelength of the LEDs is selected according to the isosbestic point in the absorption spectra of oxygenated and deoxygenated hemoglobin, at 530 nm, to ensure light absorption independent of the oxygenation state of the RBCs. [149]

SDF is regarded as the second generation of hand-held microscopes [147]. Compared to the first generation, OPS, it produces clearer images of the superficial microcirculatory network due to stroboscopic illumination that prevents smearing of RBC and reduces image blurring due to movement of the probe/tissue [149; 147]. Additionally, the focusing depth of SDF is shallower than in OPS, reducing the interference of lower vascular structures [149]. SDF is able to measure all the same parameters as OPS.

2.4.11 Incident Dark-Field Illumination

Unlike in SDF where the LEDs illuminate the tissue perpendicularly, in IDF, illustrated in Figure 14, the LEDs are positioned in an angle to utilize the principles of dark-field illumination [150]. This ensures that only scattered light from the sample is collected [151]. The measurement system is otherwise rather similar to SDF, i.e., a light guide with a lens system is in the middle of a conical object, guiding the light to a camera, and the LEDs are pulsed only for a very short time of 2 ms in synchronization with the video camera [147].

IDF is considered as the third generation of hand-held microscopes [147]. The commercial implementation of the technique, CytoCam (Braedius Medical, The Netherlands), has provided improved optical resolution and almost three times larger effective field of view compared to SDF based devices. However, this is at least to some extent due to technical improvements, for example, the commercial implementations of SDF used analogue video cameras whereas CytoCam is based on a digital video camera [144].

2.5 Summary of Optical Sensing Techniques

The presented techniques can be loosely grouped into PPG-based (PPG, MWPPG, and rPPG), spectroscopy-based (NIRS, DCS, and HSI), laser-based (LDF, LSCI, and PAI, although DCS also uses a laser), intereferometry-based (OCT), and microscopy-based (videocapillaroscopy, OPS, SDF, and IDF). However, the techniques can also be grouped based on which dominates more, absorption or scattering. The PPG-based techniques are clearly based on absorption as the waveform is the result of varying blood volume modulating, by absorption, the amount of backscattered light. NIRS is similarly based on absorption as it takes advantage of the lower absorption of hemoglobin in the NIR range and, moreover, the technique of measuring oxygen saturation is based on the oxy- and deoxyhemoglobin absorption spectra. Similar argumentation can be used for HSI. PAI is also clearly in the same group, as acoustic waves are the result of thermal expansion due to absorption. LDF then again is clearly based on scattering, since it detects the light scattered by moving RBCs, as are DCS and LSCI where the fluctuation of the speckle pattern is caused by moving particles scattering coherent light. The interferometery forming the basis in OCT is essentially based on registering scattered light from a sample. In human skin light scattering dominates over absorption (see also Section 2.2.1), and thus the contrast of light absorbing structures, such as microvessels, is low [152]. Therefore, video-capillaroscopy is also more affected by scattering. Finally, OPS, SDF, and IDF all had different technical ways to ensure that only backscattered light is collected, so they also fall under scattering.

Table 1 provides a summary of the optical techniques presented. In terms of simplicity, PPG and MWPPG stand out from the rest, requiring only simple semiconductor components without complex optics or the risks of, for example, laser light. The drawbacks are that they can only provide 1D signals with rather poor spatial and depth resolution compared to some of the imaging techniques. However, technical simplicity, low cost, and a potentially rich set of parameters make MWPPG a suitable candidate for use outside of clinical practice, i.e. in modern wearables.

Table 1. Comparison of the presented optical techniques used to study cutaneous vasculature.

Technique and principle	Wavelength	Penetration depth	Parameters	Refs.
PPG – Measures blood volume variations with a semi-narrow-band LED and a photodiode	Typically green for single wavelength and red & IR for dual wavelength	Depends on the wavelength and light source - detector distance, from $<$ 1 mm (blue light) to a few centimeters (IR with large source-detector distance)	HR, HRV, SpO_2, BP-related PTT (in dual-sensor configuration), respiratory rate, arterial stiffness, jugular venous pulse, and cardiac arrhythmia	[1; 153; 76; 79; 77; 154]
MWPPG – Same operating principle as in PPG but uses several different wavelengths of light simultaneously	Typically ranges from blue light to NIR	Same as in the case of PPG but probes different depths simultaneously	All the same as for PPG but additionally microvascular PTT and potentially blood glucose	[20; 21; 85; 155; 86]

Continued on next page

Technique and principle	Wavelength	Penetration depth	Parameters	Refs.
rPPG – Same operating principle as in PPG but uses a video camera and either ambient or broadband light source to acquire signals from a distance of up to several meters	Ambient light / broadband light source, in essence uses the three channels of an RGB camera, or alternatively a NIR camera	Depends on the camera channel, however less than in contact PPG	HR, HRV, oxygen saturation, PTT, and respiratory rate	[96; 93]
NIRS – Uses NIR radiation and large source-detector distance to measure oxygen saturation from deep tissue	∼700–2,500 nm	Centimeters, even up to 8 cm, depending on the tissue and source-detector distance	Cerebral perfusion and oxygenation, peripheral tissue and muscle oxygenation	[108; 109; 112; 110]
DCS – Measures blood flow in deep tissues by analyzing fluctuations in scattered coherent light caused by moving RBCs	∼785 nm	Centimeters, less than that of NIRS	Cerebral and tissue blood flow	[116; 113; 117; 114; 156; 115]
Hyperspectral imaging – Captures 2D images with spectral information in each pixel	Varies from visible light to NIR	Depends on the wavelength and light source, from < 1 mm to several millimeters and even deeper	Tissue perfusion, tissue oxygenation	[119; 120; 118]
LDF – Laser illuminates skin while a detector records the Doppler frequency shift caused by moving RBCs scattering the light	630–830 nm	1–1.5 mm	RBC flux (product of RBC concentration and average velocity)	[122; 123; 128; 157]
LSCI – Observes changes in speckle pattern caused by moving RBCs	Typically between 600 and 900 nm	Depends on the wavelength of the laser diode, for example for red, $<$ 1 mm	Blood flow, RBC velocity; SPG can provide many of the same parameters as PPG	[127; 125; 158]

Continued on next page

Technique and principle	Wavelength	Penetration depth	Parameters	Refs.
OCT – Uses interferometry to obtain high-resolution cross-sectional images	∼ 1,300 nm	1–3 mm	Detailed cross-sectional images of vasculature	[136; 138; 137; 133]
PAI – Short pulse of a laser is fired at tissue and partially absorbed by molecules, the resulting heat induces a pressure rise propagating as an acoustic wave that is detected with an ultrasonic transducer	500–650 nm (for studying the cutaneous vasculature)	OR-PAM: < 1 mm; AR-PAM: 1–10 mm; PACT: several centimeters	High resolution images of the cutaneous vasculature, vascular density, blood flow velocity, melanin concentration, oxygen saturation and total hemoglobin concentration	[37; 131; 133; 132; 135]
Videocapillaroscopy – Microscope with bright LED illumination and a video camera	White LEDs	∼200 µm	Nailfold capillary morphology (shape), capillary dimensions, and functional capillary density	[140; 159; 141; 160]
OPS – Uses an optical system to pass only light that has experienced multiple scattering within the tissue	Light source centered around 548 nm	Typical depth of focus is ∼0.2 mm, at maximum 1 mm	Functional capillary density, RBC velocity, and small blood vessel diameter (down to 10 µm)	[143; 145]
SDF – Uses pulsed light synchronized with a video camera to record scattered light from the tissue	LEDs with a central wavelength of 530 nm	Focusing depth is shallower than in OPS.	Functional capillary density, capillary diameter, and RBC velocity	[149; 161]
IDF – Uses dark field illumination to guarantee that only scattered light from the tissue is recorded with a video camera	LEDs with a central wavelength of 530 nm	< 1 mm	Total vessel density, microvascular flow index (RBC velocity related), proportion of perfused vessels, and perfused vessel density	[148; 162; 163]

2.6 Techniques to Obtain Hemodynamic Responses from the Cutaneous Vasculature

Several techniques can be used to stimulate the cutaneous vasculature to study hemodynamic responses. Such techniques are also known as reactivity tests as they allow assessment of microvascular reactivity when the microvessels are challenged. Common techniques are summarized in Table 2 with brief descriptions below.

Thermal Stimulus

Thermal stimulus includes local heating and local cooling. In local heating, also known as local thermal hyperemia, the skin is heated to approximately 42–44 °C for at least 30 minutes. Rapid initial increase in skin blood flow is observed within 10 minutes of start and a plateau after 20–30 minutes of heating [164]. If heating continues for more than 45–50 minutes, skin blood flow reverses towards baseline [140]. In contrast, local cooling causes an initial rapid decrease in skin blood flow due to vasoconstriction, followed by transient vasodilation, and prolonged vasoconstriction [164]. The best reproducibility has been obtained by cooling to 15 °C for 30 minutes [165].

Another cooling challenge is the so-called cold-pressor test in which a limb, such as a hand or a foot, is immersed in cold water while simultaneously measuring biosignals from, e.g., the other hand that is not immersed in water. The effects of immersion in water can be observed in signals due to systemic sympathetic activation [140].

Electrical Stimulus

Electrical stimulus is the application of a small non-noxious electrical current (e.g. 100 µA as in [166]) to the skin. This causes current-induced vasodilation (CIV) that increases the local skin blood flow. [124] The response to electrical current has been shown to vary depending on the duration and timing of the current application. For example, two 1 minute periods of current application result in a greater response than a single 2 minute period. [166] Interestingly, it has also been shown that an intake of acetylsalicyclic acid (aspirin) blocks CIV [167].

Pharmacological Stimulus

Iontophoresis of acetylcholine and sodium nitroprusside is widely used non-invasive technique to study endothelium-dependent and endothelium-independent, respectively, vasodilation. Iontophoresis is the process of delivering drugs into the skin using a low-intensity electrical current to carry charged molecules. This allows for a

Table 2. A summary of techniques that are used to obtain hemodynamic responses from the cutaneous vasculature.

Stimulus	Technique	Description	Refs.
Thermal	Local thermal hyperemia	Local heating of the skin causes a biphasic increase in skin blood flow	[124; 158]
	Local cooling	Local cooling of the skin causes initial rapid vasoconstriction which is followed by vasodilation and finally prolonged vasoconstriction	[124; 158]
	Cold pressor test	Immersion of a body part (typically hand) into cold water causes pronounced peripheral vasoconstriction	[168]
Electrical	Current-induced vasodilation	Harmlessly small electrical current increases skin blood flow	[124; 158]
Pharmacological	Anodal iontophoresis of acetylcholine	Low electrical current is applied to the skin to push molecules of acetylcholine into the skin, causing endothelium-dependent vasodilation	[124; 158]
	Cathodal iontophoresis of sodium nitroprusside	Low electrical current is applied to the skin to push molecules of sodium nitroprusside into the skin, causing endothelium-independent vasodilation	[124; 158]
	Microdialysis	Drug infusion using semi-permeable membranes inserted into the dermis	[124]
Mechanical	Reactive hyperemia	Arterial occlusion of a limb causes increased blood flow after releasing the occlusion	[124; 158]
	Pressure-induced vasodilation	Non-nociceptive pressure application induces sustained vasodilation in healthy skin to protect tissue from ischemic damage.	[124; 158]
	Pressure sweep (oscillometry)	Steadily increasing/decreasing pressure alters the loading of the blood vessel walls	[169; 86]

rather fast and accurate control of the drug, but the technique suffers from simultaneous effects of CIV that can cause confusion. [124; 158] Microdialysis overcomes this with the insertion of small fibers with semi-permeable membrances into the dermis. This allows accurate control of the drug infusion rate, but on the downside the operation is invasive and can cause pain. [124]

Mechanical Stimulus

Mechanical stimulus includes techniques that use compression to stimulate the cutaneous microvascular vessels. A well-known technique of this type is the occlusion of arterial supply to a limb, typically the arm, for a brief period of time. The magnitude of reperfusion after the ischemic event is known as the reactive hyperemia index. There are several reactive hyperemia (RH) techniques, one widely used being peripheral arterial tonometry where finger pressure pulsations are recorded. For a healthy individual, the post-occlusion pulsations have noticeably larger amplitudes, while the lack of them implies an abnormal response. [170]

The application of non-nociceptive (i.e., non-painful) pressure to the skin of a healthy person causes pressure-induced vasodilation (PIV) to protect tissues from ischemic damage. PIV occurs when the external pressure is below 150 mmHg [171] and is known to be impaired in elderly and diabetic patients. [124; 158]

Finally, a steadily increasing/decreasing external pressure, also known as pressure sweep, is the predominant technique used in non-invasive BP monitors. As the level of external pressure nears the mean arterial pressure (MAP), the amplitudes of the pressure pulse waveforms (also known as oscillations, thus the name *oscillometry*) increase, reaching maximum at a pressure level equal to the MAP. At pressure levels above MAP the amplitudes start to decrease. By plotting the amplitudes as a function of time, a bell-shaped curve is obtained, the maximum point corresponding to the mean BP of the large arteries. The systolic blood pressure (SBP) and diastolic blood pressure (DBP) are then extracted from the curve using more or less proprietary algorithms. [172; 173] In a typical BP measurement setup, the external pressure is applied with a cuff wrapped around the upper arm, but a recent study has shown that the distal phalanx of the finger is the second best site to measure BP from the arm [174]. In addition to a cuff, arterial tonometry and finger-pressing method can also be used to measure BP [175]. Interestingly, the oscillometric waveform envelope can also be extracted from a PPG signal, with the extracted BP readings showing a strong correlation with brachial intra-arterial pressure readings [169].

3 Aims of the Study

The original publications had the following aims:

I Tonometric Multi-Wavelength Photoplethysmography for Studying the Cutaneous Microvasculature of the Fingertip
The aim in this study was to develop a method to extract depth-resolved hemodynamic information from the fingertip. For this purpose, a 5-channel MWPPG instrument with a mechanism to control and measure the amount of external pressure applied to the fingertip was developed. The instrument was demonstrated in two measurements where the external pressure was (i) ramped above the level of SBP and (ii) held approximately at the level of the MAP for two minutes. Furthermore, an MC model simulating the propagation of light within a layered tissue model representing that of a fingertip was developed to gain understanding of the experimental measurement set (i).

II Wearable Edge Machine Learning with Synthetic Photoplethysmograms
The rapid development of AI research puts a pressure on high-quality data to train accurate models, while at the same time general public has become more aware of the risks related to gathering big data. Simultaneously, AI models transform from cloud-centric computation to a more edge-based approach where models are executed directly on devices that gather the model inputs, i.e. sensor data. The aim of the study was to acknowledge these challenges by presenting a synthetic PPG model to generate a large amount of privacy-secure synthetic data and then training CNN models small enough to run on a developed wearable PPG device.

III Investigating the Impact of Contact Pressure on Photoplethysmograms
Sensor contact pressure can have a significant impact on MWPPG signals, with too low contact pressure leading to poor signal-to-noise ratio (SNR) and excessive motion artifacts while too high contact pressure can occlude the underlying blood vessels, leading to a loss of pulsatile signal. This study aimed to investigate the impact of contact pressure on PPG signals with the help of an experimental finger-cuff instrument. The signals were investigated from the point of view of: (i) SpO_2, (ii) PAT, and (iii) pulse waveform features.

IV Non-invasive Hemodynamic Monitoring System Integrating Spectrometry, Photoplethysmography and Arterial Pressure Measurement Capabilities

This study is a continuation of Publication I with the goal of markedly enhancing the optical resolution beyond the five channels to explore signal information content as a function of light wavelength during an oscillometric measurement. For this purpose, an instrument integrating a spectrometer, an LED printed circuit board (PCB), and a mechanism to regulate the external pressure applied to the fingertip was developed. The instrument effectively merges the functionalities of PPG, spectrometry, and arterial pressure measurement.

4 Materials and Methods

Each original publication was based on a separate study, and each study included a unique instrument. From now on, we will refer to these studies, including human studies, and the instruments used in them, with the same Roman numerals as for the original publications listed in the previous chapter 3. That is, as an example, the original Publication I included Instrument I used in Human Study I. The most relevant materials and methods related to the studies are presented below, with more details presented in the original publications.

4.1 Instrument Design

Custom PCBs included in Instruments I, III and IV, were designed in Autodesk Eagle and manufactured and assembled by PCBWay (China). All electronics were enclosed in plastic parts designed using Autodesk Inventor Professional CAD software. The same software was used to design all mechanical parts of the instruments. The parts were 3D printed with the Creality CR-20 Pro (China) 3D printer based on the fused filament fabrication technique.

4.2 Software

The firmware of Instrument I was programmed in C using the nRF5 software development kit (SDK) by Nordic Semiconductor (Norway). The rest of the instruments were likewise programmed in C but using the Espressif Internet-of-Things Development Framework (ESP-IDF). The reason for changing the framework from Nordic Semiconductor to Espressif (China) was that the latter was deemed more suitable for edge machine learning used in Instrument II. Good experience with the framework encouraged to use Espressif system on a chips (SoCs) also for Instruments III and IV.

A graphical user interface (GUI) was developed for Instruments I, III and IV to facilitate the convenient acquisition of signals. The GUIs were programmed using the cross-platform PyQt toolkit. Given that Instrument II is a wearable device that functions as a standalone device without the need for computer instructions, it was not necessary to develop a GUI program. Instead, the stored data were fetched from the flash memory using a simple Jupyter Notebook with a serial connection.

In study II, a mobile application was developed using the cross-platform Flutter SDK. The application connects to Instrument II via Bluetooth Low Energy to receive the heart rate values predicted by the embedded ML model.

All data analysis was performed with Python 3. The analysis codes relied heavily on the standard Python libraries for numerical analysis and scientific computation, namely NumPy and SciPy.

4.3 Signal Processing

PPG signals were filtered with zero-phase (filtfilt) Butterworth filters. Butterworth filter is well suited for biosignal analysis, as it does not include pass- and stop-band ripple unlike, for example, type I and II Chebyshev filters that are also used at times in PPG signal analysis [77]. The DC components were extracted with 0.2 Hz (Instrument I) or 0.5 Hz (Instruments III and IV) fourth-order low-pass filters. The AC components were extracted with band-pass filters with the lower cutoff frequency set to 0.5 Hz, while the upper cutoff frequency was 5 (Instrument II), 8 (Instruments I and IV) or 10 Hz (Instrument III). These cutoff frequencies ensure that the main frequency band of 0.5–5 Hz in a PPG signal is included [76]. The variation in the upper cutoff frequency was mostly due to application-specific matters. For example, in the wearable device (Instrument II) a lower cutoff frequency of 5 Hz was used to suppress artifacts due to movement. The order of the filter was two for the wearable device and four for the other instruments. The wearable device had a lower order filter because the filter was also applied online in the device, and thus computation complexity was a factor in filter construction.

ECG signals were also filtered with a fourth-order Butterworth filter. The band-pass filter cutoff frequencies were set at 2 and 40 Hz for signals recorded with Instrument II and 0.5 and 40 Hz for those of Instrument III. These cutoff frequencies were deemed appropriate for heart rate measurement, given that the QRS complex of the ECG wave typically falls within the frequency range of 8–50 Hz [176].

PPG signal waveform feet and peaks were detected with the automatic multi-scale peak detection (AMPD) algorithm presented in [177] for the signals recorded with Instruments I, III and IV. Instrument II used a CNN model to detect waveform feet along with some well-known peak detectors (see Section 5.4.2). ECG R wave peaks were detected with the Pan-Tompkins algorithm [178].

4.4 Human Studies

Each study included an experimental section of human studies in which the instruments were used to record signals from volunteers. Table 3 summarizes the key information for each study, while the following subsections briefly go through the measurements behind each study set. All measurements were conducted accord-

Table 3. Summary of the performed human studies. The values in parenthesis in the *participants* column are the number of women participants. The values in the columns *age*, *ref. SBP*, *ref. MAP*, and *ref. DBP* are mean ± standard deviation (SD). The reference SBP and DBP readings were used to calculate MAP using the typical formula of: $MAP = 1/3 \cdot SBP + 2/3 \cdot DBP$ [179]. The Omron M3 reference device was attached to the left upper arm in each study set.

Study	Participants	Age [years]	Ref. device	Ref. SBP [mmHg]	Ref. MAP [mmHg]	Ref. DBP [mmHg]
Ia	10 (5)	45 ± 19	Omron M3	118 ± 13	88 ± 9	73 ± 8
Ib	19 (4)	58 ± 19	Omron M3	126 ± 14	91 ± 9	74 ± 8
II	20 (9)	34 ± 9	ECG	-	-	-
III	19 (7)	37 ± 13	Omron M3	119 ± 17	93 ± 11	80 ± 9
IV	10 (4)	40 ± 14	Omron M3	121 ± 9	92 ± 5	78 ± 4

ing to the Declaration of Helsinki guidelines. Furthermore, study I measurements were conducted with permission from the Ethics Committee of the Hospital District of Southwest Finland and National Supervisory Authority for Welfare and Health (project number 1574/31/2018), while studies II–IV were conducted with permission from the University of Turku Ethics committee. Informed consent was obtained from all participants in each study.

4.4.1 Studies Ia and Ib

The measurement set for study Ia consisted of oscillometric fingertip measurements. The external pressure squeezing the fingertip was gradually increased approximately 40–50 mmHg above the SBP. The measurements were performed in a supine position and three measurements were taken from each participant. The total number of successful measurements was 27 with three measurements omitted due to poor signal quality, caused by poor placement of the fingertip on the sensing system.

Another set of measurements, labeled from here on as study Ib, was collected to study the effects of static pressure hold on MWPPG signals. In these measurements, the level of external pressure was raised slightly below the MAP and held there for about two minutes. One measurement was taken from each participant.

4.4.2 Study II

The study consisted of three different measurements with the study participant: i) sitting in a chair, ii) walking, and iii) moving the hand with the experimental wearable device in random ways. Each measurement lasted 2 minutes and eight seconds with no movement within the first and last 20 seconds. The total number of successful measurements was 55 with three poor measurements (due to poor ECG signal quality) in ii) and two in iii).

4.4.3 Study III

This study investigated the impact of contact pressure (P_c) on fingertip MWPPG signals with measurements where the level of external pressure was increased by 10 mmHg every ten seconds until the level of external pressure was above SBP, typically 150 mmHg. Two measurements were taken from each participant while sitting with the left arm comfortably placed on a table. The total number of measurements was 38.

4.4.4 Study IV

This study set is similar to the study set Ia in that the measurements were also oscillometric in the sense that the level of external pressure was gradually increased above the level of SBP. One measurement was obtained from each participant.

5 Summary of Results and Discussion

5.1 Developed Instruments

This section presents each of the four instruments developed from the perspectives of hardware design and operating principle. A summary of the instruments is provided in Table 4 to facilitate comparison between them. The instruments differ mainly in terms of the optical sensing module, pressure sensing module, technique used to control the pressure between the optical sensing module and the finger, and whether or not an ECG module is present.

5.1.1 Instrument I

Hardware

Instrument I, pictured in Figure 15a, was developed around a custom MWPPG sensor PCB consisting of five Kingbright Electronic Co, Ltd. APT series LEDs emitting light at five different wavelengths: 465 nm (blue), 515 nm (green), 590 nm (yellow), 640 nm (red), and 880 nm (infrared). To accommodate the wide spectral bandwidth of the LEDs, the VEMD1060X01 photodiode was selected due to its rather wide spectral bandwidth of 350–1,070 nm (peaking at 820 nm). An additional factor was the relatively small surface-mount device package of 0805 which made it possible to create a small circular PCB with a diamater of just 9.6 mm.

The MWPPG sensor PCB was connected to another custom PCB containing the driving circuits for the LEDs and a circuit to read the photodiode output through a small connector (BM08B-SURS-TF(LF)(SN) by JST Sales America Inc.) at the bottom of the PCB. The constant current LED drivers were constructed from NPN bipolar junction transistors working in emitter follower configuration. Current control was achieved by feeding the bases of the transistors with 12-bit digital-to-analog converters (DACs) (MCP4728 by Microchip). The constant current configuration guaranteed stable light output characteristics. The small photodiode current was converted into voltage using a transimpedance amplifier circuit and routed to a 16-bit successive approximation analog-to-digital converter (ADC) (AD7680 by Analog Devices). All components were powered by two ultralow-noise, low-dropout 4.7 V and 3.3 V linear regulators, of which the former powered the LEDs and the latter all the other components.

Table 4. Summary of the developed instruments.

Instrument	Optical sensing module	Pressure sensing module	ECG module	Optical sensing module pressure control technique	Operating principle
I	5-channel custom MWPPG sensor, 465 (blue), 515 (green), 590 (yellow), 640 (red), and 880 (IR) nm	Barometric pressure sensor BMP280 cast in epoxy and encapsulated inside an air cushion	-	Pressing mechanism controlled by a stepper motor (28BYJ-48) (tonometry)	Fingertip is pressed in a controlled manner against the optical sensing unit mounted on top of the pressure sensing unit
II	MAX30101 PPG sensor: 537 (green), 660 (red), and 880 (IR) nm	-	AD8232 (single channel)	The optical sensing module is attached to a finger with a Velcro strap (no pressure control)	Wearable device measuring optical signals from the proximal phalanx of a finger while simultaneously measuring ECG
III	MAX30101 PPG sensor: 537 (green), 660 (red), and 880 (IR) nm	Absolute pressure sensor MPRLS0025-PA00001A measuring the pressure of a small finger cuff	AD8232 (single channel)	Small finger cuff wrapped around the optical sensing module and a fingertip	Contact pressure between the PPG sensor and a fingertip is varied with a pressure cuff wrapped around the fingertip while simultaneously also measuring ECG signal
IV	FLAME-T-VIS-NIR-ES spectrometer, utilized wavelength range: 433.5–730.5 nm (99 PPG channels with approximately 3 nm wide wavelength binning)	Load cell FX292X-100A-0010-L mounted in the pressing mechanism to sense the force applied to a fingertip	-	Pressing mechanism controlled by a stepper motor (28BYJ-48) (tonometry)	Fingertip is pressed in a controlled manner against the optical sensing unit while recording the applied force

The instrument also included a compression generation and measurement system similar to the one in [180]. A stepper motor (28BYJ-48, generic brand), driven by transistors in the Darlington configuration, rotated a threaded shaft attached to a plastic bar guided by two metal rods at each end, effectively transforming rotational

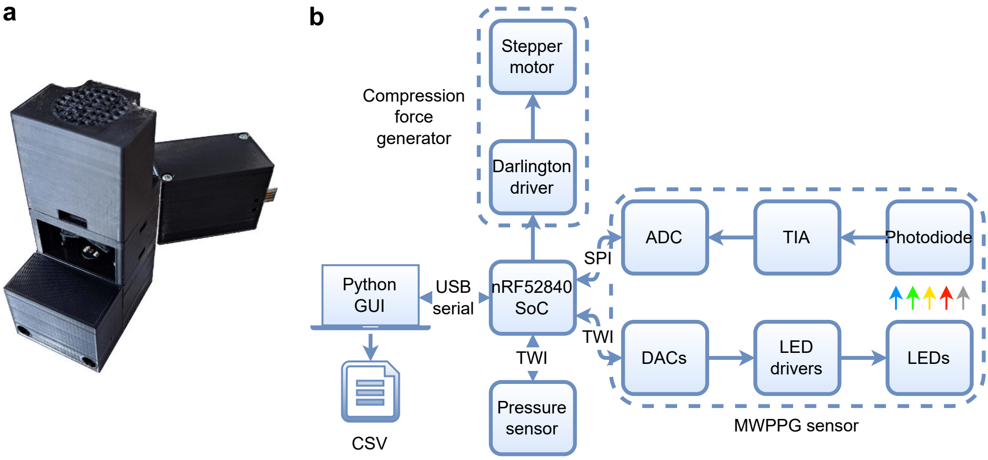

Figure 15. Instrument I. a. Picture of the instrument. The box behind the instrument contains the bulk of the electronics. b. System block diagram of the instrument. The figure is adapted from [86].

movement into vertical movement of the bar. Pressure sensing setup was modified from [180] in that a newer version of the barometric pressure sensor (BMP280 by Bosch Sensortec) was used and the sensor was not modified in any way. A PCB containing the sensor was cast in epoxy so that the top of the metal enclosure protecting the sensor was at the level of the epoxy. Once the epoxy was dry, an air cushion was sealed around the sensor element with a strong double-sided adhesive tape. The air cushion was basically a bubble cut from a piece of a strong but thin bubble wrap with the bottom part cut to facilitate air movement into the pressure sensor. The assembled component was then mounted at the bottom of a plastic part with a hole so that the air cushion was surrounded by rigid walls. The MWPPG PCB was mounted on top of a circular piston-shaped object, which was placed on top of the air cushion.

The device was controlled by nRF52840 Dongle (by Nordic Semiconductor, Norway) soldered to the driver PCB. The dongle contains the nRF52840 SoC that includes a 32-bit ARM Cortex-M4 processor running at 64 MHz together with the required digital peripherals such as the serial peripheral interface and the two-wire interface. The microcontroller was programmed so that the LEDs were time-multiplexed, meaning that each of the LEDs were sequentially lighten up while simultaneously reading the photodiode. The sampling frequency was 500 Hz for each MWPPG channel and 100 Hz for the pressure channel. The system block diagram of Instrument I is presented in Figure 15b.

Operating Principle

The device has a compact tabletop form factor specifically designed for fingertip measurements. The measurement starts by placing a fingertip with a piece of double-

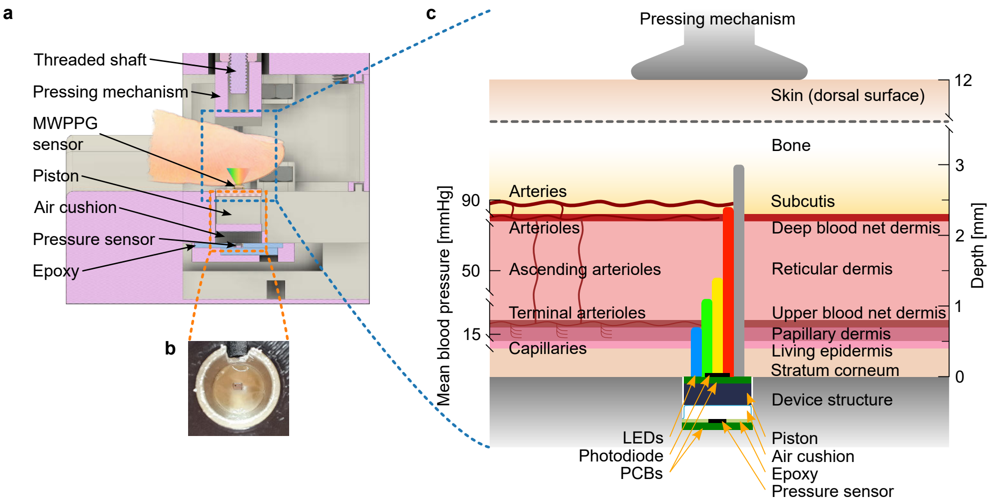

Figure 16. Instrument I concept. a. A cross-sectional view of the instrument with the main parts labeled. A threaded shaft rotated by a stepper motor presses the fingertip against a piston made of a stacked structure consisting of an MWPPG sensor, rigid piston structure, air cushion and a barometric pressure sensor. b. A close-up picture of the piston hole with the epoxy-casted pressure sensor at the bottom, seen through the transparent air cushion. c. Cross-sectional view of a simplified tissue model representing a typical fingertip. The vertical coloured bars, from blue to gray, present the mean penetration depth of each MWPPG channel, from blue to IR, computed with the developed MC simulation model. The figure is adapted from [86].

sided tape on its dorsal side inside the measurement chamber, as illustrated in Figure 16a. The placement of the palmar side is then adjusted to optimize signal quality. In the ideal case, the top of the piston is aligned with the distal transverse palmar arch, ensuring good coupling between the blood vessels and the piston and therefore the pressure sensor below, as shown in Figure 16b. A recent study investigated the feasibility of fingertip BP measurement and found that the fingertip was the second best measurement site in the arm after the upper arm, primarily due to the similar bone-to-tissue volume ratio of the fingertip relative to the upper arm [174].

After finding the optimal position, the fingertip is carefully raised to make contact with the pressing mechanism above, allowing the tape on the dorsal side to adhere securely. The double-sided tape serves to minimize unintentional or subconscious pressing of the piston, which can make it difficult to measure low-pressure readings. Once secured, the pressing mechanism is lowered, causing the fingertip to squeeze against the piston, compressing the underlying air cushion. The resulting pressure signal reflects the combined effect of the external compression force and the pulsating blood vessels exerting on the piston. [86]

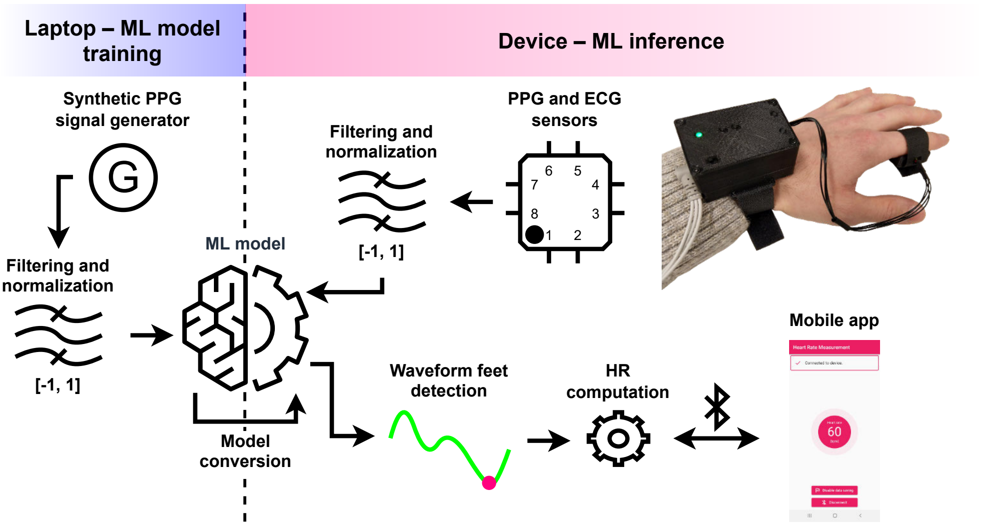

Figure 17. Instrument II concept. The developed wearable device is presented at the top right corner. The pipeline from sensor sampling to HR calculation and ultimately to sending the data to a mobile application over Bluetooth Low Energy is presented under the title *device*. Generation of synthetic signals and CNN model training are illustrated under the title *laptop*. The figure is from [181].

5.1.2 Instrument II

Hardware

The key design consideration in Instrument II was to be able to run ML models on the device, i.e. at the edge. The decision was ultimately made between the SoCs from Nordic Semiconductor and Espressif Systems. Ultimately, the ESP32-S3 SoC from Espessif Systems was selected as it had good documentation and SDK with regards to edge ML, but moreover a lot of processing power given that it has a dual-core 240 MHz processor. Coupled with 8 MB of external pseudostatic random access memory (RAM) (in addition to 512 KB of internal static RAM) and 16 MB of flash storage, the system is well-suited for edge ML.

A commercial three-channel (537, 660, and 880 nm) MWPPG sensor MAX30101 (by Maxim Integrated, United States) was selected for optical measurements. The sensor incorporates all the circuitry required to drive LEDs and digitize a photodiode signal. Regarding ECG, AD8232 (by Analog Devices, United States) was selected. The analog voltage produced by the integrated circuit was converted to digital readings using a 16 bit ADC (ADS1115 by Texas Instruments, United States). The components are powered by a rechargeable battery pack (950 mAh 3.7 V lithium polymer) to allow measurements on the move.

Operating Principle

The instrument is a wearable device consisting of two parts: i) a finger-worn small plastic part with the optical sensor, and ii) a casing holding the rest of the electronics. The finger-worn sensor is attached to the proximal phalanx of the digital finger on the left hand with a Velcro strap. The larger part with the electronics is attached to the wrist with another separate Velcro strap. The sensor unit is connected to the main unit with wires. A single-lead ECG cable with three electrodes (right arm, left arm, and left leg as the driven electrode) is connected to the main unit.

The main unit has a slide switch to start the device and a button to start a measurement. Once a measurement is started, the system starts to record all of the three PPG channels at a sampling rate of 100 Hz. However, only the green channel was used in the final analysis, given its robustness against motion artifacts [182]. Every four seconds, a CNN model stored on the flash is inferred using the 400 samples buffered from the previous four-second period. The detected waveform feet are used to calculate the HR and the value is sent over Bluetooth Low Energy to a connected mobile application. The concept of Instrument II is illustrated in Figure 17.

5.1.3 Instrument III

Hardware

Instrument III, pictured in Figure 18a, uses many of the same components as Instrument II. The SoC and the PPG and ECG sensors are the same, i.e., ESP32-S3, MAX30101, and AD8232, respectively. However, Instrument III also integrates a pressure generation and measurement system to measure PPG sensor contact pressure. For this purpose, the instrument includes an air pump (PUMP-924B by Transtek Medical, China), a motor driver (TB6612FNG by Toshiba Corporation, Japan) to control the 3 V DC motor of the pump, an absolute pressure sensor (MPRLS0025PA00001A by Honeywell, USA), and a solenoid valve (JQF1-3A, generic brand). The PPG sensor is on its own small circular PCB and is connected with wires to the main unit housing all the other components.

PPG sensor contact pressure control is performed with a small finger cuff wrapped around the sensor. The cuff was made by cutting a piece from a wrist cuff and then sealing it with a heat sealer. A flexible Velcro band with an adhesive surface was attached on the outer side of the cuff for fastening purposes. The cuff, pump, pressure sensor, and solenoid valve are all connected with silicone tubing. Initial testing of the instrument revealed that the pump flow rate was slightly too high for the small finger cuff. To address this issue, the air volume of the system was increased by incorporating a 100 ml syringe, effectively reducing the cuff fill rate, given a constant pump flow rate. The system block diagram of Instrument III is presented in Figure 18b.

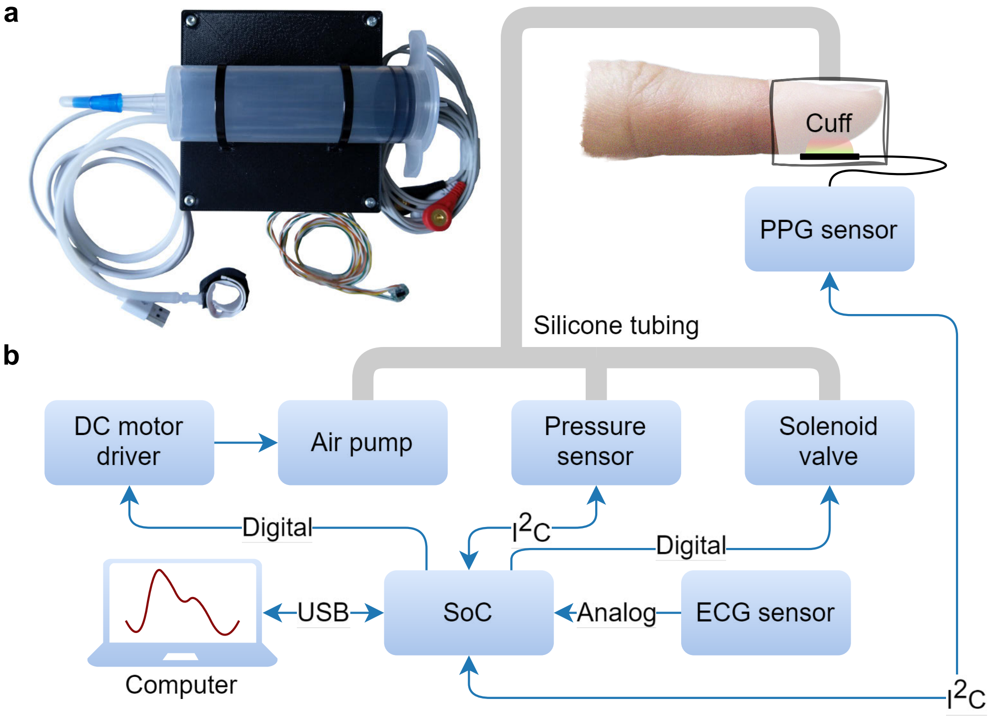

Figure 18. Instrument III. a. Picture of the instrument. b. System block diagram of the instrument. The figure is adapted from [183].

Operating Principle

The small PPG sensor PCB is placed on the palmar side of the fingertip and the cuff is wrapped around the fingertip and the sensor. The single-lead ECG cable is attached to the main unit that is connected to a laptop using a USB cable. With a press of a button from a custom GUI program, the instrument starts a measurement where the cuff pressure is increased in 10 mmHg steps every ten seconds until the suprasystolic pressure level (typically 150 mmHg) is reached. All signals are sampled at 100 Hz, including all three PPG channels – green (537 nm), red (660 nm) and IR (880 nm).

5.1.4 Instrument IV

Hardware

Instrument IV, shown in Figures 19a and 19b, is a direct continuation of Instrument I with the aim of increasing spectral resolution. The LED-based approach used in Instrument I is not suitable for increasing the number of channels for two reasons: i) even the smallest surface-mount device LEDs (0201 package) with PCB traces will quickly fill the small 9.6 mm in diameter PCB, and ii) a typical LED spectrum is relatively wide (e.g. the blue LED APT1608VBC/D used in Instrument I has a spectral bandwidth of 22 nm), meaning that the different channels would likely contain a significant portion of overlapping information. Therefore, the only way to achieve a channel count in the high tens or even hundreds is to use a spectrometer.

At the heart of Instrument IV is the FLAME-T-VIS-NIR-ES spectrometer (Ocean Insight, USA), a miniature spectrometer operating in the ultraviolet to NIR range of the electromagnetic spectrum. The spectrometer features a detector with 3,648 pixels and covers wavelengths approximately between 345 and 1,041 nm. Equipped with a 25 µm slit, it achieves an optical resolution of approximately 0.8 nm, and its ADC has a resolution of 16 bits.

The single fiber leg of a reflector/backscatter probe (QR400-7-VIS-BX by Ocean Insight, USA) was connected to the spectrometer, while the six-fiber leg intended for a light source was left unused. A tungsten halogen light source (HL-2000-HP by Ocean Insight, USA), with a spectral range of 360–2,400 nm, was tested, but failed to produce a sufficient PPG signal. This limitation is likely due to the very small fiber core size of only 400 µm, since the distance between the light source and the detector significantly affects the probing depth [184].

To address the challenges with the probe light source, a custom LED PCB was developed as an external light source. The LEDs included in the design were: a violet LED (APTR3216-VFX by Kingbright, Taiwan), a multi-color LED combining blue and green emitters (APHBM2012LVBDZGKC by Kingbright, Taiwan), and a broad spectrum white LED (S1S0-3030509503-0000003S-0P001 by Seoul Semiconductor Inc., South Korea). An IR LED (APT1608SF4C-PRV by Kingbright, Taiwan) was also assembled but delivered insufficient SNR for practical use.

The LEDs were powered and controlled by a constant-current LED driver (TLC59711 by Texas Instruments, USA). The PCB featured a small aperture in its center, allowing light to pass through to the spectrometer probe located beneath it, as illustrated in Figure 19c. Based on the wavelengths emitted by the LEDs, the operational wavelength range of the spectrometer was effectively limited to approximately 433.5–730.5 nm. To enhance signal quality, a 3 nm wide binning was applied during post-measurement analysis, resulting in a total of 99 PPG channels.

External pressure was generated using a stepper motor (28BYJ-48, generic brand) in a similar way to Instrument I, however, the pressure sensing part was different. Although the pressure transducer of Instrument I was able to detect faint pulsations of the fingertip arteries, the air cushion required more or less regular changing as the cushion lost its elastic properties as the number of measurements grew. Therefore, an alternative technique based on a compression load cell was developed as a successor. A high-quality load cell FS2030-000X-0500-G (TE Connectivity, USA) replaced the air cushion below the piston with simply the piston resting above the load cell pin. Then a calibration measurement was performed, in which weights were stacked above the load cell to convert the recorded ADC counts

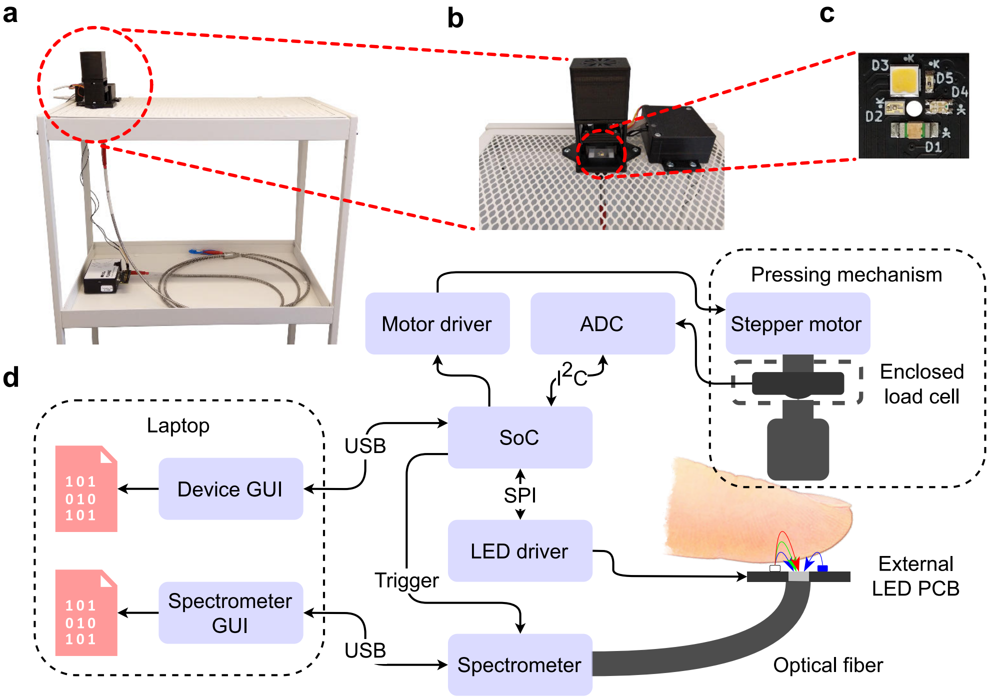

Figure 19. Instrument IV. a. Picture of the device. b. A close-up picture of the device, viewed from the front. c. A close-up picture of the LED PCB. d. System block diagram of the instrument. The figure is from [87].

to mmHg.

The load cell–based approach was considered accurate and reliable, and with the spectrometer-based approach it quickly became the only option. This was due to the cylindrical spectrometer probe placed below the LED PCB, which made it impossible to detect the applied pressure from below. Therefore, the sensing structure had to be placed between the plastic part pressing the fingertip and the stepper motor that generates the pressing force. In practice, the pressing part had an integrated piston on top of it that squeezed against a load cell encapsulated in a plastic structure moved by the threaded shaft rotated by the stepper motor. However, in this configuration, it is rather difficult to direct the force in a perpendicular manner to the load cell due to the shape of a fingertip, and thus the load cell FS2030-000X-0500-G was deemed to have a weakness in this regard, as the sensing platform of the load cell is connected to the actual sensing unit with a rather weak rod. Therefore, a simpler and more robust 50-Newton load cell FX292X-100A-0010-L (by TE Connectivity, USA) was selected for Instrument IV. The analog voltage produced by the load cell was converted to a digital signal using a 16-bit ADC (ADS1115 by Texas Instruments, USA).

All components were controlled by a SoC (ESP32-S3 by Espressif Systems, China) that was also connected to the spectrometer using a breakout PCB (HR4--

BREAKOUT by Ocean Insight, USA). This setup enabled the SoC to provide an external trigger signal to the spectrometer, ensuring synchronized data collection across the system. The sampling rate of the system was 50 Hz. A block diagram of Instrument IV is shown in Figure 19d.

Operating Principle

The operating principle of Instrument IV is exactly the same as that of Instrument I. A fingertip is placed in a measurement chamber where the pressing bar squeezes it against the optical sensing unit, in this case the LED PCB and the spectrometer probe below it.

5.2 Depth-Resolved Blood Pressure

One of the main contributions of this thesis is the extension of BP measurement from large arteries to microvascular vessels by coupling a pressure generation and sensing system with an optical measurement system. The resulting BP values are referred to as depth-resolved BP in this section, as the technique effectively measures the pressure from large arteries buried deep in the tissue to smaller vessels closer to the surface of the skin.

5.2.1 Working Principle

The working principle is based on the following principles discussed in Chapter 2. i) The penetration depth of light into the skin is dependent on the wavelength of light, generally increasing in the visible and very short NIR region (approximately 400–900 nm). ii) The organization of the cutaneous vasculature is such that the blood conducting large arteries buried deep in the tissue branch out into flow-regulating arterioles, which themselves branch out into the superficial capillaries responsible for the exchange of substances and gases with the tissue. iii) BP decreases with decreasing blood vessel size (from large arteries to arterioles, and finally to capillaries). iv) Finally, and importantly, varying the level of external pressure of a blood vessel changes the loading of the vessel wall and allows the extraction of hemodynamic information.

With respect to point iv), squeezing the fingertip in a gradual manner against a piston and its surrounding area (Instrument I) or against a flat sensor module (Instrument IV) results in an oscillometric response. In such measurements, the amplitude of the AC component of the recorded pressure signal changes due to the response of the blood vessel walls to changing transmural pressure ($\mathrm{P_t}$), defined as $P_t = P_a - P_e$, where P_a is the pressure inside the blood vessel and P_e is the external pressure, caused by the pressing mechanism. The maximum amplitude occurs at $\mathrm{P_t} = 0$ mmHg where the vessel wall is unloaded. For large arteries, this point is also known as the MAP and it is widely used in automatic non-invasive BP monitoring devices that, with the help of more or less proprietary algorithms, use this point along with the shape of the oscillogram to compute SBP and DBP values. [172; 173] This oscillometric response can also be mathematically modeled under different assumptions for pulse pressure, arterial stiffness, and device configuration [185]. In addition to pressure signals, the oscillometric response has also been shown to occur in the volumetric signals measured by PPG sensors [169]. Figure 16c illustrates how, due to tissue optics, the different MWPPG channels of Instrument I probe the fingertip differently, with each channel effectively producing different volumetric oscillograms.

Taking into account the above principles and the configuration of Instruments I and IV, it should therefore be possible to obtain hemodynamic information from different parts of the vasculature with the instruments by changing the level of external pressure in a controlled way. The pressure sensing modules of the instruments detect the pulsations of the large arteries, while the MWPPG sensor probes the tissue volume at different depths, depending on the wavelength of light. Thus, for example, a steadily increasing level of external pressure should result in oscillograms where the amplitude initially increases, reaches maximum at the level corresponding to the mean BP in a given blood vessel, and decreases from thereafter. Note that the hemodynamic response is independent of the technique used to generate the external pressure, and thus both tonometric devices (Instruments I and IV) or cuff-based devices (Instrument III) can be used.

5.2.2 Experimental Results

Extracting BP from different depths of the skin was studied in Human Study Ia with Instrument I and later in Human Study IV utilizing the high spectral resolution of Instrument IV. The principle of extracting oscillogram amplitude envelopes from raw pressure and optical signals is shown in Figure 20a. As already explained, in the oscillometric BP measurement method, the point of maximum amplitude closely corresponds to that of the MAP [185], and optical PPG signals measuring volumetric changes show a similar phenomenon, with amplitudes initially increasing and subsequently decreasing as external pressure increases. An example of this is shown in Figure 20b, which shows extracted amplitude envelopes for all six channels, five optical channels and a pressure channel, of Instrument I.

Results on Human Study Ia dataset show that the tonometric pressure sensing method is able to extract good quality pressure signals with MAP readings close to those of the automatic brachial cuff reference device, as shown by the Bland-Altman plot in Figure 20c. The mean difference was -1.2 mmHg with an SD of 5.9 mmHg, both well within the pass criterion of ≤ 5 and ≤ 8 mmHg, respectively, set in the non-invasive sphygmomanometer validation standard ANSI/AAMI/ISO 81060-

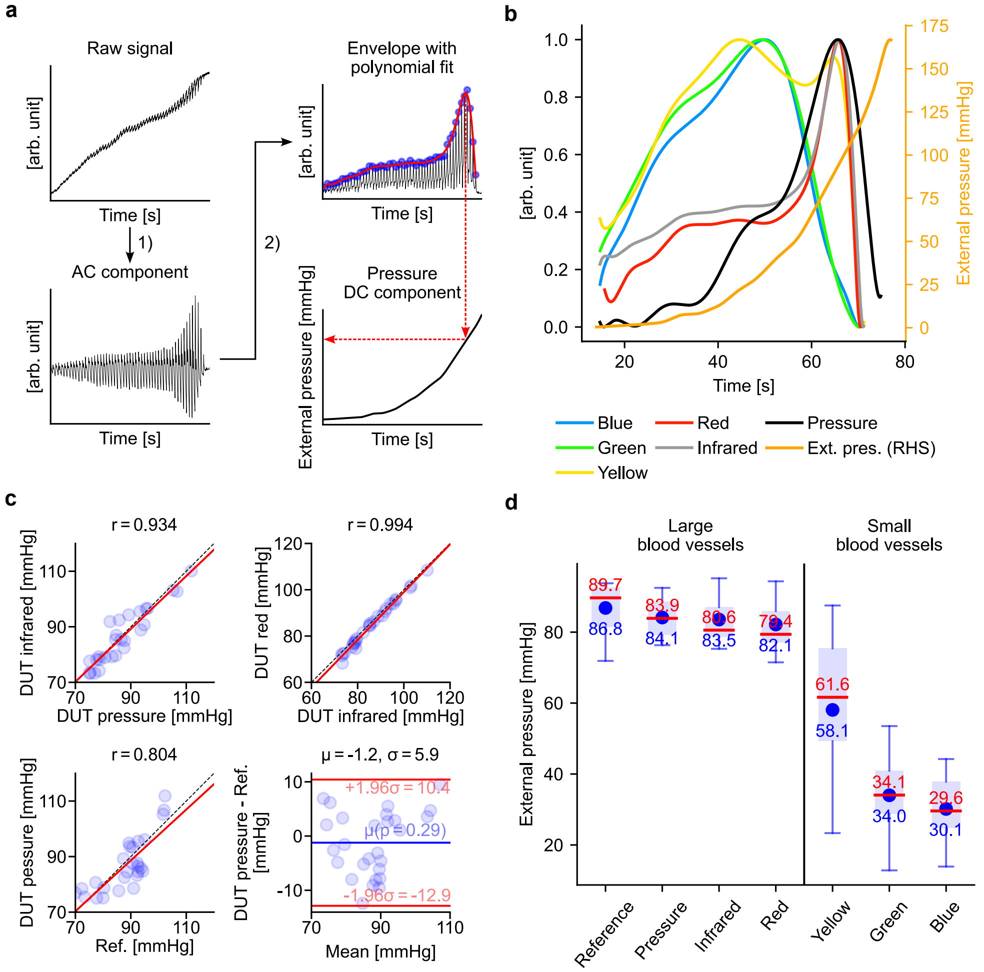

Figure 20. Human Study Ia results on maximum oscillometric pressures (MOPs). The term *pressure* refers to the pressure channel (similarly as *blue* to blue channel) whereas the term *external pressure* refers to the measured external pressure. a. Pipeline for MOP extraction. 1) Extract the AC component with a band-pass filter and, if it is a PPG signal, flip the signal. 2) Obtain the envelope with the Hilbert transformation, detect envelope peaks and calculate a polynomial fit based on the peaks. The external pressure value corresponding to the maximum of the polynomial fit is determined as the MOP. b. An example of normalized oscillogram envelopes. c. Correlation plots and a Bland-Altman plot for the evaluation of the agreement between the developed device (abbreviated as DUT, i.e. device under test) and the reference BP monitor. d. Box plots of the MOPs, with the red and blue colors representing the median and mean values, respectively. Data from one participant with high BP readings (138/84 mmHg) was excluded for clarity. The figure is from [86].

2:2013 [186].

In the 1980s it was shown that IR signal shows close correspondence to pressure signal in terms of the pressure level corresponding to the maximum amplitude

[169]. The correlation plots in Figure 20c show that red light also correlates strongly, although less strongly than IR, with the pressure signal in terms of the maximum amplitude pressure level. This is also evident in Figure 20d, which shows that red light reaches maximum amplitude at similar pressure levels to the IR and pressure signals. Thus, it can be concluded that pressure and volumetric signals measured at wavelengths corresponding to red light and IR probe the high-pressure large arteries deep in the tissue.

However, the interesting part in Figure 20d occurs at wavelengths shorter than red light. The level of external pressure at which the maximum oscillation amplitude occurs clearly decreases. Considering the large deviation from the pressure level of the large arteries (probed by the pressure, IR and red channels), a new term, maximum oscillometric pressure (MOP), was coined to refer to any pressure level at which a maximum oscillation amplitude of a given signal is reached. Note that for channels probing the large arteries MOP $\approx$ MAP. MOP is lowest for the blue channel closely followed by the green channel, with mean values of 30.1 and 34.0 mmHg, respectively. In literature, capillary BP is only about 10–20 mmHg [42; 43; 44; 45], while in the arteriolar limb of the capillary BP is about 40 mmHg [42]. These values suggest that blue and green light have an arteriolar contribution instead of probing purely superficial capillaries.

The yellow channel had clearly the largest MOP deviation, and is thus clearly different from the rest of the channels. The reason for the large deviation is due to the two-peak oscillogram nature of the yellow channel, with the oscillogram often having a peak closely corresponding to that of the blue and green channels and another closely corresponding to that of the red and IR channels. This is visualized in Figure 20b.

An important observation in Figure 20d is how the shape of the BP curve resembles that of the systemic blood circulation illustrated in Figure 5, where BP decreases as the type of blood vessel changes from the arteries to arterioles, capillaries, venules, and veins [46]. The absolute MOP levels of the different channels and the shape of the resulting curve, thus, imply that the channels are affected differently by the different compartments (mainly the arteries, arterioles, and capillaries) of the cutaneous vasculature.

Human Study IV performed with Instrument IV partly continued where Human Study Ia left in trying to obtain better understanding of the role of light wavelength in the measurement. The significantly better optical resolution of Instrument IV vs. Instrument I (99 channels with a width of 3 nm vs. 5 channels) yielded a much more detailed picture of the MOP curve, as shown in Figure 21. Overall, the shape of the MOP curve is similar and again closely resembles the pressure curve of the systemic circulation in Figure 5. However, the increased optical resolution clearly shows that the channels divide into three bands: i) shorter wavelength channels < 590 nm, ii) transition band channels between 590 and 630 nm, and iii) longer wavelength

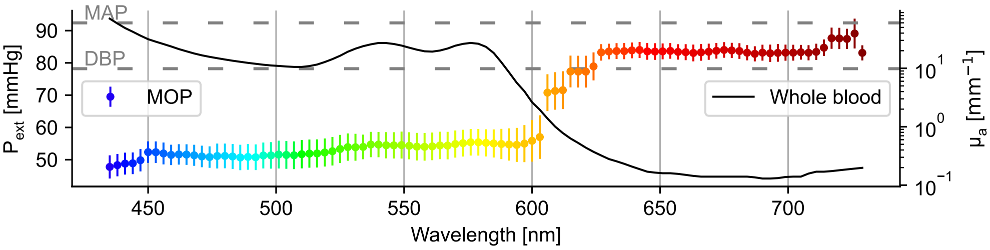

Figure 21. MOPs computed from the dataset IV are presented as *mean* ± *standard error (SE)* on the left axis while the absorption spectrum of whole blood ($SO_2 > 98\%$), based on [187], is on the right axis. The figure is adapted from [87].

channels > 630 nm. The yellow channel of Instrument I falls into the category of the transition band, and indeed the most drastic changes in MOPs in both studies Ia and IV, occur within these wavelengths. Otherwise, the figures 20d and 21 are similar with MOPs being clearly lower for channels corresponding to blue and green light, while channels corresponding to red light and NIR having clearly higher MOPs.

The drastic change in the transition band and the overall shape of the MOP curve, is explained by the absorption of light by blood, and mostly hemoglobin. Based on the Figure 6 in Section 2.2.1, absorption of light is high for light below 590 nm, which means that the channels below it are not able to penetrate deeply as blood in the more superficial blood vessels strongly absorbs light. Between 590 and 630 nm the absorption coefficient decreases rapidly, enabling the channels to probe deeper layers. By 630 nm the absorption coefficient has decreased enough for the longer-wavelength channels to probe the large arteries buried deep in the skin.

5.2.3 Simulation Results

An MC model was developed to gain understanding on Human Study Ia results. A tissue model presented in the lower panel of Figure 22 was developed to represent an approximate organization of a fingertip in terms of skin structure, blood vessels, and 3D shape (see original Publication I for more details). The simulation model was run with six different scenarios with each scenario mimicking a step during an oscillometric measurement where the external pressure is steadily increased. The scenarios were, as presented in Publication I [86]:

A the base scenario where the contact pressure of the MWPPG sensor is zero;

B occlusion of the papillary layer;

C occlusion of the papillary and upper blood net layers;

D occlusion of the upper half reticular dermis and the layers closer to the surface of the skin;

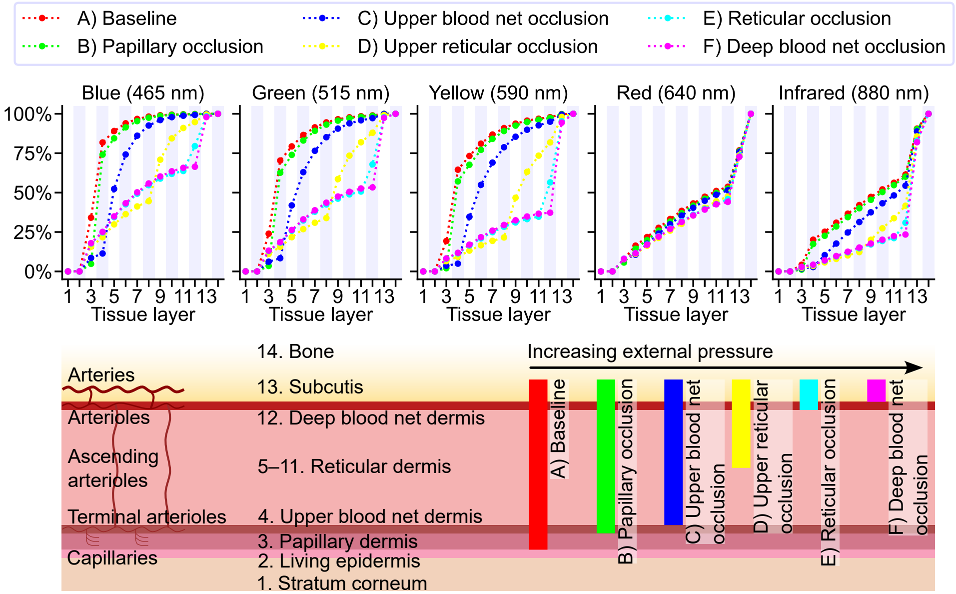

Figure 22. Layer-by-layer cumulative absorption distributions in each simulated scenario. To improve resolution, the reticular layer, which is notably thick, was divided into seven sublayers. Absorption from the first two layers of the epidermis was excluded due to the high melanin absorption in the living epidermis, which complicates visualization, and also due to the layers not containing any blood. The vertical colored bars in the tissue model indicate the blood-containing layers for each scenario. For instance, in the baseline scenario, approximately 82% of the simulated photon packet energy for the blue channel in layers 2—13 is absorbed by layer 4. The figure is adapted from [86].

E full occlusion of the reticular dermis and the layers before it; and

F occlusion of the deep blood net layer and the layers before it.

These scenarios have been illustrated in the lower panel of Figure 22. The logic behind the scenarios is that the more superficial, lower-pressure, blood vessels occlude before the high-pressure blood vessels deep in the skin. Similar logic was used in [188] where the origins of green light PPG was studied, with an argument that skin compression reduces the blood content of the skin, particularly the venous blood, with the subsequent effect of increasing the probing depth.

The upper panel of Figure 22 shows cumulative absorption distributions across tissue layers, excluding the epidermal layers that lack blood. A key observation is that the red channel exhibits smaller variations compared to the IR channel. This is due to the lower blood absorption coefficient of red light: oxygenated hemoglobin, which predominates at the assumed 98% oxygen saturation in the simulations, absorbs IR light more strongly than red light. As occlusion progresses and blood is depleted from tissue layers, the IR channel displays greater absorption in the deeper layers. However, both channels are notably influenced by absorption in these deeper layers, which contain large arterioles and arteries, resulting in similar tissue probing characteristics. [86]

The shorter wavelengths of the spectrum, specifically the blue, green, and yellow channels, exhibit more pronounced variations between scenarios compared to the longer wavelengths. These channels show high absorption in layers containing capillaries and small arterioles under both baseline and papillary occlusion conditions. Even in scenario (C), their distributions remain similar, with deeper layers contributing more at longer wavelengths. However, in scenario (D), noticeable differences arise, with the yellow channel showing the most significant changes. Here, absorption becomes predominantly influenced by the deeper tissue layers. By scenario (E), the yellow channel has a greater contribution from deeper tissue layers than the red channel. In summary, at low external compression pressures, the shorter-wavelength channels primarily probe the smaller blood vessels near the skin surface. As external compression pressure increases, they shift to probing deeper and larger blood vessels as blood is displaced from the superficial layers. [86]

5.3 Effects of Contact Pressure on Multi-Wavelength Photoplethysmograms

5.3.1 Pressure Ramp

To gather further insights into the origins of the MWPPG signals, Pearson correlation coefficients were calculated for the PPG AC components in the dataset IV, shown in Figure 23. The correlation coefficients exhibit a similar division between the MWPPG channels as in Figure 21 about the MOPs. The shorter-wavelength channels below the transition band between 585–615 nm correlate strongly together, as do the channels above the transition band. Considering that the transition band occurs in a wavelength range where blood absorption decreases rapidly, it was hypothesized that blood absorption is a key factor in oscillometric PPG measurements. It is reasoned that area under curve (AUC) values of low-pass filtered (cutoff frequency of 8 Hz; see Publication IV and its Supporting Information for further details on the computation of AUC) PPG signals approximate the total blood volume (both non-pulsatile and pulsatile) probed during a measurement considering that PPG measures changes in blood volume. Figure 24 shows that the AUCs clearly follow the absorption spectrum of whole blood, after removing the intensity variation between the PPG channels and the variation between individuals.

In recent years, perfusion index (PI), which is especially affected by vascular tone and stroke volume, has attracted renewed interest [78], with low values, for example, being associated with severe postoperative complications or death in acute high-risk surgical patients [189]. Thus, PI was calculated for the dataset IV in addition to

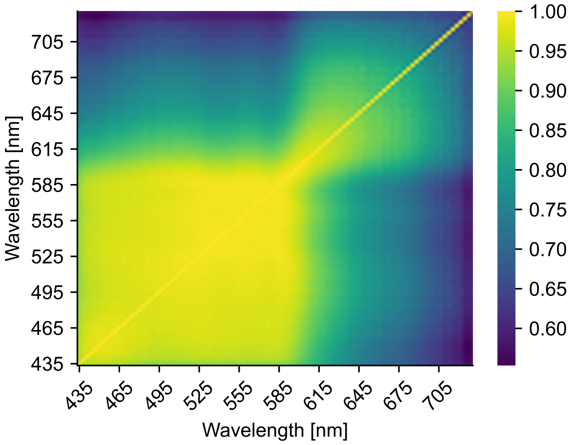

Figure 23. Spatial sensitivity map of the mean correlations between the AC components of different MWPPG channels in the dataset IV. The figure is from [87].

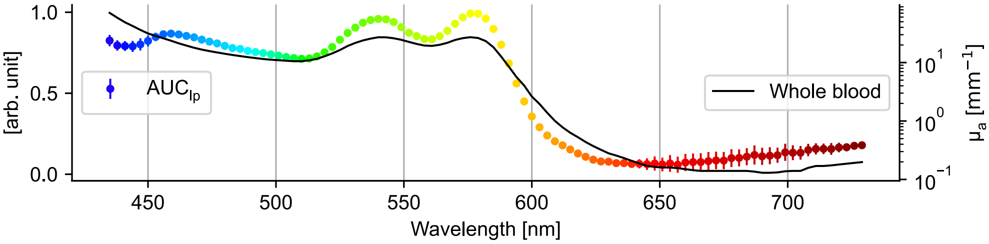

Figure 24. Lowpass-filtered PPG areas, AUC$_{\text{lp}}$, computed from the dataset IV on the left axis, and the absorption spectrum of whole blood, on the right axis. The absorption coefficient (μ_a) of whole blood ($SO_2 > 98\%$) is based on [187]. The figure is adapted from [87].

DC component level changes, which is another parameter affected by vasomotor activity [1]. These two parameters are closely related as PI is calculated as the ratio of pulse waveform amplitude to DC component level. These two parameters were calculated for two channel groups, separated at 615 nm, an approximate midpoint in the transition band, considering the clear division discussed above. The results are shown in Figure 25.

The AC component is the predominant factor in PI, as evidenced by the peak values occurring around P_t = 40 mmHg (mean MAP of 92 mmHg, see the Table 3, minus an approximate MOP of 54 mmHg in Figure 21) for wavelengths below 615 nm, and around P_t = 10 mmHg (92 mmHg minus an approximate MOP of 83 mmHg in Figure 21) for wavelengths above 615 nm. Further evidence is provided by the near-zero PI values in the negative P_t region for channels below 615 nm. This occurs because the AC components exhibit minimal pulsation at such elevated external pressure levels, since the more superficial, lower-pressure blood vessels targeted by

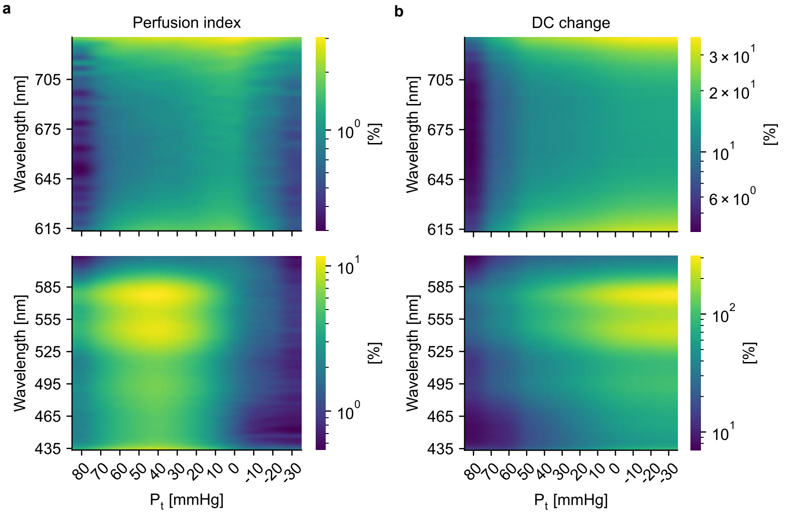

Figure 25. Dataset IV results on PI and DC component level changes, calculated as mean values over the whole dataset and as a function of 10 mmHg wide P_t bins. a. PI values. b. DC component level changes. The figure is from [87].

these channels are already occluded. In general, the highest PI values are observed for channels within the 525–585 nm range (corresponding to green and yellow light), with slightly higher values at the upper end of this range. The channels below and particularly above this band exhibit significantly lower PI values. [87]

The results for the DC component changes are similar to the PI results with the channels below 615 nm showing significantly larger changes than those above the threshold. In particular, the highest values are again obtained for channels ranging from 525 to 585 nm where the absorption spectrum of whole blood has two distinct peaks. In general, the results show that PI and DC component level are sensitive to sensor contact pressure, which complicates their usage in clinical analysis. [87]

5.3.2 Pressure Steps

Instrument III and the related Huma Study III dataset were designed to study how PPG sensor contact pressure changes PPG-derived parameters SpO_2, PAT and various PPG and its second derivative, also known as acceleration PPG (APG), based features. These parameters have been illustrated in Figure 26. Each of these three categories are presented separately below. The parameters were studied from the perspective of linear regression for statistical significance and coefficient of variation (CV) in the positive P_t range (which is the likely pressure range for real-world PPG applications), and plotting the parameters as functions of pressure steps. The pressure steps have been converted into physiologically meaningful P_t instead of us-

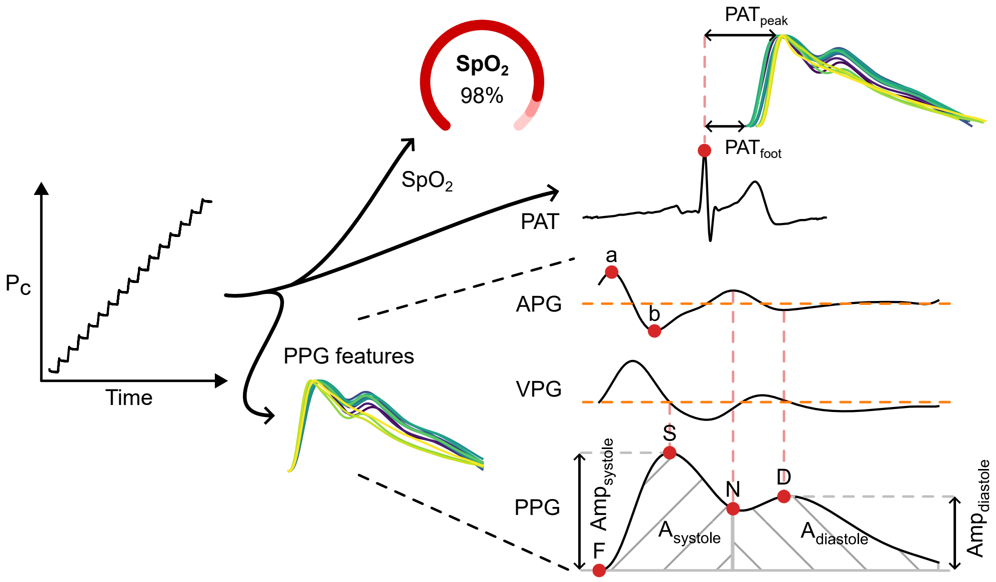

Figure 26. Illustration of the parameters calculated from dataset III. VPG (velocity PPG) and APG (acceleration PPG) are the first and second derivatives of PPG, respectively. PPG waveform points F, S, N, and D refer to waveform foot, systolic peak, dicrotic notch, and diastolic peak, respectively. The waveform points, S, N, and D can be detected with the help of VPG and APG, as illustrated by the vertical dashed lines.

ing absolute pressure values. Figure 27 presents an example of a measurement in Human Study III dataset.

Peripheral Oxygen Saturation

Regression analysis revealed a statistically significant relationship between P_c and SpO_2 ($p = 0.0034, < 0.05$). However, SpO_2 values remained largely stable at higher positive P_t levels, increasing approximately 10–20 mmHg before reaching the DBP level and peaking at 100% slightly above the MAP. The largest deviation from the theoretical SpO_2 maximum of 100% was about 1.9 percentage points. As shown in Figure 28b, this increase is attributed to the IR component rising relative to the red component, with the IR AC/DC ratio increasing more rapidly than that of the red channel. Figure 28c shows that the IR channel amplitude begins to rise before the DBP level, while the DC levels exhibit a similar trend, as illustrated in Figure 28d.

The relative insensitivity to low levels of P_t, with changes starting 10-20 mmHg below DBP, is in agreement with the findings in [190]. However, unlike in [190], where the values stabilized, the values in Figure 28 continue to change, possibly due to different sensor placements (forehead vs. fingertip). Increasing P_c also increased SpO_2 estimation errors, consistent with the findings in [191]. Both studies

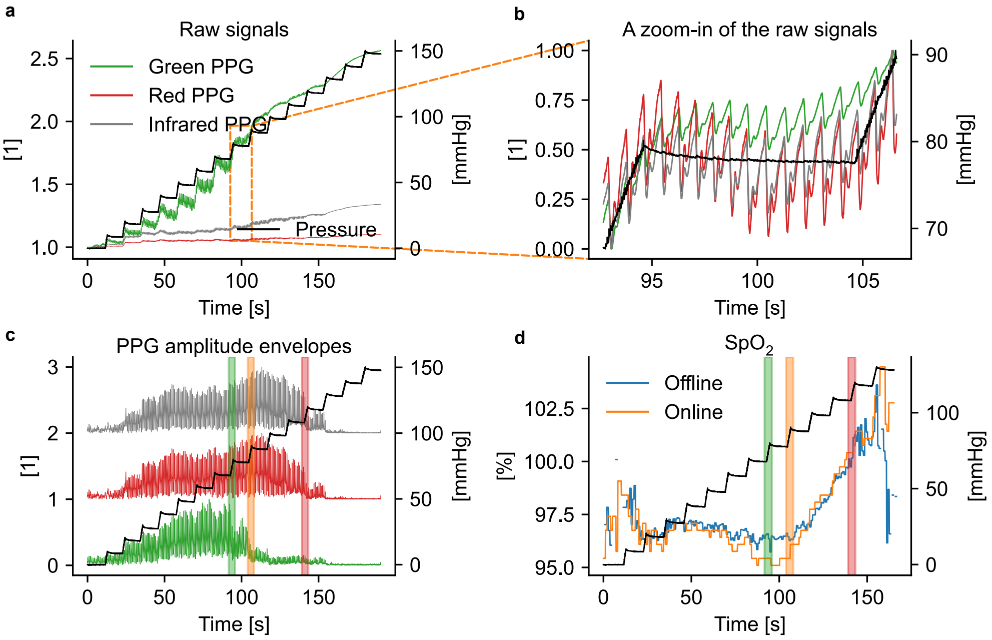

Figure 27. Example measurement from dataset III. The right-hand axis in all panels shows cuff pressure. a. Normalized raw PPG signals, with the green channel exhibiting the largest DC component change. b. Zoomed raw signals normalized to [0, 1], showing clear PPG waveforms. c. Normalized amplitude envelopes with a clear oscillometric response. DBP, MAP, and SBP from the reference device are marked with green, orange, and red bars, respectively. d. Online and offline SpO$_2$ calculations, excluding higher pressure steps due to total occlusion. The figure is from [183].

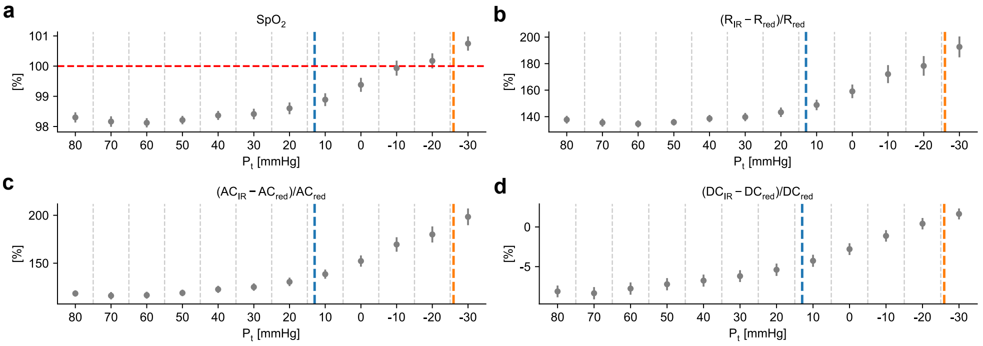

Figure 28. SpO$_2$ results (mean ± standard error) as a function of P_t (e.g., P_t = 80 mmHg covers [85, 75) mmHg etc.). Mean reference device DBP and SBP values are presented as blue and orange, respectively, vertical dashed lines. a. SpO$_2$ shows an increasing pattern. b. The IR ratio, R_{IR}, begins to increase relative to that of the red channel near P_t = 20 mmHg. c. IR amplitudes also tend to increase relative to those of the red channel near P_t = 20 mmHg. d. IR DC component increases faster than that of the red channel. The figure is from [183].

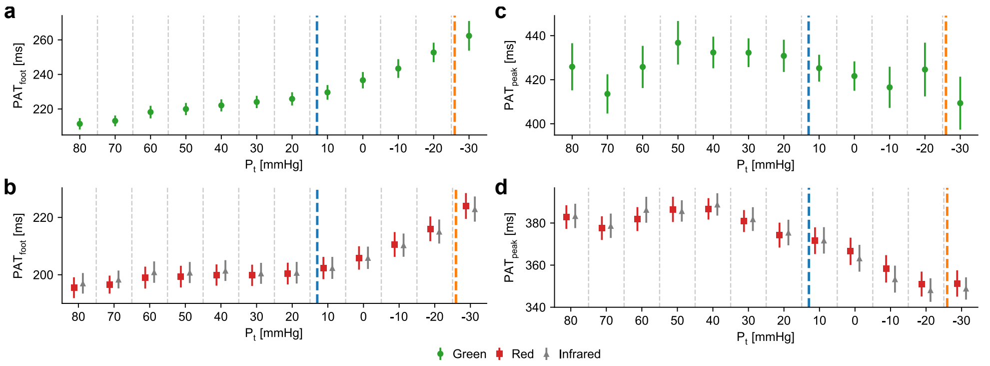

Figure 29. PAT results (mean ± standard error) presented in a manner similar to that in Figure 28. Mean reference device DBP and SBP values are presented as blue and orange, respectively, vertical dashed lines. PAT$_{foot}$ results are in figures a and b while PAT$_{peak}$ results are in figures c and d. The figure is from [183].

showed that IR amplitudes increased more than the red amplitudes with rising P_c. The hypothesis presented in [190] that higher P_c reduces venous blood effects, thus increasing SpO_2, is supported, but the expected stabilization at low P_c was not observed. Overall, the stability of SpO_2 at low P_c suggests that SpO_2 can be measured with patch-like wearables that are unable to exert significant P_c on the skin.

Pulse Arrival Time

PAT$_{foot}$, presented in Figure 29a, shows a clear increasing trend in the green PPG channel, accompanied by smaller standard errors, while the red and IR channels, presented in Figure 29b, exhibit an upward trend starting near the DBP level. In contrast, PAT$_{peak}$, presented in Figure 29c, for the green channel fluctuates with larger standard errors, whereas the red and IR channels, presented in Figure 29d, display a consistent decrease beyond P_t 40 mmHg. The observed behavior of the red and IR channels aligns with the findings reported in [192], although a U-shaped pattern prior to the increase in PAT$_{foot}$ values is not visible in Figure 29b. This discrepancy may be attributed to the lower sampling rate used in our measurements (100 Hz, upsampled to 500 Hz, compared to 1 kHz).

Overall, PAT$_{foot}$ demonstrates greater stability and predictability compared to PAT$_{peak}$. The influence of P_c on PAT is statistically significant across all cases except for the green channel PAT$_{peak}$, as shown in Table 5. In the positive P_t region, the maximum differences in PAT$_{foot}$ are 25 ms, 10 ms, and 9 ms for the green, red, and IR channels, respectively, while for PAT$_{peak}$, they are 23 ms, 20 ms, and 26 ms. The differences between the green and IR channels are 31 ms for PAT$_{foot}$ and 58 ms for PAT$_{peak}$. The higher PAT values observed in the green channel can be attributed to the pulse waveform traveling from deeper to more superficial blood vessels, introducing a delay. This phenomenon has been investigated as a potential basis for more convenient BP monitoring using a single MWPPG sensor, removing the need for a secondary sensor like the ECG in conventional PAT-based systems [21]. However, PAT-based methods for BP estimation generally show limited reliability [175; 193].

Photoplethysmogram Features

Several common PPG features, frequently used in diagnostics and indirect BP estimation techniques, see Figure 30, were computed to evaluate the effects of $\mathrm{P_c}$. These features, grouped into amplitude-based, temporal, relative, and basic categories, are summarized in Table 5. Among these, amplitude-based features, such as the perfusion index, exhibit the largest variations, while temporal and relative features show the smallest. The table also includes CV and linear regression coefficients with p values for the positive $\mathrm{P_t}$ region. Relative features are largely insensitive to changes in $\mathrm{P_c}$, as indicated by their insignificant p values. In contrast, amplitude-based features and the DC level demonstrate statistical significance, with non-linear trends observed in the green PPG channel. The temporal feature $\Delta\mathrm{T}$ is significant only in the red channel.

Sensor $\mathrm{P_c}$ can significantly affect the clinical interpretation of PPG features. For example, the APG b/a ratio, an indicator of arterial stiffness (e.g., vascular aging), begins to rise as $\mathrm{P_c}$ approaches MAP and shows notable changes beyond that point, consistent with the findings in [205]. Using the linear regression model from [202], we estimated age based on the IR APG b/a ratio, which varied from [-0.76, -0.68] in the positive $\mathrm{P_t}$ region (see Figure 30). This corresponded to an age range of 33–43 years, a ten-year difference, solely due to $\mathrm{P_c}$. Despite the minor variation in the APG b/a ratio (Table 5) and its insignificant regression coefficient, the impact on age estimation was substantial. Similar variations may occur with other features, highlighting the need to control $\mathrm{P_c}$. As shown in Figure 30, maintaining $\mathrm{P_c}$ below the DBP level minimizes this effect. For practical use, a slight contact pressure of 20—30 mmHg is recommended to reduce movement artifacts.

5.3.3 Static Pressure Hold

Human Study Ib studied the effect of PIV in measurements in which the external pressure was raised (on average 3.7 mmHg/s) slightly below the MAP, with the aim of still having pulsations in the blue channel, and held there for a bit more than two minutes. The focus was on the DC components and the pulse waveform amplitudes, as they are known to vary due to vasomotor activity [1; 206; 207].

Figure 31 illustrates the mean responses in dataset Ib during the 2-minute measurement period, while Figure 32 provides box plots summarizing the final changes observed at the end of the period. Negative changes in the DC level reflect a re-

Table 5. Summary of calculated PPG features, their CV (absolute values), and polynomial regression coefficients in the positive P_t region. The assumed regression model was first-order ($y = \beta_0 + \beta_1 x$) for most features, except for the green PPG amplitude and perfusion index, where a second-order model ($y = \beta_0 + \beta_1 x + \beta_2 x^2$) was used. Statistically significant p-values ($p \leq 0.05$) are indicated with an asterisk (*). The letters in parentheses in the *feature* column correspond to Figure 26. Note that PAT_{foot} and PAT_{peak} values are included for comparison purposes only and are not part of the categorical mean calculations. The table is adapted from [183].

Category	Feature	Reasoning	|CV|			β_1 (p_1), β_2 (p_2)		
			Green	Red	IR	Green	Red	IR
Amplitude	Amplitude (Amp): The vertical distance between the systolic peak (S) and the waveform foot (F)	BP estimation algorithms [194; 195] and usage in oscillometric measurements	0.140	0.210	0.258	9.4×10^{-3} ($8.4 \times 10^{-3}*$), -1.1×10^{-4} ($8.5 \times 10^{-3}*$)	-4.1×10^{-3} ($3.6 \times 10^{-6}*$)	-4.6×10^{-3} ($3.1 \times 10^{-5}*$)
	Perfusion index (PI): $Amp_{systole}$ / DC component level	Hemodynamic monitoring [78]	0.183	0.214	0.235	7.5×10^{-4} ($8.0 \times 10^{-3}*$), -8.0×10^{-6} ($1.3 \times 10^{-2}*$)	-4.3×10^{-5} ($2.3 \times 10^{-4}*$)	-1.1×10^{-4} ($4.0 \times 10^{-4}*$)
		Category mean	0.161	0.212	0.246			
Temporal	Crest time (CT): The time difference between the systolic peak (S) and the waveform foot (F)	Arterial stiffness [196]	0.047	0.062	0.067	3.2×10^{-4} ($3.2 \times 10^{-2}*$)	4.4×10^{-4} ($3.6 \times 10^{-3}*$)	3.9×10^{-4} ($3.4 \times 10^{-2}*$)
	ΔT: The time difference between the diastolic (D) and systolic peaks (S)	Arterial stiffness [196]	0.035	0.044	0.035	7.2×10^{-5} (5.5×10^{-1})	-3.2×10^{-4} ($1.6 \times 10^{-2}*$)	-1.6×10^{-4} (1.9×10^{-1})
	Slope transit time (STT): The slope of a line from the waveform foot (F) to the systolic peak (S)	A single point proxy for pulse transit time [197]	0.040	0.074	0.076	-3.1×10^{-3} (1.4×10^{-1})	-1.1×10^{-2} ($1.0 \times 10^{-3}*$)	-1.0×10^{-2} ($1.1 \times 10^{-2}*$)
		Category mean	0.040	0.060	0.059			
	PAT_{foot}: The time difference between the PPG foot (F) and the ECG R peak	BP estimation [198]	0.036	0.015	0.012	-2.8×10^{-1} ($3.6 \times 10^{-6}*$)	-1.0×10^{-1} ($2.1 \times 10^{-4}*$)	-7.8×10^{-2} ($2.8 \times 10^{-3}*$)
	PAT_{peak}: The time difference between the PPG systolic peak (S) and the ECG R peak	BP estimation [199]	0.016	0.018	0.022	-4.0×10^{-2} (6.9×10^{-1})	1.7×10^{-1} ($3.9 \times 10^{-2}*$)	2.1×10^{-1} ($3.3 \times 10^{-2}*$)
Relative	Reflection index (RI): $Amp_{diastole}/Amp_{systole}$	Arterial stiffness [200]	0.027	0.014	0.018	-2.4×10^{-4} (4.5×10^{-1})	-1.3×10^{-4} (4.3×10^{-1})	1.8×10^{-4} (3.7×10^{-1})
	Inflection point area ratio (IPA): $A_{systole}/A_{diastole}$	Total peripheral resistance [201]	0.050	0.096	0.060	-1.3×10^{-3} (1.4×10^{-1})	1.1×10^{-4} (9.5×10^{-1})	4.7×10^{-4} (6.8×10^{-1})
	APG b/a: The amplitude ratio of APG b (b) and a (a)	Aging and arterial stiffness [202; 203; 204]	0.029	0.047	0.034	-1.2×10^{-4} (6.3×10^{-1})	7.4×10^{-4} (9.4×10^{-2})	8.8×10^{-5} (8.0×10^{-1})
		Category mean	0.035	0.052	0.037			
Basic	DC level: PPG signal DC component level	Relation to average blood volume and tissues [1]	0.088	0.004	0.015	-3.4×10^{-3} ($1.3 \times 10^{-4}*$)	1.6×10^{-4} ($3.0 \times 10^{-5}*$)	-5.5×10^{-4} ($4.3 \times 10^{-5}*$)
		All categories mean	0.071	0.085	0.089			

duction in light detected by the photodiode, attributed to increased blood volume absorbing more light. In contrast, positive changes in waveform amplitude indicate increased perfusion by PIV, leading to stronger pulsations. Among the channels, the yellow channel shows the most pronounced DC level change, with a V-shaped trend, in which the changes decrease on both sides of the yellow channel. The blue channel demonstrates the largest increase in waveform amplitude, with a decreasing trend for

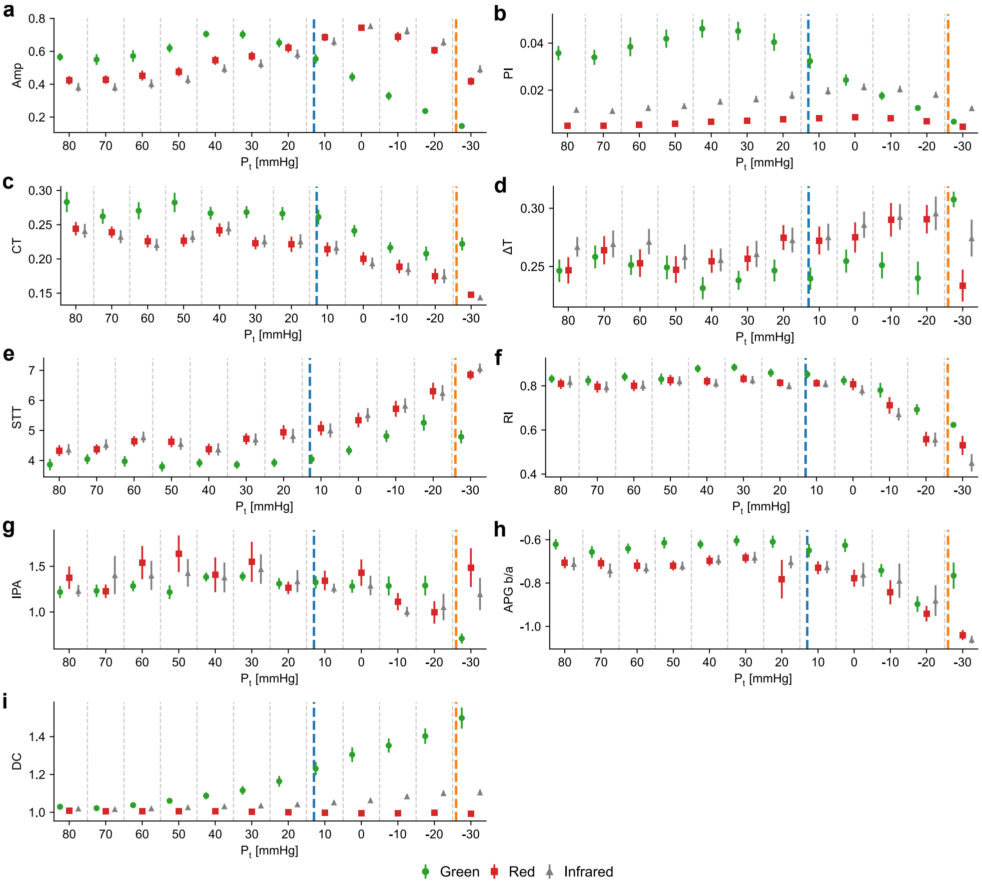

Figure 30. Results on PPG features (mean ± standard error) presented in a manner similar to that in Figure 28. Amplitude-based features are presented in figures a and b. Temporal features are presented in figures c–e. Relative features are presented in figures f–h. The results on the basic feature, DC level, are presented in figure i. See Table 5 for feature descriptions. The figure is from [183].

longer wavelengths, stabilizing around the red channel. The variance is higher in the shorter-wavelength channels compared to the longer-wavelength ones, probably because of the initial small pulse waveform amplitudes under high external pressure, allowing for a greater rebound in shorter wavelengths.

The MC simulation results in Section 5.2.3 showed that the yellow channel is the most representative of the arterioles which are known to play a significant role in the regulation of vascular tone (see Section 2.1.2). Thus, it can be argued that the large changes observed in the yellow DC component are due to arteriolar vasodilation, and that the increases in the blue and green channel AC amplitudes are a consequence of increased blood flow to more superficial blood vessels.

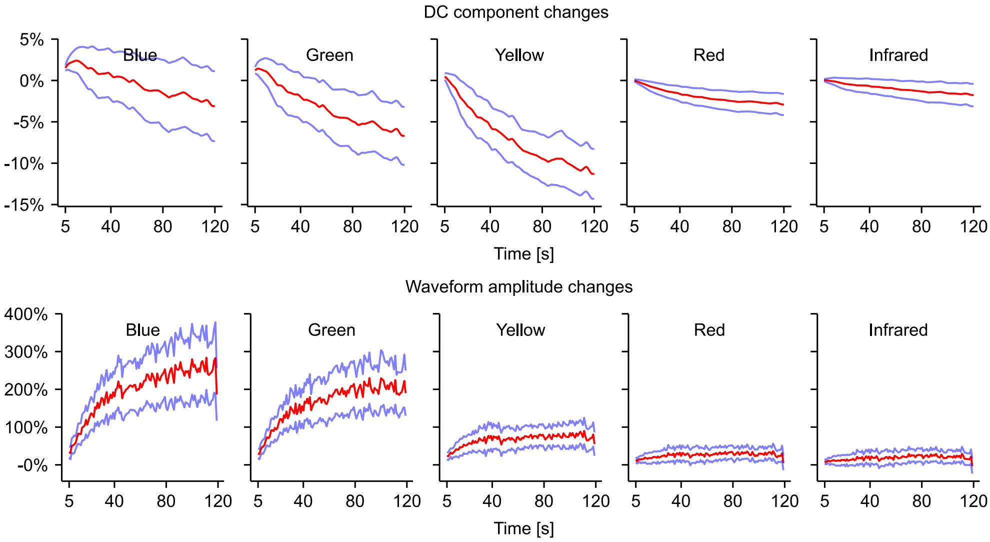

Figure 31. Mean DC component and waveform amplitude changes with 95% confidence intervals, calculated relative to the mean value during a 5-second baseline period at the start of the 2-minute static pressure hold. The figure is adapted from [86].

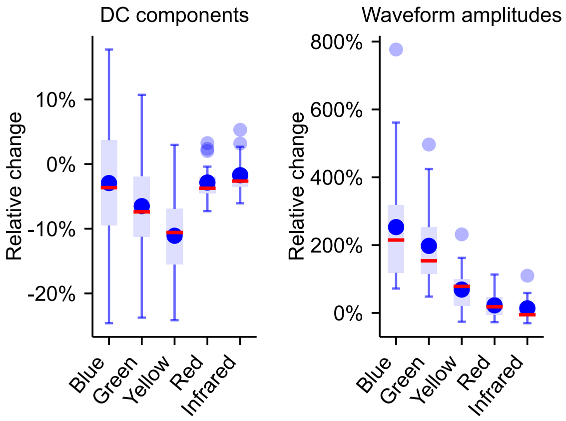

Figure 32. Box plots representing the mean values calculated over the final five seconds of the period shown in Figure 31. The red lines indicate the median values, while the blue circles represent the mean values. Adapted from [86].

5.4 Synthetic Photoplethysmograms

5.4.1 Mathematical Model

The synthetic PPG model presented in the original Publication II is inspired by the works of [208] and [209] presenting the generation of synthetic ECG signals. The derivative of a single synthetic PPG pulse waveform is expressed as a sum of Gaussian function derivatives [181]:

$$s'_{synthetic} = \sum_{i=1}^{N} -\frac{\mathbf{x_i}}{c_i^2} f(\mathbf{x_i}), \tag{10}$$

where $\mathbf{x_i}$ is a phase signal for the i^{th} Gaussian bump with values linearly spaced in the range $[-\pi, \pi]$ (i.e., a PPG pulse waveform is modeled as a rotation around a circle with values sampled at points $x_1, ..., x_n$, where $x_1 = -\pi$ and $x_n = \pi$) but with values shifted to the left or right of the center of the pulse waveform by d_i (in radians from the center point) depending on the location of the desired Gaussian bump (e.g., the Gaussian bump modeling the systolic peak of a PPG pulse waveform is shifted to the left), N is the number of Gaussian bumps (at minimum two, i.e., to model the systolic and diastolic parts of a PPG waveform), c_i is the width of the bump, and $f(\mathbf{x_i})$ is a Gaussian function:

$$f(\mathbf{x_i}) = a_i \exp\left(\frac{-\mathbf{x_i}^2}{2c_i^2}\right), \tag{11}$$

where a_i is an amplitude modifier. [181] The derivative, $s'_{synthetic}$, is then smoothed with a 2nd order Savitzky-Golay filter with a window length of 11. Smoothing handles cases where a Gaussian bump is wide enough to cause discontinuity in the final summed derivative. However, such potential discontinuities have negligible effects on the resulting waveform, as shown in Publication II. Finally, the derivative $s'_{synthetic}$ is integrated with cumulative numerical integration to obtain the final waveform $s_{synthetic}$. [181]

A complete PPG signal can be generated using a phase signal consisting of a concatenated series of $[-\pi, \pi]$ intervals. The number of samples in any given pulse waveform interval k, is calculated using the equation adapted from [209]:

$$n_k = f_s[l + b\sin(2\pi f_b \sum_{j=1}^{k-1} \frac{n_j}{f_s})], \tag{12}$$

where n_k is the length (in samples) of the pulse waveform interval k, f_s is the sampling frequency (in Hz), l is the mean pulse waveform interval length (in seconds), b is the breathing coupling coefficient (assumed to be 0.1) and f_b is the breathing frequency (in Hz). Thus, HR in any given interval k is defined by n_k. For example, $n_k = 80$ and $f_s = 100$ equals an HR of 75 ($= 60/(80/100)$) beats per minute.

The big benefit of parametric signal generation is the automatic labeling of the feet/onsets with simple rules. The first foot should be near the start of the synthetic signal, while the remaining feet should be located near the end of the modeled pulse waveform intervals. The potential foot locations can therefore be determined using an array in which each element is incremented from the previous element by the pulse length n_k, resulting in the sequence $\{0, n_{k_1}, n_{k_1} + n_{k_2}, ...\}$. Each foot is then

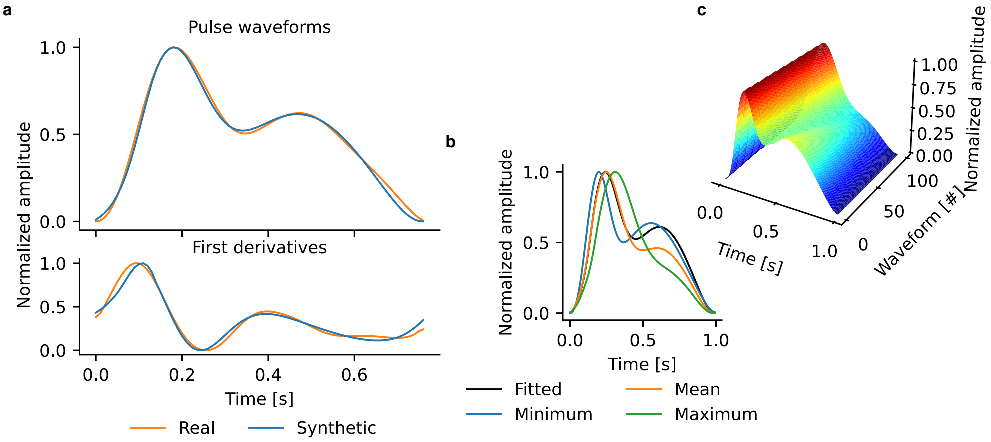

Figure 33. Synthetic waveform fitting. a. A real PPG pulse waveform alongside its corresponding fitted synthetic waveform. b. The original fitted waveform, from figure a, together with waveforms generated using minimum, mean, and maximum parameter values (see Table 6). c. Evolution of the synthetic waveform from one generated with the minimum parameters to one generated with the maximum parameters. Adapted from [181].

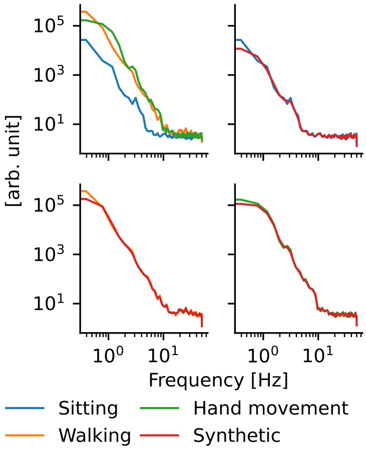

Figure 34. Power spectral densities (PSDs) used in noise generation. The upper left panel shows the mean power spectral densitys (PSDs) computed for each measurement type (sitting, walking, and hand movement). The remaining panels present the computed mean PSDs alongside their sampled (synthetic) counterparts for each measurement type. The similarity between the computed and synthetic PSDs confirms that the noise generator functions as intended. Adapted from [181].

identified as the minimum point found within ± 100 milliseconds around these potential locations. For CNN model training, this series of feet is transformed into a label signal where each foot is represented by five ones, the rest of the elements being

Table 6. Parameter ranges for generating randomized synthetic PPG signals. The table is adapted from [181].

(a) PPG waveform parameter ranges.

Parameter	Waveform bump Systole	Waveform bump Diastole	Unit
d (shift)	[-2.0, -1.4]	[0.4, 1.0]	rad
c (width)	[0.5, 0.9]	[1.7, 2.1]	arb. unit
a (amplitude)	[5.0, 10.0]	[5.0, 9.0]	arb. unit

(b) Ranges for the rest of the parameters.

Parameter	Range	Unit
l (mean waveform length)	[0.4, 1.3]	s
f_b (breathing frequency)	[0.15, 0.4]	Hz
a_{noise} (noise amplitude)	[0, 1.5]	arb. unit

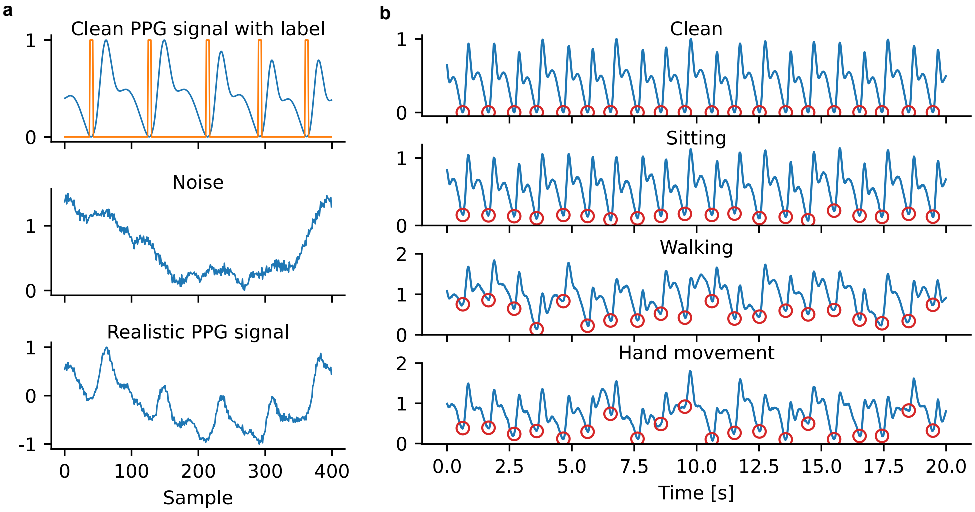

Figure 35. Examples of synthetic PPG signals. a. A synthetic PPG signal with foot location labels, generated noise, and the final realistic signal normalized to $[-1, 1]$. b. Longer synthetic PPG signals from the same clean signal and noise generated using the same random seed. The figure is from [181].

zeros.

Figure 33a shows a real PPG pulse waveform together with a fitted synthetic waveform. The parameters of the fitted waveform were used to experimentally derive model parameter ranges to generate a wide range of different pulse waveforms. The parameter ranges are shown in Table 6, while Figure 33b shows the waveforms generated from the range and 33c shows the full range of the waveforms.

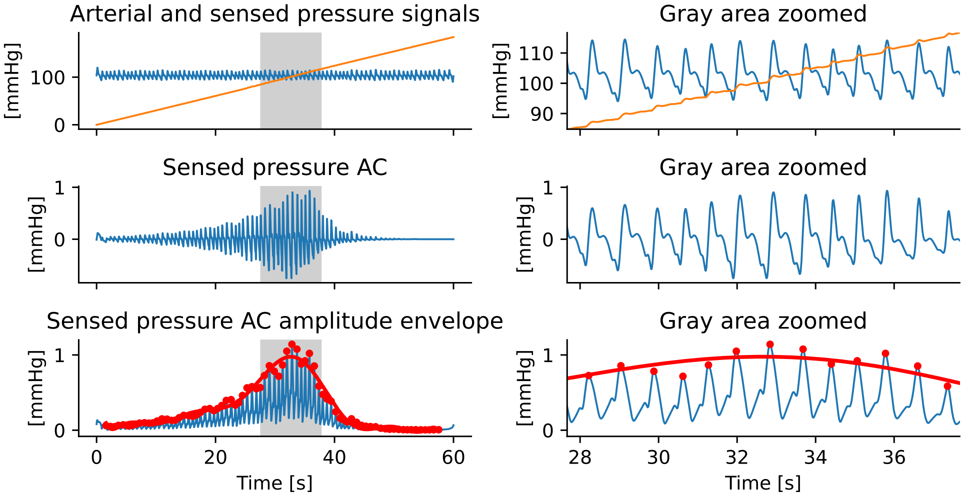

Figure 36. Synthetic BP oscillogram. Top panel: Synthetic pressure signal (blue) generated with three Gaussian bumps representing a typical arterial waveform extracted from a fingertip with BP of 120/80 mmHg. The orange line is the simulated pressure signal sensed with a setup similar to Instrument I assuming linearly increasing external pressure. Note the superimposed arterial pressure signal in the closeup figure on the right. Middle panel: AC component extracted with band-pass filtering from the sensed pressure signal. Bottom panel: Computed amplitude envelope of the AC component.

The synthetic model alone generates unrealistically clean PPG signals. Therefore, a noise generator based on converting a PSD from the frequency domain to the time domain using the algorithm presented in [210] was developed. Three measurements (each a little more than two minutes long) were recorded while sitting, walking, and moving the hand with the device in random ways. These measurements were then divided into four-second blocks, corresponding the CNN model inference period of Instrument II. The timeseries blocks were converted into PSDs using the Welch's method [211] and the computed PSDs were averaged, as shown in Figure 34. The averaged PSDs were used as the basis for creating interpolation functions that another function uses to create randomized time-domain noise. The generated noise effectively represents the noise specific to the device and measurement protocol, eliminating the need for a parametric synthetic noise model. Figure 35a illustrates the process of generating realistic PPG signals while 35b shows examples of longer signals with different types of noise.

The synthetic model can be easily modified for specific purposes or coupled with additional models. The model could, for example, be modified to factor in arrhythmia by adjusting the process of creating pulse waveform intervals (Equation 12) to include random irregularities. Similarly, the model could be coupled with, for example, the mathematical model for oscillometric BP measurement presented in [185]

Table 7. The CNN models analyzed in Human Study II. All layers are convolutional, except those labeled *Norm.* which are normalization layers. Convolutional layer parameters are specified as the number of filters, dilation rate, and activation function. Layers are listed from top (first layer) to bottom (last layer). The output shape of each layer matches the input layer shape, i.e., 400 samples. The table is adapted from [181].

	Reference NN model	NN model 1	NN model 2
Kernel size	3	5	5
Parameters	3,169	296	28
Trainable parameters	3,169	265	23
Model size [kB]	21.3	7.7	3.6
Layers	4, 1, elu	2, 1, swish	2, 2, swish
	8, 2, elu	Norm.	Norm.
	8, 4, elu	4, 2, swish	1, 4, sigmoid
	16, 8, elu	Norm.	-
	16, 16, elu	8, 4, swish	-
	32, 32, elu	Norm.	-
	1, 64, sigmoid	1, 8, sigmoid	-

using synthetic pulse waveforms as input to the model. This has been demonstrated in Figure 36, which shows an example of a synthetic oscillometric pressure measurement, although the model could just as well be used to generate synthetic MWPPG oscillograms which are similar in nature. The combined model can create a range of oscillometric signals varying in BP, HR, arterial stiffness, pulse waveform shape, noise, and system configuration (e.g., rate of change in external pressure and BP monitor cuff size or the air cushion configuration used in the tonometric setup presented in this thesis). Such a combined model could be used, for example, to train an AI quality detector for oscillometric measurements.

5.4.2 Convolutional Neural Network Based Heart Rate Calculation

The synthetic model was used to generate 200,000 four seconds long labeled PPG signals. The signals were used as a training set for three different CNN models, summarized in Table 7 with further details in the original Publication II. The models detect the PPG waveform onsets that mark the beginning of a new pulse and are used to calculate HR. The trained models were used to detect the waveform feet in the dataset II, with the possibility to run model inference directly on Instrument II.

HR computed from the detected feet was compared with several common peak detection algorithms, including the AMPD algorithm [177], its optimized version

Table 8. Summary of algorithm comparison results. The table shows the mean precision, recall, F1 scores, and HR mean absolute error (MAE) relative to the ECG for each foot detection algorithm and measurement type. The best values in each column are highlighted in bold black, while the worst are in bold red. Mean values are calculated over all measurement durations (2 minutes). The table is adapted from [181].

	Sitting				**Walking**				**Hand movement**				**All measurements**			
Algorithm	Precision	Recall	F1 score	HR MAE	Precision	Recall	F1 score	HR MAE	Precision	Recall	F1 score	HR MAE	Precision	Recall	F1 score	HR MAE
NN model 1	0.94	0.98	0.96	**3.1**	0.69	0.70	0.69	15.7	0.73	0.62	0.67	15.5	0.80	0.78	0.78	11.0
NN model 2	0.96	0.98	**0.97**	2.0	0.69	0.69	0.69	15.9	0.73	0.63	0.67	**15.4**	0.80	0.78	**0.79**	10.7
Ref. NN model	0.95	0.98	**0.97**	2.5	0.70	**0.72**	**0.71**	**13.7**	0.74	0.64	**0.68**	15.5	0.80	**0.79**	**0.79**	**10.2**
AMPD	**0.99**	**0.80**	**0.89**	1.3	**0.72**	**0.53**	**0.61**	17.9	**0.75**	**0.50**	**0.60**	16.6	**0.83**	**0.62**	**0.71**	11.4
AMPD (modified)	**0.91**	**0.99**	0.95	2.0	0.68	0.66	0.67	18.7	0.71	**0.65**	**0.68**	16.8	**0.77**	0.78	0.77	12.0
MSPTD	**0.99**	**0.80**	**0.89**	1.3	0.70	0.56	0.62	17.0	**0.75**	0.54	0.62	15.6	0.82	0.64	0.72	10.8
Heartpy	0.98	0.89	0.93	**1.2**	**0.65**	0.62	0.63	16.5	**0.67**	0.60	0.63	15.9	0.78	0.71	0.74	10.7
Autocorrelation	-	-	-	2.7	-	-	-	**20.2**	-	-	-	**19.0**	-	-	-	**13.4**

multi-scale peak and trough detection (MSPTD) [212], and the HeartPy algorithm [213]. Threshold-based methods, such as [214], were excluded as they generally perform poorly with short signals. Furthermore, a simple algorithm based on autocorrelation [215] was used alongside the foot detectors for HR estimation. In this method, autocorrelation was computed over 4-second signal blocks, and the location of the first peak was used to determine the pulse waveform length.

The comparison results are summarized in Table 8. The reference CNN model outperforms other methods, achieving the highest number of top values. Notably, the two smaller CNN models perform comparably well, suggesting that the limited complexity of the 1-dimensional, tightly filtered, and short PPG signals constrains the amount of information that can be extracted. Among non-CNN approaches, the modified AMPD and HeartPy algorithms perform relatively well. The modified AMPD algorithm, in particular, effectively addresses the problem of the original AMPD algorithm in detecting feet close to the end points of a signal.

6 Conclusion

PPG has emerged as the definitive sensor technique for tracking cardiovascular parameters in modern wearables and has an important clinical application in the form of pulse oximetry. However, the prevalent single, dual, and triple wavelength solutions discard most of the spectrum between approximately 400–1,000 nm, and the solutions exploring other wavelengths have so far merely aimed to improve the quality of HR estimation. According to the wavelength-dependency of light penetration into skin (based on MC simulations) and the structure of the cutaneous vasculature, utilizing more of the spectral range could offer opportunities to extract new cardiovascular parameters or improve the accuracy of existing ones. In the late 2010s research interest towards utilizing more of the spectrum started to gain traction, giving a push to MWPPG research. This thesis contributed to that and the wider PPG research by developing two MWPPG instruments that integrate controlled and measurable sensor contact pressure systems (Publications I and IV), presenting an edge AI system running an HR estimation model trained with signals generated with a developed synthetic PPG generator model (Publication II), and investigating the effects of sensor contact pressure on MWPPG signals (Publication III).

The results on the developed finger pressing method (Publications I and IV) together with the MC simulation results (Publication I) provided clear evidence that the different channels of MWPPG have different information content originating from the different compartments of the cutaneous vasculature. Combining an MWPPG sensor with an external pressure control and measurement mechanism allows to alter hemodynamics to reveal these differences, and provides a way to extract depth-resolved responses to static pressure (Publication I) and, importantly, depth-resolved BP (Publications I and IV). Therefore, the presented method not only measures the pressure of the large arteries, as is the case with current automatic non-invasive BP monitors, but also provides BP readings for the smaller blood vessels further down the vascular tree, mostly arterioles in the current state of the presented method. This has the potential to factor in the aspect of microcirculation in noninvasive, and perhaps wearable, cardiovascular monitoring, improving the diagnosis of CVDs and offering a new tool to investigate the pathophysiology of such diseases.

A related contribution in this thesis was the investigation of sensor contact pressure on PPG signals, notably the effects of uncontrolled contact pressure (Publication III). Amplitude (systolic peak derived) and DC component based parameters / waveform features for wavelengths approximately below 615 nm are sensitive to varying sensor contact pressure. Most current applications of PPG do not have a method to actively control sensor contact pressure. For example, pulse oximeters typically have a spring-based clip that applies a certain pressure based on the stiffness of the spring and fingertip size, while wearables generally do not have even that much of control. Smart watches are tightened to some more or less variable contact pressure by the user, while in smart rings the contact pressure can change significantly based on the vascular tone, from loose in cold temperatures (due to vasoconstriction) to rather tight in warm temperatures (due to vasodilation). Large changes in vascular tone are, in general, a challenge with finger-based PPG measurements, and thus active control of sensor contact pressure is beneficial.

PPG sensor contact pressure should not only be controlled, it should ideally also be measured relative to the hemodynamics of an individual (Publication III). As an example, considering two subjects with identical anatomy (i.e., the physical size, vasculature, and tissue composition) and a clip-based fingertip monitoring device (such as a pulse oximeter), assuming that one of them is hypotensive (BP below 90/60 mmHg) and the other one hypertensive (BP above 140/90 mmHg), the difference in the MAPs (70 and 107 mmHg, respectively) is 37 mmHg. Thus, the difference in the physiologically relevant P_t in these two cases is also 37 mmHg. Such a large difference, although in a quite extreme case, highlights that a fixed contact pressure approach is rather crude and adds parameter estimation inaccuracies for subjects who need medical attention the most. The effect on SpO_2 was found to be rather negligible, while certain features used in AI models, for example, for the analysis of vascular age, are indeed sensitive to contact pressure.

The ongoing strong growth in AI based analysis models requires large and representative datasets without compromising data privacy. Models trained with synthetic data generator models and accompanied with edge based model inference offer privacy secure and possibly latency optimized solution without compromising on accuracy relative to more traditional techniques (Publication II). In addition, parametric synthetic models can be rather flexibly modified to take into account more complex cases or coupled with other mathematical models replicating physiological processes. An example of this is synthetic oscillograms that resemble the real-world oscillograms recorded in the studies behind Publications I and IV.

The future research direction of PPG sensors looks inevitably directed towards multi-wavelength sensing because of its potential to create new monitoring solutions that measure hemodynamic parameters from large blood vessels to the vessels of the microvasculature (Publications I and IV). In wearables MWPPG could be used together with context-aware algorithms to dynamically select the most appropriate wavelength of light for a given measurement context and the targeted physiological parameter. For example, during exercise, motion-robust green light could be used, while blue light together with, for example, IR could be used to compute a single point PTT for vascular analysis. This growth path could benefit significantly from inverting the typical PPG system architecture, from narrow-band LEDs and wideband photodiodes to wideband LEDs and spectrometers (Publication IV). Future developments in chip-scale spectrometers would simplify PPG sensor designs and allow smaller sensor configurations while providing a richer set of physiological information.

The MWPPG research has only scratched the surface of future possibilities, and as was the case with single- and dual-wavelength PPG in its infancy, a significant amount of clinical research is needed to understand MWPPG signals in different diseases. For example, how do MOP curves (Publications I and IV) compare between hypotensive and hypertensive patients (e.g. is the pressure difference between the channels $<$ 590 nm and $>$ 630 nm smaller for hypertensive patients, i.e., a sign of pressure leakage from large arteries to smaller vessels) and what kind of responses do the different channels show in PIV measurements (Publication I) for, e.g., peripheral arterial disease or diabetic patients. More research is also needed to understand how representative the cutaneous microcirculation is of the generalized microcirculation.

List of References

[1] John Allen. Photoplethysmography and its application in clinical physiological measurement. *Physiological Measurement*, 28:R1–39, April 2007. doi: 10.1088/0967-3334/28/3/R01.

[2] Proceedings of the american physiological society. *American Journal of Physiology-Legacy Content*, 119(2):257–427, May 1937. ISSN 0002-9513. doi: 10.1152/ajplegacy.1937.119.2.257.

[3] Alrick B. Hertzman. Photoelectric Plethysmography of the Nasal Septum in Man. *Proceedings of the Society for Experimental Biology and Medicine*, 37(2):290–292, November 1937. ISSN 0037-9727. doi: 10.3181/00379727-37-9543P.

[4] Alrick B. Hertzman. Photoelectric Plethysmography of the Fingers and Toes in Man. *Proceedings of the Society for Experimental Biology and Medicine*, 37(3):529–534, December 1937. ISSN 0037-9727. doi: 10.3181/00379727-37-9630.

[5] Alrick B. Hertzman. The blood supply of various skin areas as estimated by the photoelectric plethysmograph. *American Journal of Physiology-Legacy Content*, 124(2):328–340, October 1938. ISSN 0002-9513. doi: 10.1152/ajplegacy.1938.124.2.328.

[6] Alrick B. Hertzman and John B. Dillon. Distinction between arterial, venous and flow components in photoelectric plethysmography in man. *American Journal of Physiology-Legacy Content*, 130(1):177–185, June 1940. ISSN 0002-9513. doi: 10.1152/ajplegacy.1940.130.1.177.

[7] Alrick B. Hertzman and John B. Dillon. Applications of photoelectric plethysmography in peripheral vascular disease. *American Heart Journal*, 20(6):750–761, December 1940. ISSN 0002-8703. doi: 10.1016/S0002-8703(40)90534-8.

[8] Alrick B. Hertzman and Laurence W. Roth. The vasomotor components in the vascular reactions in the finger to cold. *American Journal of Physiology-Legacy Content*, 136(4):669–679, June 1942. ISSN 0002-9513. doi: 10.1152/ajplegacy.1942.136.4.669.

[9] Takuo Aoyagi. Pulse oximetry: Its invention, theory, and future. *Journal of Anesthesia*, 17(4): 259–266, November 2003. ISSN 1438-8359. doi: 10.1007/s00540-003-0192-6.

[10] Hangsik Shin and Se Dong Min. Feasibility study for the non-invasive blood pressure estimation based on ppg morphology: Normotensive subject study. *BioMedical Engineering OnLine*, 16 (1):10, January 2017. ISSN 1475-925X. doi: 10.1186/s12938-016-0302-y.

[11] Scott Ryals, Ambrose Chiang, Sharon Schutte-Rodin, Arvind Chandrakantan, Nitun Verma, Steven Holfinger, Fariha Abbasi-Feinberg, Anuja Bandyopadhyay, Kelly Baron, Sumit Bhargava, Ken He, Joseph Kern, Jennifer Miller, Ruchir Patel, Dulip Ratnasoma, and Maryann C. Deak. Photoplethysmography—new applications for an old technology: A sleep technology review. *Journal of Clinical Sleep Medicine*, 19(1):189–195, January 2023. ISSN 1550-9389, 1550-9397. doi: 10.5664/jcsm.10300.

[12] Peter H. Charlton, Birutė Paliakaitė, Kristjan Pilt, Martin Bachler, Serena Zanelli, Dániel Kulin, John Allen, Magid Hallab, Elisabetta Bianchini, Christopher C. Mayer, Dimitrios Terentes-Printzios, Verena Dittrich, Bernhard Hametner, Dave Veerasingam, Dejan Žikić, and Vaidotas Marozas. Assessing hemodynamics from the photoplethysmogram to gain insights into vascular age: A review from VascAgeNet. *American Journal of Physiology-Heart and Circulatory Physiology*, 322(4):H493–H522, April 2022. ISSN 0363-6135. doi: 10.1152/ajpheart.00392.2021.

[13] Mikołaj Basza, Damian Waląg, Weronika Kowalczyk, Aleksandra Bożym, Michalina Ciurla, Małgorzata Krzyżanowska, Cezary Maciejewski, Wojciech Bojanowicz, Mateusz Soliński,

and Łukasz Kołtowski. Photoplethysmography wave morphology in patients with atrial fibrillation. *Physiological Measurement*, 44(4):045001, April 2023. ISSN 0967-3334. doi: 10.1088/1361-6579/acc725.

[14] M. Bester, M. J. Almario Escorcia, P. Fonseca, M. Mollura, M. M. van Gilst, R. Barbieri, M. Mischi, J. O. E. H. van Laar, R. Vullings, and R. Joshi. The impact of healthy pregnancy on features of heart rate variability and pulse wave morphology derived from wrist-worn photoplethysmography. *Scientific Reports*, 13(1):21100, November 2023. ISSN 2045-2322. doi: 10.1038/s41598-023-47980-2.

[15] Yoon La Yang, Hyeon Seok Seok, Gyu-Jeong Noh, Byung-Moon Choi, and Hangsik Shin. Postoperative Pain Assessment Indices Based on Photoplethysmography Waveform Analysis. *Frontiers in Physiology*, 9, 2018. ISSN 1664-042X.

[16] Louise Finlayson, Isla R. M. Barnard, Lewis McMillan, Sally H. Ibbotson, C. Tom A. Brown, Ewan Eadie, and Kenneth Wood. Depth Penetration of Light into Skin as a Function of Wavelength from 200 to 1000 nm. *Photochemistry and Photobiology*, 98(4):974–981, 2022. ISSN 1751-1097. doi: 10.1111/php.13550.

[17] Irwin M. Braverman. The Cutaneous Microcirculation. *Journal of Investigative Dermatology Symposium Proceedings*, 5(1):3–9, December 2000. ISSN 1087-0024. doi: 10.1046/j.1087-0024.2000.00010.x.

[18] Ville Sarkela, Harri K. Kopola, Kyosti Oikarinen, and Esko Herrala. Dental pulp vitality measurement based on multiwavelength photoplethysmography. In *Medical and Fiber Optic Sensors and Delivery Systems*, volume 2631, pages 72–83. SPIE, January 1995. doi: 10.1117/12.229169.

[19] Janis Spigulis, Lasma Gailite, Alexey Lihachev, and Renars Erts. Simultaneous recording of skin blood pulsations at different vascular depths by multiwavelength photoplethysmography. *Applied Optics*, 46(10):1754–1759, April 2007. ISSN 2155-3165. doi: 10.1364/AO.46.001754.

[20] Jing Liu, Bryan Ping-Yen Yan, Wen-Xuan Dai, Xiao-Rong Ding, Yuan-Ting Zhang, and Ni Zhao. Multi-wavelength photoplethysmography method for skin arterial pulse extraction. *Biomedical Optics Express*, 7(10):4313–4326, October 2016. ISSN 2156-7085. doi: 10.1364/BOE.7.004313.

[21] Jing Liu, Bryan P. Yan, Yuan-Ting Zhang, Xiao-Rong Ding, Peng Su, and Ni Zhao. Multi-Wavelength Photoplethysmography Enabling Continuous Blood Pressure Measurement With Compact Wearable Electronics. *IEEE Transactions on Biomedical Engineering*, 66(6):1514–1525, June 2019. ISSN 1558-2531. doi: 10.1109/TBME.2018.2874957.

[22] Sangjin Han, Donggeun Roh, Junyung Park, and Hangsik Shin. Design of Multi-Wavelength Optical Sensor Module for Depth-Dependent Photoplethysmography. *Sensors*, 19(24):5441, January 2019. ISSN 1424-8220. doi: 10.3390/s19245441.

[23] Cheng-Chun Chang, Chien-Ta Wu, Byung Il Choi, and Tong-Jing Fang. MW-PPG Sensor: An on-Chip Spectrometer Approach. *Sensors*, 19(17):3698, January 2019. ISSN 1424-8220. doi: 10.3390/s19173698.

[24] Jukka-Pekka Sirkiä, Tuukka Panula, and Matti Kaisti. Multi-Wavelength Photoplethysmography Device for the Measurement of Pulse Transit Time in the Skin Microvasculature. In *2020 Computing in Cardiology*, pages 1–4, September 2020. doi: 10.22489/CinC.2020.179.

[25] Jukka-Pekka Sirkiä, Tuukka Panula, and Matti Kaisti. The Effects of External Pressure on Multi-Wavelength Photoplethysmography Signals. In *2021 Computing in Cardiology (CinC)*, volume 48, pages 1–4, September 2021. doi: 10.23919/CinC53138.2021.9662771.

[26] Jing Liu, Shirong Qiu, Ningqi Luo, Sze-Kei Lau, Hui Yu, Timothy Kwok, Yuan-Ting Zhang, and Ni Zhao. PCA-Based Multi-Wavelength Photoplethysmography Algorithm for Cuffless Blood Pressure Measurement on Elderly Subjects. *IEEE Journal of Biomedical and Health Informatics*, 25(3):663–673, March 2021. ISSN 2168-2208. doi: 10.1109/JBHI.2020.3004032.

[27] Subhasri Chatterjee, Karthik Budidha, and Panayiotis A. Kyriacou. Investigating the origin of photoplethysmography using a multiwavelength Monte Carlo model. *Physiological Measurement*, 41(8):084001, September 2020. ISSN 0967-3334. doi: 10.1088/1361-6579/aba008.

[28] Stephane Laurent, Claudia Agabiti-Rosei, Rosa Maria Bruno, and Damiano Rizzoni. Microcirculation and Macrocirculation in Hypertension: A Dangerous Cross-Link? *Hypertension*, 79(3): 479–490, March 2022. doi: 10.1161/HYPERTENSIONAHA.121.17962.

[29] Marcin Hellmann, Matthieu Roustit, and Jean-Luc Cracowski. Skin microvascular endothelial function as a biomarker in cardiovascular diseases? *Pharmacological Reports*, 67, May 2015. doi: 10.1016/j.pharep.2015.05.008.

[30] Toshiyo Tamura, Yuka Maeda, Masaki Sekine, and Masaki Yoshida. Wearable Photoplethysmographic Sensors—Past and Present. *Electronics*, 3(2):282–302, June 2014. ISSN 2079-9292. doi: 10.3390/electronics3020282.

[31] Peter H. Charlton, Panicos A. Kyriacou, Jonathan Mant, Vaidotas Marozas, Phil Chowienczyk, and Jordi Alastruey. Wearable Photoplethysmography for Cardiovascular Monitoring. *Proceedings of the IEEE*, 110(3):355–381, March 2022. ISSN 1558-2256. doi: 10.1109/JPROC.2022.3149785.

[32] Richard J. Chen, Ming Y. Lu, Tiffany Y. Chen, Drew F. K. Williamson, and Faisal Mahmood. Synthetic data in machine learning for medicine and healthcare. *Nature Biomedical Engineering*, 5(6):493–497, June 2021. ISSN 2157-846X. doi: 10.1038/s41551-021-00751-8.

[33] Jean-Francois Rajotte, Robert Bergen, David L. Buckeridge, Khaled El Emam, Raymond Ng, and Elissa Strome. Synthetic data as an enabler for machine learning applications in medicine. *iScience*, 25(11):105331, November 2022. ISSN 2589-0042. doi: 10.1016/j.isci.2022.105331.

[34] Ehrhardt Proksch, Johanna M. Brandner, and Jens-Michael Jensen. The skin: An indispensable barrier. *Experimental Dermatology*, 17(12):1063–1072, 2008. ISSN 1600-0625. doi: 10.1111/j.1600-0625.2008.00786.x.

[35] Marjorie F. Yang, Valery V. Tuchin, and Anna N. Yaroslavsky. Principles of Light-Skin Interactions. In Elma Baron, editor, *Light-Based Therapies for Skin of Color*, pages 1–44. Springer, London, 2009. ISBN 978-1-84882-328-0. doi: 10.1007/978-1-84882-328-0_1.

[36] H. Fruhstorfer, U. Abel, C.-D. Garthe, and A. Knüttel. Thickness of the stratum corneum of the volar fingertips. *Clinical Anatomy*, 13(6):429–433, 2000. ISSN 1098-2353. doi: 10.1002/1098-2353(2000)13:6<429::AID-CA6>3.0.CO;2-5.

[37] Daiwei Li, Lucas Humayun, Emelina Vienneau, Tri Vu, and Junjie Yao. Seeing through the Skin: Photoacoustic Tomography of Skin Vasculature and Beyond. *JID Innovations*, 1(3):100039, September 2021. ISSN 2667-0267. doi: 10.1016/j.xjidi.2021.100039.

[38] Jean-Luc Cracowski and Matthieu Roustit. Human Skin Microcirculation. *Comprehensive Physiology*, 10:1105–1154, July 2020. ISSN 9780470650714. doi: 10.1002/cphy.c190008.

[39] Lars Walløe. Arterio-venous anastomoses in the human skin and their role in temperature control. *Temperature: Multidisciplinary Biomedical Journal*, 3(1):92–103, October 2015. ISSN 2332-8940. doi: 10.1080/23328940.2015.1088502.

[40] Goksel Guven, Matthias P. Hilty, and Can Ince. Microcirculation: Physiology, Pathophysiology, and Clinical Application. *Blood Purification*, 49(1-2):143–150, December 2019. ISSN 0253-5068. doi: 10.1159/000503775.

[41] Aleksander S. Popel and Paul C. Johnson. Microcirculation and Hemorheology. *Annual Review of Fluid Mechanics*, 37(1):43–69, 2005. doi: 10.1146/annurev.fluid.37.042604.133933.

[42] S. A. Williams, S. Wasserman, D. W. Rawlinson, R. I. Kitney, L. H. Smaje, and J. E. Tooke. Dynamic measurement of human capillary blood pressure. *Clinical Science*, 74(5):507–512, May 1988. ISSN 0143-5221. doi: 10.1042/cs0740507.

[43] A. C. Shore, D. D. Sandeman, and J. E. Tooke. Capillary pressure, pulse pressure amplitude, and pressure waveform in healthy volunteers. *American Journal of Physiology-Heart and Circulatory Physiology*, 268(1):H147–H154, January 1995. ISSN 0363-6135. doi: 10.1152/ajpheart.1995.268.1.H147.

[44] Angela C. Shore. Capillaroscopy and the measurement of capillary pressure. *British Journal of Clinical Pharmacology*, 50(6):501–513, 2000. ISSN 1365-2125. doi: 10.1046/j.1365-2125.2000.00278.x.

[45] Martin Hahn, Thomas Klyscz, and Michael Jünger. Synchronous Measurements of Blood Pressure and Red Blood Cell Velocity in Capillaries of Human Skin. *Journal of Investigative Dermatology*, 106(6):1256–1259, June 1996. ISSN 0022-202X. doi: 10.1111/1523-1747.ep12348955.

[46] Steven Lammers, Devon Scott, Kendall Hunter, Wei Tan, Robin Shandas, and Kurt R. Stenmark. Mechanics and Function of the Pulmonary Vasculature: Implications for Pulmonary Vascular Disease and Right Ventricular Function. In *Comprehensive Physiology*, pages 295–319. John Wiley & Sons, Ltd, 2012. ISBN 978-0-470-65071-4. doi: 10.1002/cphy.c100070.

[47] David D. Gutterman, Dawid S. Chabowski, Andrew O. Kadlec, Matthew J. Durand, Julie K. Freed, Karima Ait-Aissa, and Andreas M. Beyer. The Human Microcirculation. *Circulation Research*, 118(1):157–172, January 2016. doi: 10.1161/CIRCRESAHA.115.305364.

[48] R. G. IJzerman, R. T. De Jongh, M. a. M. Beijk, M. M. Van Weissenbruch, H. A. Delemarre-van de Waal, E. H. Serné, and C. D. A. Stehouwer. Individuals at increased coronary heart disease risk are characterized by an impaired microvascular function in skin. *European Journal of Clinical Investigation*, 33(7):536–542, 2003. ISSN 1365-2362. doi: 10.1046/j.1365-2362.2003.01179.x.

[49] A. Kruger, J. Stewart, R. Sahityani, E. O'Riordan, C. Thompson, S. Adler, R. Garrick, P. Vallance, and M. S. Goligorsky. Laser Doppler flowmetry detection of endothelial dysfunction in end-stage renal disease patients: Correlation with cardiovascular risk. *Kidney International*, 70 (1):157–164, July 2006. ISSN 0085-2538. doi: 10.1038/sj.ki.5001511.

[50] R. Yamamoto-Suganuma and Y. Aso. Relationship between post-occlusive forearm skin reactive hyperaemia and vascular disease in patients with Type 2 diabetes—a novel index for detecting micro- and macrovascular dysfunction using laser Doppler flowmetry. *Diabetic Medicine*, 26(1): 83–88, 2009. ISSN 1464-5491. doi: 10.1111/j.1464-5491.2008.02609.x.

[51] Sharad C. Agarwal, John Allen, Alan Murray, and Ian F. Purcell. Laser Doppler assessment of dermal circulatory changes in people with coronary artery disease. *Microvascular Research*, 84 (1):55–59, July 2012. ISSN 0026-2862. doi: 10.1016/j.mvr.2012.02.002.

[52] Elaine G. Souza, Andrea De Lorenzo, Grazielle Huguenin, Glaucia M. M. Oliveira, and Eduardo Tibiriçá. Impairment of systemic microvascular endothelial and smooth muscle function in individuals with early-onset coronary artery disease: Studies with laser speckle contrast imaging. *Coronary Artery Disease*, 25(1):23, January 2014. ISSN 0954-6928. doi: 10.1097/MCA.0000000000000055.

[53] P A Carberry, A M Shepherd, and J M Johnson. Resting and maximal forearm skin blood flows are reduced in hypertension. *Hypertension*, 20(3):349–355, September 1992. doi: 10.1161/01.HYP.20.3.349.

[54] Marco Rossi, Adam Bradbury, Armando Magagna, Margherita Pesce, Stefano Taddei, and Aneta Stefanovska. Investigation of skin vasoreactivity and blood flow oscillations in hypertensive patients: Effect of short-term antihypertensive treatment. *Journal of Hypertension*, 29(8):1569, August 2011. ISSN 0263-6352. doi: 10.1097/HJH.0b013e328348b653.

[55] Erik H. Serné, Reinold O.B. Gans, Jan C. ter Maaten, Geert-Jan Tangelder, Ab J.M. Donker, and Coen D.A. Stehouwer. Impaired Skin Capillary Recruitment in Essential Hypertension Is Caused by Both Functional and Structural Capillary Rarefaction. *Hypertension*, 38(2):238–242, August 2001. doi: 10.1161/01.HYP.38.2.238.

[56] Lacy A. Holowatz, Caitlin S. Thompson-Torgerson, and W. Larry Kenney. The human cutaneous circulation as a model of generalized microvascular function. *Journal of Applied Physiology*, 105 (1):370–372, July 2008. ISSN 8750-7587. doi: 10.1152/japplphysiol.00858.2007.

[57] Evan Austin, Amaris N. Geisler, Julie Nguyen, Indermeet Kohli, Iltefat Hamzavi, Henry W. Lim, and Jared Jagdeo. Visible light. Part I: Properties and cutaneous effects of visible light. *Journal of the American Academy of Dermatology*, 84(5):1219–1231, May 2021. ISSN 0190-9622. doi: 10.1016/j.jaad.2021.02.048.

[58] Tom Lister, Philip A. Wright, and Paul H. Chappell. Optical properties of human skin. *Journal*

of Biomedical Optics, 17(9):090901, September 2012. ISSN 1083-3668, 1560-2281. doi: 10.1117/1.JBO.17.9.090901.

[59] C. Mignon, D. J. Tobin, M. Zeitouny, and N. E. Uzunbajakava. Shedding light on the variability of optical skin properties: Finding a path towards more accurate prediction of light propagation in human cutaneous compartments. *Biomedical Optics Express*, 9(2):852–872, February 2018. ISSN 2156-7085. doi: 10.1364/BOE.9.000852.

[60] Steven Jacques. Melanosome Absorption Coefficient. https://omlc.org/spectra/melanin/mua.html.

[61] Scott Prahl. Optical Absorption of Water Compendium. https://omlc.org/spectra/water/abs/index.html, .

[62] Scott Prahl. Optical Absorption of Hemoglobin. https://omlc.org/spectra/hemoglobin/, .

[63] R.L.P. van Veen, H.J.C.M. Sterenborg, A. Pifferi, A. Torricelli, and R. Cubeddu. Optical Absorption of Fat. https://omlc.org/spectra/fat/.

[64] Wesley B. Baker, Ashwin B. Parthasarathy, David R. Busch, Rickson C. Mesquita, Joel H. Greenberg, and A. G. Yodh. Modified Beer-Lambert law for blood flow. *Biomedical Optics Express*, 5(11):4053–4075, November 2014. ISSN 2156-7085. doi: 10.1364/BOE.5.004053.

[65] Ilze Oshina and Janis Spigulis. Beer–Lambert law for optical tissue diagnostics: Current state of the art and the main limitations. *Journal of Biomedical Optics*, 26(10):100901, October 2021. ISSN 1083-3668, 1560-2281. doi: 10.1117/1.JBO.26.10.100901.

[66] D T Delpy, M Cope, P Van Der Zee, S Arridge, S Wray, and J Wyatt. Estimation of optical pathlength through tissue from direct time of flight measurement. *Physics in Medicine and Biology*, 33(12):1433–1442, December 1988. ISSN 0031-9155, 1361-6560. doi: 10.1088/0031-9155/33/12/008.

[67] Angelo Sassaroli and Sergio Fantini. Comment on the modified Beer–Lambert law for scattering media. *Physics in Medicine & Biology*, 49(14):N255, July 2004. ISSN 0031-9155. doi: 10.1088/0031-9155/49/14/N07.

[68] S. R. Arridge, M. Cope, and D. T. Delpy. The theoretical basis for the determination of optical pathlengths in tissue: Temporal and frequency analysis. *Physics in Medicine & Biology*, 37(7):1531, July 1992. ISSN 0031-9155. doi: 10.1088/0031-9155/37/7/005.

[69] Matthias Kohl, Christian Nolte, Hauke R. Heekeren, Susanne Horst, Udo Scholz, Hellmuth Obrig, and Arno Villringer. Determination of the wavelength dependence of the differential pathlength factor from near-infrared pulse signals. *Physics in Medicine & Biology*, 43(6):1771, June 1998. ISSN 0031-9155. doi: 10.1088/0031-9155/43/6/028.

[70] Scott Prahl, M. Keijzer, Steven Jacques, and A. Welch. A Monte Carlo Model of Light Propagation in Tissue. *SPIE Inst. Ser. IS*, 5, January 1989.

[71] Lihong Wang, Steven L. Jacques, and Liqiong Zheng. MCML—Monte Carlo modeling of light transport in multi-layered tissues. *Computer Methods and Programs in Biomedicine*, 47(2):131–146, July 1995. ISSN 0169-2607. doi: 10.1016/0169-2607(95)01640-F.

[72] T.J. Pfefer, J. Kehlet Barton, E.K. Chan, M.G. Ducros, B.S. Sorg, T.E. Milner, J.S. Nelson, and A.J. Welch. A three-dimensional modular adaptable grid numerical model for light propagation during laser irradiation of skin tissue. *IEEE Journal of Selected Topics in Quantum Electronics*, 2(4):934–942, December 1996. ISSN 1558-4542. doi: 10.1109/2944.577318.

[73] Steven L. Jacques. Tutorial on Monte Carlo simulation of photon transport in biological tissues [Invited]. *Biomedical Optics Express*, 14(2):559–576, February 2023. ISSN 2156-7085. doi: 10.1364/BOE.477237.

[74] José Francisco Algorri, Mario Ochoa, Pablo Roldán-Varona, Luís Rodríguez-Cobo, and José Miguel López-Higuera. Light Technology for Efficient and Effective Photodynamic Therapy: A Critical Review. *Cancers*, 13(14):3484, January 2021. ISSN 2072-6694. doi: 10.3390/cancers13143484.

[75] Steven Jacques. Simple Theory, Measurements, And Rules Of Thumb For Dosimetry During Photodynamic Therapy. *Proceedings of SPIE - The International Society for Optical Engineering*, 1065:100, May 1989. doi: 10.1117/12.978009.

[76] Junyung Park, Hyeon Seok Seok, Sang-Su Kim, and Hangsik Shin. Photoplethysmogram Analysis and Applications: An Integrative Review. *Frontiers in Physiology*, 12, 2022. ISSN 1664-042X.

[77] Elisa Mejía-Mejía, John Allen, Karthik Budidha, Chadi El-Hajj, Panicos A. Kyriacou, and Peter H. Charlton. Photoplethysmography signal processing and synthesis. In *Photoplethysmography*, pages 69–146. Elsevier, 2022. ISBN 978-0-12-823374-0. doi: 10.1016/B978-0-12-823374-0.00015-3.

[78] Maxime Coutrot, Emmanuel Dudoignon, Jona Joachim, Etienne Gayat, Fabrice Vallée, and François Dépret. Perfusion index: Physical principles, physiological meanings and clinical implications in anaesthesia and critical care. *Anaesthesia Critical Care & Pain Medicine*, 40(6): 100964, December 2021. ISSN 2352-5568. doi: 10.1016/j.accpm.2021.100964.

[79] Mohamed Elgendi. On the Analysis of Fingertip Photoplethysmogram Signals. *Current Cardiology Reviews*, 8(1):14–25, February 2012. ISSN 1573-403X. doi: 10.2174/157340312801215782.

[80] Irene García-López and Esther Rodriguez-Villegas. Extracting the Jugular Venous Pulse from Anterior Neck Contact Photoplethysmography. *Scientific Reports*, 10(1):3466, February 2020. ISSN 2045-2322. doi: 10.1038/s41598-020-60317-7.

[81] Jing Liu, Yuan-Ting Zhang, Xiao-Rong Ding, Wen-Xuan Dai, and Ni Zhao. A preliminary study on multi-wavelength PPG based pulse transit time detection for cuffless blood pressure measurement. In *2016 38th Annual International Conference of the IEEE Engineering in Medicine and Biology Society (EMBC)*, pages 615–618, August 2016. doi: 10.1109/EMBC.2016.7590777.

[82] M. Sandberg, Q. Zhang, J. Styf, B. Gerdle, and L.-G. Lindberg. Non-invasive monitoring of muscle blood perfusion by photoplethysmography: Evaluation of a new application. *Acta Physiologica Scandinavica*, 183(4):335–343, 2005. ISSN 1365-201X. doi: 10.1111/j.1365-201X.2005.01412.x.

[83] Shifat Hossain, Chowdhury Azimul Haque, and Ki-Doo Kim. Quantitative Analysis of Different Multi-Wavelength PPG Devices and Methods for Noninvasive In-Vivo Estimation of Glycated Hemoglobin. *Applied Sciences*, 11(15):6867, January 2021. ISSN 2076-3417. doi: 10.3390/app11156867.

[84] Liangwen Yan, Sijung Hu, Abdullah Alzahrani, Samah Alharbi, and Panagiotis Blanos. A Multi-Wavelength Opto-Electronic Patch Sensor to Effectively Detect Physiological Changes against Human Skin Types. *Biosensors*, 7(2):22, June 2017. ISSN 2079-6374. doi: 10.3390/bios7020022.

[85] Jing Liu, Bryan Yan, Shih-Chi Chen, Yuan-Ting Zhang, Charles Sodini, and Ni Zhao. Non-Invasive Capillary Blood Pressure Measurement Enabling Early Detection and Classification of Venous Congestion. *IEEE Journal of Biomedical and Health Informatics*, 25(8):2877–2886, August 2021. ISSN 2168-2208. doi: 10.1109/JBHI.2021.3055760.

[86] Jukka-Pekka Sirkiä, Tuukka Panula, and Matti Kaisti. Tonometric Multi-Wavelength Photoplethysmography for Studying the Cutaneous Microvasculature of the Fingertip. *IEEE Transactions on Instrumentation and Measurement*, 72:1–13, 2023. ISSN 1557-9662. doi: 10.1109/TIM.2023.3293873.

[87] Jukka-Pekka Sirkiä, Tuukka Panula, and Matti Kaisti. Non-Invasive Hemodynamic Monitoring System Integrating Spectrometry, Photoplethysmography, and Arterial Pressure Measurement Capabilities. *Advanced Science*, 11(24):2310022, 2024. ISSN 2198-3844. doi: 10.1002/advs.202310022.

[88] Shao-Hao Chen, Yung-Chi Chuang, and Cheng-Chun Chang. Development of a Portable All-Wavelength PPG Sensing Device for Robust Adaptive-Depth Measurement: A Spectrometer Approach with a Hydrostatic Measurement Example. *Sensors*, 20(22):6556, January 2020. ISSN 1424-8220. doi: 10.3390/s20226556.

[89] Ali Al-Naji, Kim Gibson, Sang-Heon Lee, and Javaan Chahl. Monitoring of Cardiorespiratory Signal: Principles of Remote Measurements and Review of Methods. *IEEE Access*, 5:15776–15790, 2017. ISSN 2169-3536. doi: 10.1109/ACCESS.2017.2735419.

[90] Smera Premkumar and Duraisamy Jude Hemanth. Intelligent Remote Photoplethysmography-Based Methods for Heart Rate Estimation from Face Videos: A Survey. *Informatics*, 9(3):57, September 2022. ISSN 2227-9709. doi: 10.3390/informatics9030057.

[91] Po-Wei Huang, Bing-Jhang Wu, and Bing-Fei Wu. A Heart Rate Monitoring Framework for Real-World Drivers Using Remote Photoplethysmography. *IEEE Journal of Biomedical and Health Informatics*, 25(5):1397–1408, May 2021. ISSN 2168-2208. doi: 10.1109/JBHI.2020.3026481.

[92] Juan-Carlos Cobos-Torres, Mohamed Abderrahim, and José Martínez-Orgado. Non-Contact, Simple Neonatal Monitoring by Photoplethysmography. *Sensors*, 18(12):4362, December 2018. ISSN 1424-8220. doi: 10.3390/s18124362.

[93] Sebastian Zaunseder, Alexander Trumpp, Daniel Wedekind, and Hagen Malberg. Cardiovascular assessment by imaging photoplethysmography – a review. *Biomedical Engineering / Biomedizinische Technik*, 63(5):617–634, October 2018. ISSN 1862-278X. doi: 10.1515/bmt-2017-0119.

[94] Daniel McDuff, Sarah Gontarek, and Rosalind W. Picard. Improvements in Remote Cardiopulmonary Measurement Using a Five Band Digital Camera. *IEEE Transactions on Biomedical Engineering*, 61(10):2593–2601, October 2014. ISSN 1558-2531. doi: 10.1109/TBME.2014.2323695.

[95] Mark van Gastel, Sander Stuijk, and Gerard de Haan. Motion Robust Remote-PPG in Infrared. *IEEE Transactions on Biomedical Engineering*, 62(5):1425–1433, May 2015. ISSN 1558-2531. doi: 10.1109/TBME.2015.2390261.

[96] Philipp V. Rouast, Marc T. P. Adam, Raymond Chiong, David Cornforth, and Ewa Lux. Remote heart rate measurement using low-cost RGB face video: A technical literature review. *Frontiers of Computer Science*, 12(5):858–872, October 2018. ISSN 2095-2236. doi: 10.1007/s11704-016-6243-6.

[97] Melissa Joanne Bautista, Mikolaj Kowal, Daniel G. W. Cave, Candice Downey, and David G. Jayne. Clinical applications of contactless photoplethysmography for monitoring in adults: A systematic review and meta-analysis. *Journal of Clinical and Translational Science*, 7(1):e129, January 2023. ISSN 2059-8661. doi: 10.1017/cts.2023.547.

[98] Coen Arrow, Max Ward, Jason Eshraghian, and Girish Dwivedi. Capturing the pulse: A state-of-the-art review on camera-based jugular vein assessment. *Biomedical Optics Express*, 14(12):6470–6492, December 2023. ISSN 2156-7085. doi: 10.1364/BOE.507418.

[99] Andreia Moço and Wim Verkruysse. Pulse oximetry based on photoplethysmography imaging with red and green light. *Journal of Clinical Monitoring and Computing*, 35(1):123–133, February 2021. ISSN 1573-2614. doi: 10.1007/s10877-019-00449-y.

[100] James Jordon, Lukasz Szpruch, Florimond Houssiau, Mirko Bottarelli, Giovanni Cherubin, Carsten Maple, Samuel N. Cohen, and Adrian Weller. Synthetic Data – what, why and how?, May 2022.

[101] Lu Wang, Lisheng Xu, Shuting Feng, Max Q. H. Meng, and Kuanquan Wang. Multi-Gaussian fitting for pulse waveform using Weighted Least Squares and multi-criteria decision making method. *Computers in Biology and Medicine*, 43(11):1661–1672, November 2013. ISSN 0010-4825. doi: 10.1016/j.compbiomed.2013.08.004.

[102] Diego Martín-Martínez, Pablo Casaseca-de-la-Higuera, Marcos Martín-Fernández, and Carlos Alberola-López. Stochastic Modeling of the PPG Signal: A Synthesis-by-Analysis Approach With Applications. *IEEE Transactions on Biomedical Engineering*, 60(9):2432–2441, September 2013. ISSN 1558-2531. doi: 10.1109/TBME.2013.2257770.

[103] Qunfeng Tang, Zhencheng Chen, Rabab Ward, and Mohamed Elgendi. Synthetic photoplethysmogram generation using two Gaussian functions. *Scientific Reports*, 10(1):13883, August 2020. ISSN 2045-2322. doi: 10.1038/s41598-020-69076-x.

[104] Andrius Sološenko, Andrius Petrėnas, Vaidotas Marozas, and Leif Sörnmo. Modeling of the photoplethysmogram during atrial fibrillation. *Computers in Biology and Medicine*, 81:130–138, February 2017. ISSN 0010-4825. doi: 10.1016/j.compbiomed.2016.12.016.

[105] Oishee Mazumder, Rohan Banerjee, Dibyendu Roy, Sakyajit Bhattacharya, Avik Ghose, and Aniruddha Sinha. Synthetic PPG Signal Generation to Improve Coronary Artery Disease Classification: Study With Physical Model of Cardiovascular System. *IEEE Journal of Biomedical and Health Informatics*, 26(5):2136–2146, May 2022. ISSN 2168-2208. doi: 10.1109/JBHI.2022.3147383.

[106] Dani Kiyasseh, Girmaw Abebe Tadesse, Le Nguyen Thanh Nhan, Le Van Tan, Louise Thwaites, Tingting Zhu, and David Clifton. PlethAugment: GAN-Based PPG Augmentation for Medical Diagnosis in Low-Resource Settings. *IEEE Journal of Biomedical and Health Informatics*, 24 (11):3226–3235, November 2020. ISSN 2168-2208. doi: 10.1109/JBHI.2020.2979608.

[107] Siana Jones, Scott T. Chiesa, Nishi Chaturvedi, and Alun D. Hughes. Recent developments in near-infrared spectroscopy (NIRS) for the assessment of local skeletal muscle microvascular function and capacity to utilise oxygen. *Artery Research*, 16:25–33, December 2016. ISSN 1872-9312. doi: 10.1016/j.artres.2016.09.001.

[108] Felix Scholkmann, Stefan Kleiser, Andreas Jaakko Metz, Raphael Zimmermann, Juan Mata Pavia, Ursula Wolf, and Martin Wolf. A review on continuous wave functional near-infrared spectroscopy and imaging instrumentation and methodology. *NeuroImage*, 85:6–27, January 2014. ISSN 1053-8119. doi: 10.1016/j.neuroimage.2013.05.004.

[109] Adelina Pellicer and María del Carmen Bravo. Near-infrared spectroscopy: A methodology-focused review. *Seminars in Fetal and Neonatal Medicine*, 16(1):42–49, February 2011. ISSN 1744-165X. doi: 10.1016/j.siny.2010.05.003.

[110] Paola Pinti, Ilias Tachtsidis, Antonia Hamilton, Joy Hirsch, Clarisse Aichelburg, Sam Gilbert, and Paul W. Burgess. The present and future use of functional near-infrared spectroscopy (fNIRS) for cognitive neuroscience. *Annals of the New York Academy of Sciences*, 1464(1): 5–29, 2020. ISSN 1749-6632. doi: 10.1111/nyas.13948.

[111] Abele Donati, Elisa Damiani, Roberta Domizi, Claudia Scorcella, Andrea Carsetti, Stefania Tondi, Valentina Monaldi, Erica Adrario, Rocco Romano, Paolo Pelaia, and Mervyn Singer. Near-infrared spectroscopy for assessing tissue oxygenation and microvascular reactivity in critically ill patients: A prospective observational study. *Critical Care*, 20:311, October 2016. ISSN 1364-8535. doi: 10.1186/s13054-016-1500-5.

[112] Takafumi Hamaoka and Kevin K. McCully. Review of early development of near-infrared spectroscopy and recent advancement of studies on muscle oxygenation and oxidative metabolism. *The Journal of Physiological Sciences*, 69(6):799–811, November 2019. ISSN 1880-6562. doi: 10.1007/s12576-019-00697-2.

[113] Turgut Durduran and Arjun G. Yodh. Diffuse correlation spectroscopy for non-invasive, microvascular cerebral blood flow measurement. *NeuroImage*, 85:51–63, January 2014. ISSN 1053-8119. doi: 10.1016/j.neuroimage.2013.06.017.

[114] Stefan A. Carp, Davide Tamborini, Dibbyan Mazumder, Kuan-Cheng Wu, Mitchell B. Robinson, Kimberly A. Stephens, Oleg Shatrovoy, Niyom Lue, Nisan Ozana, Megan H. Blackwell, and Maria Angela Franceschini. Diffuse correlation spectroscopy measurements of blood flow using 1064 nm light. *Journal of Biomedical Optics*, 25(9):097003, September 2020. ISSN 1083-3668, 1560-2281. doi: 10.1117/1.JBO.25.9.097003.

[115] Edward James and Peter R. T. Munro. Diffuse Correlation Spectroscopy: A Review of Recent Advances in Parallelisation and Depth Discrimination Techniques. *Sensors*, 23(23):9338, January 2023. ISSN 1424-8220. doi: 10.3390/s23239338.

[116] T. Durduran, R. Choe, W. B. Baker, and A. G. Yodh. Diffuse optics for tissue monitoring and tomography. *Reports on Progress in Physics*, 73(7):076701, June 2010. ISSN 0034-4885. doi: 10.1088/0034-4885/73/7/076701.

[117] Yu Shang, Ting Li, and Guoqiang Yu. Clinical applications of near-infrared diffuse correlation spectroscopy and tomography for tissue blood flow monitoring and imaging. *Physiological Measurement*, 38(4):R1, March 2017. ISSN 0967-3334. doi: 10.1088/1361-6579/aa60b7.

[118] Jonghee Yoon. Hyperspectral Imaging for Clinical Applications. *BioChip Journal*, 16(1):1–12, March 2022. ISSN 2092-7843. doi: 10.1007/s13206-021-00041-0.

[119] 1st Lt. Pushkar Aggarwal and Francis A. Papay. Applications of multispectral and hyperspectral imaging in dermatology. *Experimental Dermatology*, 31(8):1128–1135, 2022. ISSN 1600-0625. doi: 10.1111/exd.14624.

[120] Mihaela Antonina Calin, Sorin Viorel Parasca, Dan Savastru, and Dragos Manea. Hyperspectral Imaging in the Medical Field: Present and Future. *Applied Spectroscopy Reviews*, 49(6):435–447, August 2014. ISSN 0570-4928. doi: 10.1080/05704928.2013.838678.

[121] Baowei Fei. Chapter 3.6 - Hyperspectral imaging in medical applications. In José Manuel Amigo, editor, *Data Handling in Science and Technology*, volume 32 of *Hyperspectral Imaging*, pages 523–565. Elsevier, January 2019. doi: 10.1016/B978-0-444-63977-6.00021-3.

[122] Ingemar Fredriksson, Marcus Larsson, and Tomas Strömberg. Measurement depth and volume in laser Doppler flowmetry. *Microvascular Research*, 78(1):4–13, June 2009. ISSN 0026-2862. doi: 10.1016/j.mvr.2009.02.008.

[123] A. M. Seifalian, G. Stansby, A. Jackson, K. Howell, and G. Hamilton. Comparison of laser doppler perfusion imaging, laser doppler flowmetry, and thermographic imaging for assessment of blood flow in human skin. *European Journal of Vascular Surgery*, 8(1):65–69, January 1994. ISSN 0950-821X. doi: 10.1016/S0950-821X(05)80123-9.

[124] Matthieu Roustit and Jean-Luc Cracowski. Assessment of endothelial and neurovascular function in human skin microcirculation. *Trends in pharmacological sciences*, 34, June 2013. doi: 10.1016/j.tips.2013.05.007.

[125] Janaka Senarathna, Abhishek Rege, Nan Li, and Nitish V. Thakor. Laser Speckle Contrast Imaging: Theory, Instrumentation and Applications. *IEEE Reviews in Biomedical Engineering*, 6: 99–110, 2013. ISSN 1937-3333, 1941-1189. doi: 10.1109/RBME.2013.2243140.

[126] David Briers, Donald D. Duncan, Evan R. Hirst, Sean J. Kirkpatrick, Marcus Larsson, Wiendelt Steenbergen, Tomas Stromberg, and Oliver B. Thompson. Laser speckle contrast imaging: Theoretical and practical limitations. *Journal of Biomedical Optics*, 18(6):066018, June 2013. ISSN 1083-3668, 1560-2281. doi: 10.1117/1.JBO.18.6.066018.

[127] Matthijs Draijer, Erwin Hondebrink, Ton van Leeuwen, and Wiendelt Steenbergen. Review of laser speckle contrast techniques for visualizing tissue perfusion. *Lasers in Medical Science*, 24 (4):639–651, July 2009. ISSN 1435-604X. doi: 10.1007/s10103-008-0626-3.

[128] Anton Sdobnov, Gennadii Piavchenko, Alexander Bykov, and Igor Meglinski. Advances in Dynamic Light Scattering Imaging of Blood Flow. *Laser & Photonics Reviews*, 18(2):2300494, 2024. ISSN 1863-8899. doi: 10.1002/lpor.202300494.

[129] Wido Heeman, Wiendelt Steenbergen, Gooitzen M. van Dam, and E. Christiaan Boerma. Clinical applications of laser speckle contrast imaging: A review. *Journal of Biomedical Optics*, 24 (8):080901, August 2019. ISSN 1083-3668, 1560-2281. doi: 10.1117/1.JBO.24.8.080901.

[130] Jorge Herranz Olazabal, Ilde Lorato, Jesse Kling, Marc Verhoeven, Fokko Wieringa, Chris Van Hoof, Willem Verkruijsse, and Evelien Hermeling. Comparison between Speckle Plethysmography and Photoplethysmography during Cold Pressor Test Referenced to Finger Arterial Pressure. *Sensors*, 23(11):5016, January 2023. ISSN 1424-8220. doi: 10.3390/s23115016.

[131] Amalina Binte Ebrahim Attia, Ghayathri Balasundaram, Mohesh Moothanchery, U. S. Dinish, Renzhe Bi, Vasilis Ntziachristos, and Malini Olivo. A review of clinical photoacoustic imaging: Current and future trends. *Photoacoustics*, 16:100144, December 2019. ISSN 2213-5979. doi: 10.1016/j.pacs.2019.100144.

[132] Xosé Luís Deán-Ben and Daniel Razansky. Optoacoustic imaging of the skin. *Experimental Dermatology*, 30(11):1598–1609, 2021. ISSN 1600-0625. doi: 10.1111/exd.14386.

[133] Mengyang Liu and Wolfgang Drexler. Optical coherence tomography angiography and photoacoustic imaging in dermatology. *Photochemical & Photobiological Sciences*, 18(5):945–962, May 2019. ISSN 1474-905X, 1474-9092. doi: 10.1039/c8pp00471d.

[134] Terese von Knorring and Mette Mogensen. Photoacoustic tomography for assessment and quantification of cutaneous and metastatic malignant melanoma - A systematic review. *Photodiagnosis and Photodynamic Therapy*, 33:102095, March 2021. ISSN 1572-1000. doi: 10.1016/j.pdpdt.2020.102095.

[135] Yue Ying, Hong Zhang, and Li Lin. Photoacoustic Imaging of Human Skin for Accurate Diagnosis and Treatment Guidance. *Optics*, 5(1):133–150, March 2024. ISSN 2673-3269. doi: 10.3390/opt5010010.

[136] James G Fujimoto, Costas Pitris, Stephen A Boppart, and Mark E Brezinski. Optical Coherence Tomography: An Emerging Technology for Biomedical Imaging and Optical Biopsy. *Neoplasia (New York, N.Y.)*, 2(1-2):9–25, January 2000. ISSN 1522-8002.

[137] D. Thomas and G. Duguid. Optical coherence tomography—a review of the principles and contemporary uses in retinal investigation. *Eye*, 18(6):561–570, June 2004. ISSN 1476-5454. doi: 10.1038/sj.eye.6700729.

[138] B.E. Bouma, J.F. de Boer, D. Huang, I.K. Jang, T. Yonetsu, C.L. Leggett, R. Leitgeb, D.D. Sampson, M. Suter, B. Vakoc, M. Villiger, and M. Wojtkowski. Optical coherence tomography. *Nature reviews. Methods primers*, 2:79, 2022. ISSN 2662-8449. doi: 10.1038/s43586-022-00162-2.

[139] Kornelia Schuetzenberger, Martin Pfister, Alina Messner, Vanessa Froehlich, Gerhard Garhoefer, Christine Hohenadl, Leopold Schmetterer, and René M. Werkmeister. Comparison of optical coherence tomography and high frequency ultrasound imaging in mice for the assessment of skin morphology and intradermal volumes. *Scientific Reports*, 9(1):13643, September 2019. ISSN 2045-2322. doi: 10.1038/s41598-019-50104-4.

[140] Matthieu Roustit and Jean-Luc Cracowski. Non-invasive Assessment of Skin Microvascular Function in Humans: An Insight Into Methods. *Microcirculation*, 19(1):47–64, 2012. ISSN 1549-8719. doi: 10.1111/j.1549-8719.2011.00129.x.

[141] Vanessa Smith, Ariane L. Herrick, Francesca Ingegnoli, Nemanja Damjanov, Rossella De Angelis, Christopher P. Denton, Oliver Distler, Karinna Espejo, Ivan Foeldvari, Tracy Frech, Boris Garro, Marwin Gutierrez, Genevieve Gyger, Eric Hachulla, Roger Hesselstrand, Annamaria Iagnocco, Cristiane Kayser, Karin Melsens, Ulf Müller-Ladner, Sabrina Paolino, Carmen Pizzorni, Mislav Radic, Valeria Riccieri, Marcus Snow, Wendy Stevens, Alberto Sulli, Jacob M. van Laar, Madelon C. Vonk, Amber Vanhaecke, and Maurizio Cutolo. Standardisation of nailfold capillaroscopy for the assessment of patients with Raynaud's phenomenon and systemic sclerosis. *Autoimmunity Reviews*, 19(3):102458, March 2020. ISSN 1568-9972. doi: 10.1016/j.autrev.2020.102458.

[142] Zahra Emrani, Abdolamir Karbalaie, Alimohammad Fatemi, Mahnaz Etehadtavakol, and Björn-Erik Erlandsson. Capillary density: An important parameter in nailfold capillaroscopy. *Microvascular Research*, 109:7–18, January 2017. ISSN 0026-2862. doi: 10.1016/j.mvr.2016.09.001.

[143] Warren Groner, James W. Winkelman, Anthony G. Harris, Can Ince, Gerrit J. Bouma, Konrad Messmer, and Richard G. Nadeau. Orthogonal polarization spectral imaging: A new method for study of the microcirculation. *Nature Medicine*, 5(10):1209–1212, October 1999. ISSN 1546-170X. doi: 10.1038/13529.

[144] H. A. van Elteren, C. Ince, D. Tibboel, I. K. M. Reiss, and R. C. J. de Jonge. Cutaneous microcirculation in preterm neonates: Comparison between sidestream dark field (SDF) and incident dark field (IDF) imaging. *Journal of Clinical Monitoring and Computing*, 29(5):543–548, October 2015. ISSN 1573-2614. doi: 10.1007/s10877-015-9708-5.

[145] V. Cerný, Z. Turek, and R. Pařízková. Orthogonal polarization spectral imaging. *Physiological Research*, 56(2):141–147, 2007. ISSN 0862-8408. doi: 10.33549/physiolres.930922.

[146] Orsolya Genzel-Boroviczény, Julia Strötgen, Anthony G. Harris, Konrad Messmer, and Frank Christ. Orthogonal Polarization Spectral Imaging (OPS): A Novel Method to Measure the Microcirculation in Term and Preterm Infants Transcutaneously. *Pediatric Research*, 51(3):386–391, March 2002. ISSN 1530-0447. doi: 10.1203/00006450-200203000-00019.

[147] Daniel Alexandre Bottino and Eliete Bouskela. Non-invasive techniques to access in vivo the skin microcirculation in patients. *Frontiers in Medicine*, 9, 2023. ISSN 2296-858X.

[148] Guclu Aykut, Gerke Veenstra, Claudia Scorcella, Can Ince, and Christiaan Boerma. Cytocam-IDF (incident dark field illumination) imaging for bedside monitoring of the microcirculation.

Intensive Care Medicine Experimental, 3(1):4, January 2015. ISSN 2197-425X. doi: 10.1186/s40635-015-0040-7.

[149] P. T. Goedhart, M. Khalilzada, R. Bezemer, J. Merza, and C. Ince. Sidestream Dark Field (SDF) imaging: A novel stroboscopic LED ring-based imaging modality for clinical assessment of the microcirculation. *Optics Express*, 15(23):15101–15114, November 2007. ISSN 1094-4087. doi: 10.1364/OE.15.015101.

[150] Howard Sherman, Stanley Klausner, and William A. Cook. Incident Dark-Field Illumination: A New Method for Microcirculatory Study. *Angiology*, 22(5):295–303, May 1971. ISSN 0003-3197. doi: 10.1177/000331977102200507.

[151] Jonathan A. Fan, Kui Bao, J. Britt Lassiter, Jiming Bao, Naomi J. Halas, Peter Nordlander, and Federico Capasso. Near-Normal Incidence Dark-Field Microscopy: Applications to Nanoplasmonic Spectroscopy. *Nano Letters*, 12(6):2817–2821, June 2012. ISSN 1530-6984. doi: 10.1021/nl300160y.

[152] G. Saiko and A. Douplik. Contrast Ratio Quantification During Visualization of Microvasculature. In Oliver Thews, Joseph C. LaManna, and David K. Harrison, editors, *Oxygen Transport to Tissue XL*, pages 369–373. Springer International Publishing, Cham, 2018. ISBN 978-3-319-91287-5. doi: 10.1007/978-3-319-91287-5_59.

[153] Malak Abdullah Almarshad, Md Saiful Islam, Saad Al-Ahmadi, and Ahmed S. BaHammam. Diagnostic Features and Potential Applications of PPG Signal in Healthcare: A Systematic Review. *Healthcare*, 10(3):547, March 2022. ISSN 2227-9032. doi: 10.3390/healthcare10030547.

[154] Matti Kaisti, Tuukka Panula, Jukka-Pekka Sirkiä, Mikko Pänkäälä, Tero Koivisto, Teemu Niiranen, and Ilkka Kantola. Hemodynamic Bedside Monitoring Instrument with Pressure and Optical Sensors: Validation and Modality Comparison. *Advanced Science*, 11(24):2307718, 2024. ISSN 2198-3844. doi: 10.1002/advs.202307718.

[155] Daniel Ray, Tim Collins, Sandra I. Woolley, and Prasad V. S. Ponnapalli. A Review of Wearable Multi-Wavelength Photoplethysmography. *IEEE Reviews in Biomedical Engineering*, 16:136–151, 2023. ISSN 1941-1189. doi: 10.1109/RBME.2021.3121476.

[156] Stefan A. Carp, Mitchell B. Robinson, and Maria A. Franceschini. Diffuse correlation spectroscopy: Current status and future outlook. *Neurophotonics*, 10(1):013509, January 2023. ISSN 2329-423X, 2329-4248. doi: 10.1117/1.NPh.10.1.013509.

[157] Nahar Ghouth, Monty S. Duggal, Alaa BaniHani, and Hani Nazzal. The diagnostic accuracy of laser Doppler flowmetry in assessing pulp blood flow in permanent teeth: A systematic review. *Dental Traumatology*, 34(5):311–319, 2018. ISSN 1600-9657. doi: 10.1111/edt.12424.

[158] Jean-Luc Cracowski and Matthieu Roustit. Current Methods to Assess Human Cutaneous Blood Flow: An Updated Focus on Laser-Based-Techniques. *Microcirculation*, 23(5):337–344, 2016. ISSN 1549-8719. doi: 10.1111/micc.12257.

[159] J. Aguirre, B. Hindelang, Andrei Berezhnoi, U. Darsow, F. Lauffer, K. Eyerich, T. Biedermann, and V. Ntziachristos. Assessing nailfold microvascular structure with ultra-wideband raster-scan optoacoustic mesoscopy. *Photoacoustics*, 10:31–37, June 2018. ISSN 2213-5979. doi: 10.1016/j.pacs.2018.02.002.

[160] Vanessa Smith, Claudia Ickinger, Elvis Hysa, Marcus Snow, Tracy Frech, Alberto Sulli, and Maurizio Cutolo. Nailfold capillaroscopy. *Best Practice & Research Clinical Rheumatology*, 37 (1):101849, March 2023. ISSN 1521-6942. doi: 10.1016/j.berh.2023.101849.

[161] Curt M. Treu, Omar Lupi, Daniel A. Bottino, and Eliete Bouskela. Sidestream dark field imaging: The evolution of real-time visualization of cutaneous microcirculation and its potential application in dermatology. *Archives of Dermatological Research*, 303(2):69–78, March 2011. ISSN 1432-069X. doi: 10.1007/s00403-010-1087-7.

[162] Edward Gilbert-Kawai, Jonny Coppel, Vassiliki Bountziouka, Can Ince, Daniel Martin, and for the Caudwell Xtreme Everest and Xtreme Everest 2 Research Groups. A comparison of the quality of image acquisition between the incident dark field and sidestream dark field video-microscopes. *BMC Medical Imaging*, 16(1):10, January 2016. ISSN 1471-2342. doi: 10.1186/s12880-015-0078-8.

[163] Inga Kiudulaite, Egle Belousoviene, Astra Vitkauskiene, and Andrius Pranskunas. Effects of remote ischemic conditioning on microcirculatory alterations in patients with sepsis: A single-arm clinical trial. *Annals of Intensive Care*, 11(1):55, April 2021. ISSN 2110-5820. doi: 10.1186/s13613-021-00848-y.

[164] Christopher T. Minson. Thermal provocation to evaluate microvascular reactivity in human skin. *Journal of Applied Physiology*, 109(4):1239–1246, October 2010. ISSN 8750-7587. doi: 10.1152/japplphysiol.00414.2010.

[165] M. Roustit, F. Maggi, S. Isnard, M. Hellmann, B. Bakken, and J. L. Cracowski. Reproducibility of a local cooling test to assess microvascular function in human skin. *Microvascular Research*, 79(1):34–39, January 2010. ISSN 0026-2862. doi: 10.1016/j.mvr.2009.11.004.

[166] S. Durand, B. Fromy, Ph. Bouyé, J. L. Saumet, and P. Abraham. Vasodilatation in response to repeated anodal current application in the human skin relies on aspirin-sensitive mechanisms. *The Journal of Physiology*, 540(1):261–269, 2002. ISSN 1469-7793. doi: 10.1113/jphysiol.2001.013364.

[167] S Durand, B Fromy, A Koïtka, M Tartas, J L Saumet, and P Abraham. Oral single high-dose aspirin results in a long-lived inhibition of anodal current-induced vasodilatation. *British Journal of Pharmacology*, 137(3):384–390, 2002. ISSN 1476-5381. doi: 10.1038/sj.bjp.0704868.

[168] Vincent Fleischhauer, Jan Bruhn, Stefan Rasche, and Sebastian Zaunseder. Photoplethysmography upon cold stress—impact of measurement site and acquisition mode. *Frontiers in Physiology*, 14, June 2023. ISSN 1664-042X. doi: 10.3389/fphys.2023.1127624.

[169] K. Yamakoshi, H. Shimazu, M. Shibata, and A. Kamiya. New oscillometric method for indirect measurement of systolic and mean arterial pressure in the human finger. Part 2: Correlation study. *Medical and Biological Engineering and Computing*, 20(3):314–318, May 1982. ISSN 1741-0444. doi: 10.1007/BF02442798.

[170] Ryan Rosenberry and Michael D. Nelson. Reactive hyperemia: A review of methods, mechanisms, and considerations. *American Journal of Physiology-Regulatory, Integrative and Comparative Physiology*, 318(3):R605–R618, March 2020. ISSN 0363-6119. doi: 10.1152/ajpregu.00339.2019.

[171] Maxime Fouchard, Laurent Misery, Raphaële Le Garrec, Dominique Sigaudo-Roussel, and Bérengère Fromy. Alteration of Pressure-Induced Vasodilation in Aging and Diabetes, a Neuro-Vascular Damage. *Frontiers in Physiology*, 10, July 2019. ISSN 1664-042X. doi: 10.3389/fphys.2019.00862.

[172] Gbenga Ogedegbe and Thomas Pickering. Principles and Techniques of Blood Pressure Measurement. *Cardiology Clinics*, 28(4):571–586, November 2010. ISSN 0733-8651. doi: 10.1016/j.ccl.2010.07.006.

[173] Mohamad Forouzanfar, Hilmi R. Dajani, Voicu Z. Groza, Miodrag Bolic, Sreeraman Rajan, and Izmail Batkin. Oscillometric Blood Pressure Estimation: Past, Present, and Future. *IEEE Reviews in Biomedical Engineering*, 8:44–63, 2015. ISSN 1941-1189. doi: 10.1109/RBME.2015.2434215.

[174] Jing Liu, Charles G. Sodini, Yanghui Ou, Bryan Yan, Yuan-Ting Zhang, and Ni Zhao. Feasibility of Fingertip Oscillometric Blood Pressure Measurement: Model-Based Analysis and Experimental Validation. *IEEE Journal of Biomedical and Health Informatics*, 24(2):533–542, February 2020. ISSN 2168-2208. doi: 10.1109/JBHI.2019.2919896.

[175] Tuukka Panula, Jukka-Pekka Sirkiä, David Wong, and Matti Kaisti. Advances in Non-Invasive Blood Pressure Measurement Techniques. *IEEE Reviews in Biomedical Engineering*, 16:424–438, 2023. ISSN 1941-1189. doi: 10.1109/RBME.2022.3141877.

[176] Larisa G. Tereshchenko and Mark E. Josephson. Frequency content and characteristics of ventricular conduction. *Journal of Electrocardiology*, 48(6):933–937, November 2015. ISSN 0022-0736. doi: 10.1016/j.jelectrocard.2015.08.034.

[177] Felix Scholkmann, Jens Boss, and Martin Wolf. An Efficient Algorithm for Automatic Peak Detection in Noisy Periodic and Quasi-Periodic Signals. *Algorithms*, 5(4):588–603, December 2012. ISSN 1999-4893. doi: 10.3390/a5040588.

[178] Jiapu Pan and Willis J. Tompkins. A Real-Time QRS Detection Algorithm. *IEEE Transactions on Biomedical Engineering*, BME-32(3):230–236, March 1985. ISSN 1558-2531. doi: 10.1109/TBME.1985.325532.

[179] Willem JW Bos, Elisabeth Verrij, Hieronymus H. Vincent, Berend E. Westerhof, Gianfranco Parati, and Gert A. van Montfrans. How to assess mean blood pressure properly at the brachial artery level. *Journal of Hypertension*, 25(4):751, April 2007. ISSN 0263-6352. doi: 10.1097/HJH.0b013e32803fb621.

[180] Tuukka Panula, Tero Koivisto, Mikko Pänkäälä, Teemu Niiranen, Ilkka Kantola, and Matti Kaisti. An instrument for measuring blood pressure and assessing cardiovascular health from the fingertip. *Biosensors and Bioelectronics*, 167:112483, November 2020. ISSN 0956-5663. doi: 10.1016/j.bios.2020.112483.

[181] Jukka-Pekka Sirkiä, Tuukka Panula, and Matti Kaisti. Wearable edge machine learning with synthetic photoplethysmograms. *Expert Systems with Applications*, 238:121523, March 2024. ISSN 0957-4174. doi: 10.1016/j.eswa.2023.121523.

[182] Jihyoung Lee, Kenta Matsumura, Ken-ichi Yamakoshi, Peter Rolfe, Shinobu Tanaka, and Takehiro Yamakoshi. Comparison between red, green and blue light reflection photoplethysmography for heart rate monitoring during motion. In *2013 35th Annual International Conference of the IEEE Engineering in Medicine and Biology Society (EMBC)*, pages 1724–1727, July 2013. doi: 10.1109/EMBC.2013.6609852.

[183] Jukka-Pekka Sirkiä, Tuukka Panula, and Matti Kaisti. Investigating the impact of contact pressure on photoplethysmograms. *Biomedical Engineering Advances*, 7:100123, June 2024. ISSN 2667-0992. doi: 10.1016/j.bea.2024.100123.

[184] M. Hickey and P. A. Kyriacou. Optimal spacing between transmitting and receiving optical fibres in reflectance pulse oximetry. *Journal of Physics: Conference Series*, 85(1):012030, October 2007. ISSN 1742-6596. doi: 10.1088/1742-6596/85/1/012030.

[185] Charles F. Babbs. Oscillometric measurement of systolic and diastolic blood pressures validated in a physiologic mathematical model. *BioMedical Engineering OnLine*, 11(1):56, August 2012. ISSN 1475-925X. doi: 10.1186/1475-925X-11-56.

[186] George S. Stergiou, Bruce Alpert, Stephan Mieke, Roland Asmar, Neil Atkins, Siegfried Eckert, Gerhard Frick, Bruce Friedman, Thomas Graßl, Tsutomu Ichikawa, John P. Ioannidis, Peter Lacy, Richard McManus, Alan Murray, Martin Myers, Paolo Palatini, Gianfranco Parati, David Quinn, Josh Sarkis, Andrew Shennan, Takashi Usuda, Jiguang Wang, Colin O. Wu, and Eoin O'Brien. A universal standard for the validation of blood pressure measuring devices: Association for the Advancement of Medical Instrumentation/European Society of Hypertension/International Organization for Standardization (AAMI/ESH/ISO) Collaboration Statement. *Journal of Hypertension*, 36(3):472, March 2018. ISSN 0263-6352. doi: 10.1097/HJH.0000000000001634.

[187] Nienke Bosschaart, Gerda J. Edelman, Maurice C. G. Aalders, Ton G. van Leeuwen, and Dirk J. Faber. A literature review and novel theoretical approach on the optical properties of whole blood. *Lasers in Medical Science*, 29(2):453–479, March 2014. ISSN 1435-604X. doi: 10.1007/s10103-013-1446-7.

[188] Andreia V. Moço, Sander Stuijk, and Gerard de Haan. New insights into the origin of remote PPG signals in visible light and infrared. *Scientific Reports*, 8(1):8501, May 2018. ISSN 2045-2322. doi: 10.1038/s41598-018-26068-2.

[189] Marianne Agerskov, Anna N. W. Thusholdt, Henrik Holm-Sørensen, Sebastian Wiberg, Christian S. Meyhoff, Jakob Højlund, Niels H. Secher, and Nicolai B. Foss. Association of the intraoperative peripheral perfusion index with postoperative morbidity and mortality in acute surgical patients: A retrospective observational multicentre cohort study. *British Journal of Anaesthesia*, 127(3):396–404, September 2021. ISSN 0007-0912. doi: 10.1016/j.bja.2021.06.004.

[190] A. C. M. Dassel, R. Graaff, M. Sikkema, A. Meijer, W. G. Zijlstra, and J. G. Aarnoudse. Reflectance pulse oximetry at the forehead improves by pressure on the probe. *Journal of Clinical Monitoring*, 11(4):237–244, July 1995. ISSN 1573-2614. doi: 10.1007/BF01617518.

[191] Chong Liu, Ricardo Correia, Hattan Khaled Ballaji, Serhiy Korposh, Barrie R. Hayes-Gill, and Stephen P. Morgan. Optical Fibre-Based Pulse Oximetry Sensor with Contact Force Detection. *Sensors*, 18(11):3632, November 2018. ISSN 1424-8220. doi: 10.3390/s18113632.

[192] Anand Chandrasekhar, Mohammad Yavarimanesh, Keerthana Natarajan, Jin-Oh Hahn, and Ramakrishna Mukkamala. PPG Sensor Contact Pressure Should Be Taken Into Account for Cuff-Less Blood Pressure Measurement. *Ieee Transactions on Biomedical Engineering*, 67(11):3134–3140, November 2020. ISSN 0018-9294. doi: 10.1109/TBME.2020.2976989.

[193] Zeng-Ding Liu, Ye Li, Yuan-Ting Zhang, Jia Zeng, Zu-Xian Chen, Zhi-Wei Cui, Ji-Kui Liu, and Fen Miao. Cuffless Blood Pressure Measurement Using Smartwatches: A Large-Scale Validation Study. *IEEE Journal of Biomedical and Health Informatics*, 27(9):4216–4227, September 2023. ISSN 2168-2208. doi: 10.1109/JBHI.2023.3278168.

[194] Eric Chern-Pin Chua, Stephen J. Redmond, Gary McDarby, and Conor Heneghan. Towards Using Photo-Plethysmogram Amplitude to Measure Blood Pressure During Sleep. *Annals of Biomedical Engineering*, 38(3):945–954, March 2010. ISSN 1573-9686. doi: 10.1007/s10439-009-9882-z.

[195] Shaoxiong Sun, Erik Bresch, Jens Muehlsteff, Lars Schmitt, Xi Long, Rick Bezemer, Igor Paulussen, Gerrit J. Noordergraaf, and Ronald M. Aarts. Systolic blood pressure estimation using ECG and PPG in patients undergoing surgery. *Biomedical Signal Processing and Control*, 79:104040, January 2023. ISSN 1746-8094. doi: 10.1016/j.bspc.2022.104040.

[196] Stephen R. Alty, Natalia Angarita-Jaimes, Sandrine C. Millasseau, and Philip J. Chowienczyk. Predicting Arterial Stiffness From the Digital Volume Pulse Waveform. *IEEE Transactions on Biomedical Engineering*, 54(12):2268–2275, December 2007. ISSN 1558-2531. doi: 10.1109/TBME.2007.897805.

[197] Paul S. Addison. Slope Transit Time (STT): A Pulse Transit Time Proxy requiring Only a Single Signal Fiducial Point. *IEEE Transactions on Biomedical Engineering*, 63(11):2441–2444, November 2016. ISSN 1558-2531. doi: 10.1109/TBME.2016.2528507.

[198] Ramakrishna Mukkamala, Jin-Oh Hahn, Omer T. Inan, Lalit K. Mestha, Chang-Sei Kim, Hakan Töreyin, and Survi Kyal. Toward Ubiquitous Blood Pressure Monitoring via Pulse Transit Time: Theory and Practice. *IEEE Transactions on Biomedical Engineering*, 62(8):1879–1901, August 2015. ISSN 1558-2531. doi: 10.1109/TBME.2015.2441951.

[199] Younhee Choi, Qiao Zhang, and Seokbum Ko. Noninvasive cuffless blood pressure estimation using pulse transit time and Hilbert–Huang transform. *Computers & Electrical Engineering*, 39 (1):103–111, January 2013. ISSN 0045-7906. doi: 10.1016/j.compeleceng.2012.09.005.

[200] K. Pilt, K. Meigas, R. Ferenets, K. Temitski, and M. Viigimaa. Photoplethysmographic signal waveform index for detection of increased arterial stiffness. *Physiological Measurement*, 35(10): 2027, September 2014. ISSN 0967-3334. doi: 10.1088/0967-3334/35/10/2027.

[201] L. Wang, Emma Pickwell-MacPherson, Y. P. Liang, and Y. T. Zhang. Noninvasive cardiac output estimation using a novel photoplethysmogram index. In *2009 Annual International Conference of the IEEE Engineering in Medicine and Biology Society*, pages 1746–1749, September 2009. doi: 10.1109/IEMBS.2009.5333091.

[202] Kenji Takazawa, Nobuhiro Tanaka, Masami Fujita, Osamu Matsuoka, Tokuyu Saiki, Masaru Aikawa, Sinobu Tamura, and Chiharu Ibukiyama. Assessment of Vasoactive Agents and Vascular Aging by the Second Derivative of Photoplethysmogram Waveform. *Hypertension*, 32(2):365–370, August 1998. doi: 10.1161/01.HYP.32.2.365.

[203] Issei Imanaga, Hiroshi Hara, Samonn Koyanagi, and Kohtaro Tanaka. Correlation between Wave Components of the Second Derivative of Plethysmogram and Arterial Distensibility. *Japanese Heart Journal*, 39(6):775–784, 1998. doi: 10.1536/ihj.39.775.

[204] Hyun Jae Baek, Jung Soo Kim, Yun Sung Kim, Haet Bit Lee, and Kwang Suk Park. Second Derivative of Photoplethysmography for Estimating Vascular Aging. In *2007 6th International Special Topic Conference on Information Technology Applications in Biomedicine*, pages 70–72, November 2007. doi: 10.1109/ITAB.2007.4407346.

[205] Andris Grabovskis, Zbignevs Marcinkevics, Uldis Rubins, and Edgars Kviesis-Kipge. Effect of probe contact pressure on the photoplethysmographic assessment of conduit artery stiffness. *Journal of Biomedical Optics*, 18(2):027004, February 2013. ISSN 1083-3668, 1560-2281. doi: 10.1117/1.JBO.18.2.027004.

[206] Gerardo Tusman, Cecilia M. Acosta, Sven Pulletz, Stephan H. Böhm, Adriana Scandurra, Jorge Martinez Arca, Matías Madorno, and Fernando Suarez Sipmann. Photoplethysmographic characterization of vascular tone mediated changes in arterial pressure: An observational study. *Journal of Clinical Monitoring and Computing*, 33(5):815–824, October 2019. ISSN 1573-2614. doi: 10.1007/s10877-018-0235-z.

[207] H. Njoum and P. A. Kyriacou. Investigation of finger reflectance photoplethysmography in volunteers undergoing a local sympathetic stimulation. *Journal of Physics: Conference Series*, 450 (1):012012, June 2013. ISSN 1742-6596. doi: 10.1088/1742-6596/450/1/012012.

[208] P.E. McSharry, G.D. Clifford, L. Tarassenko, and L.A. Smith. A dynamical model for generating synthetic electrocardiogram signals. *IEEE Transactions on Biomedical Engineering*, 50(3):289–294, March 2003. ISSN 1558-2531. doi: 10.1109/TBME.2003.808805.

[209] Matti Kaisti, Juho Laitala, and Antti Airola. Training neural networks with synthetic electrocardiograms, November 2021.

[210] J. Timmer and M. König. On generating power law noise. *Astronomy and Astrophysics*, 300: 707, August 1995. ISSN 0004-6361.

[211] P. Welch. The use of fast Fourier transform for the estimation of power spectra: A method based on time averaging over short, modified periodograms. *IEEE Transactions on Audio and Electroacoustics*, 15(2):70–73, June 1967. ISSN 1558-2582. doi: 10.1109/TAU.1967.1161901.

[212] Steven M. Bishop and Ari Ercole. Multi-scale peak and trough detection optimised for periodic and quasi-periodic neuroscience data. In Thomas Heldt, editor, *Intracranial Pressure & Neuromonitoring XVI*, pages 189–195, Cham, 2018. Springer International Publishing. ISBN 978-3-319-65798-1.

[213] Paul van Gent, Haneen Farah, Nicole van Nes, and Bart van Arem. HeartPy: A novel heart rate algorithm for the analysis of noisy signals. *Transportation Research Part F: Traffic Psychology and Behaviour*, 66:368–378, October 2019. ISSN 1369-8478. doi: 10.1016/j.trf.2019.09.015.

[214] Hang Sik Shin, Chungkeun Lee, and Myoungho Lee. Adaptive threshold method for the peak detection of photoplethysmographic waveform. *Computers in Biology and Medicine*, 39(12): 1145–1152, December 2009. ISSN 0010-4825. doi: 10.1016/j.compbiomed.2009.10.006.

[215] Sangita Das, Saurabh Pal, and Madhuchhanda Mitra. Real time heart rate detection from PPG signal in noisy environment. In *2016 International Conference on Intelligent Control Power and Instrumentation (ICICPI)*, pages 70–73, October 2016. doi: 10.1109/ICICPI.2016.7859676.

TURUN
YLIOPISTO
UNIVERSITY
OF TURKU

ISBN 978-952-02-0236-1 (PRINT)
ISBN 978-952-02-0237-8 (PDF)
ISSN 2736-9390 (Painettu/Print)
ISSN 2736 9684 (Sähköinen/Online)

Painosalama, Turku, Finland 2025